MODELING AND CONTROL OF ANGIOPLASTY BALLOON DEPLOYMENT BASED ON INTRAVASCULAR OPTICAL COHERENCE TOMOGRAPHY

HAMED AZARNOUSH

DEPARTMENT OF ELECTRICAL AND COMPUTER ENGINEERING

McGILL UNIVERSITY, MONTREAL

OCTOBER 2011

A THESIS SUBMITTED TO McGILL UNIVERSITY IN PARTIAL FULFILLMENT OF THE REQUIREMENTS OF THE DEGREE OF PHILOSOPHIAE DOCTOR

Dedication

This thesis is dedicated to my wife, Sara.

Acknowledgment

I am grateful to my academic advisor Prof. Benoit Boulet from the Centre for Intelligent Machines (CIM) for his wonderful support, advice, and encouragement throughout my studies. I acknowledge the financial support of the Natural Sciences and Engineering Research Council (NSERC) of Canada.

The majority of experiments in this thesis were performed at the Industrial Materials Institute (IMI) of the National Research Council (NRC) of Canada. I am grateful to my advisor at IMI, Dr. Guy Lamouche, for providing me with various resources, e.g., the optical coherence tomography (OCT) system. Dr. Lamouche also provided valuable guidance and support in my research activities. I would especially like to thank Dr. Sébastien Vergnole for providing me with training to use the OCT system and for offering me valuable support in the development of the experimental setup. For the inflation control experiments, he also integrated my image analysis and control algorithms in the previously developed image acquisition software. I am thankful to Dr. Robert DiRaddo for providing me with valuable resources, such as the finite-element software, developed at IMI. Dr. Valérie Pazos and Patricia Debergue provided me with training and support to use the software. Dr. Pazos also performed the uniaxial tensile tests. Christian de Grandpré produced the catheters used in my experiments. He also trained me to use the hydraulic pressure tester. Charles-Étienne Bisaillon produced the artery phantoms. Jacques Dufour kindly lent me the computerized syringe pump for my experiments. Bruno Gauthier, Rafik Bourezak, Marc Dufour, Anna Bardetti, and Frédéric D'Amours have also been supportive in my research. I would like to thank them all.

The beating heart experiments were performed at the Institute for Biodiagnostics (IBD) of the NRC. I am thankful to Dr. Mike Sowa for providing me with the opportunity. I also thank Lori Gregorash, Bo Xiang, and Michael Smith, for preparing the setup and Dr. Mark Hewko for his support in experiments.

I would also like to thank all my friends and the professors at CIM who made my studies at McGill a wonderful and rewarding experience.

Last but not least, I am grateful to my family and Sara's family for their patience and encouragement which helped me focus on my studies despite the long distance from home.

Claim of Originality

To our knowledge no result has been published prior to this research on monitoring, characterization, simulation, or control of angioplasty balloon deployment based on intravascular optical coherence tomography (IVOCT). The original results appear in Chapters 6 through 11. Chapter 6 includes theoretical treatment and simulation of balloon deployment control. Chapter 7 [1, 2] presents monitoring and characterization of balloon deformation. Chapter 8 [3] presents monitoring and characterization of deformation of various artery phantoms. In Chapter 9 [4], IVOCT monitoring and characterization is proposed as a method to validate angioplasty simulation results. This chapter presents a comparison of finite-element simulation and experimental results. Chapter 10 [5] presents experimental validation of a method to control the luminal diameter of an artery phantom during balloon inflation. Chapter 11 [6] presents validation of the same method to control the luminal diameter of porcine arteries in an excised heart and in an *ex vivo* beating heart. The results of this research have been presented at various conferences [7-12].

The ideas proposed in this thesis are mainly developed by me as a result of a review of the literature and consultation with advisors. Based on these ideas, I planned for various experiment scenarios and developed a theoretical and an experimental framework. To achieve the goals of the theoretical framework, I developed image analysis algorithms, finite-element models and control concepts. I performed all finite-element simulations and post-simulation analyses. For the experimental framework, I integrated different elements, e.g., the imaging system, pumps, and catheters, from different labs at IMI to generate a setup, customized to my experiments. The experiments were designed and performed by me. I also performed post-processing and analysis of the acquired data.

Abstract

Cardiovascular disease is the leading cause of death in industrialized nations. Angioplasty is performed on millions of patients every year. It is, therefore, essential to constantly explore and investigate new approaches to study and improve the outcomes of this minimally-invasive procedure. In this thesis, novel applications of intravascular optical coherence tomography (IVOCT) are proposed, namely, monitoring, characterization, simulation, and control of balloon inflation.

High-resolution IVOCT images lead to a detailed assessment of microstructures. Using image analysis techniques, IVOCT characterization of balloon deformation is presented as a method to validate the performance of balloons. IVOCT characterization of the deformation of artery phantoms is proposed as a method to study the tissue's response to various balloon sizes, various balloon folding strategies and various inflation strategies.

In addition, IVOCT characterization of deformation is proposed as a method to validate simulation results. This thesis provides a comparison between finite-element simulation results and experimental results for two case studies, which investigate the effects of variation of mechanical properties as well as balloon unfolding and inflation process.

Finally, in this thesis, methods are proposed to control the balloon inflation. During balloon inflation, the luminal diameter of an artery could be estimated in real-time and used in a feedback loop to control the inflation. The experimental relevance of this method is demonstrated when the balloon is inflated in an artery phantom, in an artery of an excised porcine heart and in an artery of a beating porcine heart.

The methods and the results, provided in this thesis, could benefit the developers of angioplasty devices, cardiovascular research, and clinical users.

Résumé

Les maladies cardiovasculaires sont la principale cause de décès dans les pays industrialisés. L'angioplastie est réalisée sur des millions de patients chaque année. Il est donc essentiel de constamment explorer et étudier de nouvelles approches pour étudier et améliorer les résultats de cette procédure peu invasive. Dans cette thèse, de nouvelles applications de la tomographie par cohérence optique intravasculaire (IVOCT) sont proposées, à savoir, la surveillance, la caractérisation, la simulation et le contrôle du gonflement du ballon.

Des images haute résolution IVOCT mènent à une évaluation détaillée des microstructures. En utilisant des techniques d'analyse d'image, la caractérisation de la déformation du ballon est présentée comme une méthode pour valider la performance de ballons. La caractérisation de la déformation des fantômes est proposée comme une méthode pour étudier la réponse des tissus à des tailles différentes de ballons, et diverses stratégies de pliage et de gonflement du ballon.

En outre, la caractérisation de la déformation est proposée pour valider les résultats de simulation. Une comparaison est fournie entre les résultats de la simulation par éléments finis et des résultats expérimentaux pour les deux études de cas, qui étudient les effets de la variation des propriétés mécaniques ainsi que le processus de déploiement et de gonflement du ballon.

Enfin, dans cette thèse, des méthodes sont proposées pour contrôler le gonflement du ballon. Pendant le gonflement du ballon, le diamètre luminal de l'artère peut être estimé en temps réel et utilisé dans une boucle de rétroaction pour contrôler le gonflement. La

pertinence expérimentale de cette méthode est démontrée lorsque le ballon est gonflé dans un fantôme, dans les artères porcines d'un cœur excisé et d'un cœur battant.

Les méthodes et les résultats fournis dans cette thèse pourraient bénéficier aux développeurs de dispositifs d'angioplastie, à la recherche cardiovasculaire et aux utilisateurs cliniques.

Table of contents

Chapter 1: Introduction 1

1.1 Statement of the problem and objectives 1
1.2 Methodology 2
1.3 Motivation 4
1.4 Contribution 6
1.5 Outline 8

Chapter 2: Angioplasty 9

2.1 Angioplasty procedures 9
2.2 Vascular imaging 12
2.2.1. Angiography 12
2.2.2. Intravascular ultrasound 13
2.3 Related research 13

Chapter 3: Optical coherence tomography 16

3.1 SS-OCT principles 16
3.2 Experimental imaging setup 18
3.2.1. SS-OCT system 18
3.2.2. IVOCT probe 19
3.2.3. Rotation-translation unit 20

Chapter 4: Gray-scale image analysis 21

4.1 Global operations 22
4.2 Local operations 24
4.2.1. Noise reduction 26
4.2.2. Ridge detection 28
4.2.3. Edge detection 29
4.3 Image registration and object characterization 32
4.3.1. Image registration 32
4.3.2. Object characterization 32

Chapter 5: Finite-element simulation 33

5.1 Constitutive modeling 33
5.2 In-house FEM software to simulate angioplasty 34

5.2.1. Inputs 35
5.2.2. Solving protocol 36
5.2.3. Outputs 37
5.3 Interface with intravascular imaging 37
5.4 Validation 38
Chapter 6: Balloon inflation control 39
6.1 Experimental angioplasty simulation setup 39
6.2 Pressure control 42
6.2.1. Proportional control 43
6.2.2. Control based on online estimation of the compliance curve 46
6.3 Diameter control 50
6.4 Pressure and diameter control 53
6.5 Concluding remarks 56
Chapter 7: IVOCT monitoring and characterization of balloon deformation in a deployment tester 58
7.1 Balloon production 59
7.2 Structure of the OCTIB catheter 61
7.3 Integration of the OCTIB catheter in a deployment tester 63
7.4 IVOCT monitoring of balloon deformation 64
7.5 Image analysis 68
7.5.1. Image registration 68
7.5.2. Ridge detection 69
7.5.3. Sequential algorithm for contour detection 70
7.5.4. Conversion from pixel values to values in geometrical distance 71
7.6 IVOCT characterization of the balloon deformation 72
7.7 Concluding remarks 76
Chapter 8: IVOCT monitoring and characterization of phantom deformation 77
8.1 Experimental setup 79
8.2 Scenario 1: IVOCT monitoring of the deformation of single-layer phantoms with different mechanical properties during balloon inflation 79
8.3 Scenario 2: IVOCT monitoring of the deformation of a three-layer phantom during balloon unfolding and balloon inflation 80
8.4 Image analysis 82

8.4.1. Ridge detection 84
8.4.2. Edge detection 84
8.4.3. Sequential algorithm for contour detection 85
8.4.4. Conversion from pixel values to values in geometrical distance 86
8.5 IVOCT characterization of phantom deformation 87
8.5.1. Scenario 1 87
8.5.2. Scenario 2 89
8.6 Concluding remarks 92

Chapter 9: Finite-element simulation of deformation based on IVOCT 93

9.1 Generation of a simulation model for the balloon 94
9.2 Simulation of Scenario 1 96
9.3 Simulation of Scenario 2 97
9.4 Simulation results 98
9.4.1. Generation of a simulation model for the balloon 98
9.4.2. Scenario 1 100
9.4.3. Scenario 2 102
9.5 Concluding remarks 104

Chapter 10: Real-time control of balloon inflation based on feedback from IVOCT: experimental validation in an artery phantom 105

10.1 Lumen detection in IVOCT images 106
10.2 Control system architecture 111
10.3 Hardware implementation of the control system 112
10.4 Results 113
10.4.1. Various target diameter values 114
10.4.2. Various flow rate gain values 116
10.4.3. Sequential target diameter values 118
10.5 Concluding remarks 120

Chapter 11: Real-time control of balloon inflation based on feedback from IVOCT: experimental validation in an excised heart and a beating heart model 121

11.1 IVOCT-imaging through a compliant balloon 122

11.2 Porcine heart experiments 122
11.2.1. Excised heart model 122
11.2.2. Beating heart model 123
11.3 Monitoring balloon inflation in a porcine artery 124
11.4 Balloon detection in IVOCT images 126
11.5 Control system 129
11.6 Results 129
11.6.1. Inflation control in an excised heart 130
11.6.2. Inflation control in an artery of a beating heart 131
11.7 Concluding remarks 136
Chapter 12: Conclusion and Future Work 138

List of figures

Figure 2.1. Balloon angioplasty (image provided courtesy of Boston Scientific. © 2011 Boston Scientific Corporation or its affiliates. All rights reserved.) 10
Figure 2.2. Stent implantation (image provided courtesy of Boston Scientific. © 2011 Boston Scientific Corporation or its affiliates, All rights reserved.) 11
Figure 2.3. Stenosis identified on an angiogram (image provided courtesy of the Radiological Society of North America [39]) 12
Figure 2.4. An IVUS image of an artery (image source: National Research Council Canada) 13
Figure 3.1. Basic configuration of a fibered SS-OCT setup (Cp: coupler, D: detector). 17
Figure 3.2. Experimental imaging setup 18
Figure 3.3. Schematic of the SS-OCT setup (Cp1 and Cp2: couplers, PC: polarization controller, Cir1 and Cir2: circulators, D: balanced detection, NC: not connected, ATU: artery testing unit). 19
Figure 3.4. Schematic of the IVOCT probe 19
Figure 4.1. A grayscale image (a) and the column j_0 of the corresponding image matrix (b) 21
Figure 4.2. Image histogram 22
Figure 4.3. The grayscale image obtained from FSHS (a) and the column j_0 of the corresponding image matrix (b) 23
Figure 4.4. Image histogram after application of FSHS 23
Figure 4.5. The grayscale image after reversing bright and dark regions (a) and the column j_0 of the corresponding image matrix (b) 24
Figure 4.6. The grayscale image after adding salt and pepper noise (a) and the column j_0 of the corresponding image matrix (b) 26
Figure 4.7. The grayscale image after application of a uniform filter (a) and the column j_0 of the corresponding image matrix (b) 27
Figure 4.8. The grayscale image after application of a median filter (a) and the column j_0 of the corresponding image matrix (b) 28
Figure 4.9. A rotating kernel and the set of corresponding masks 29
Figure 5.1. Side view of artery (a), cross-sectional images (b), meshing (c), and simulation results (d) 37
Figure 6.1. Interconnection between components in a balloon inflation setup 40
Figure 6.2. Diameter-pressure curves for a non-compliant (a), a semi-compliant (b), and a compliant (c) balloon 41
Figure 6.3. A typical pressure-volume curve 42
Figure 6.4. Inflation control based on pressure feedback 43

Figure 6.5. Proportional control for two different gains 46
Figure 6.6. Proportional control for $\alpha = 2$ and $\alpha = 4$ 46
Figure 6.7. Pressure control based on online estimation of the compliance curve 49
Figure 6.8. Inflation control based on diameter feedback 51
Figure 6.9. Diameter control with and without a time delay 52
Figure 6.10. Inflation control based on pressure and diameter feedback 53
Figure 6.11. Diameter control with different pressurization rates 55
Figure 6.12. Diameter control with a desired pressurization rate with and without a time delay 56
Figure 7.1. Balloon inflation monitoring using a laser scanner 58
Figure 7.2. The balloon forming machine (9810-H, Interface Catheter Solutions) 60
Figure 7.3. Balloon forming stages 61
Figure 7.4. Schematic (a) (B: Balloon, F: ferrule, PS: polymer sheath, GRIN: gradient-index lens, LB: light beam, OF: optical fiber, PT: polymer tube, RAP: right-angle prism) and illustration of the OCTIB catheter (b) 63
Figure 7.5. Cross-section of the OCTIB catheter (proximal side) 63
Figure 7.6. Schematic (a) and illustration of OCTIB catheter in the deployment tester 64
Figure 7.7. IVOCT image of the balloon in polar (a) and Cartesian (b) coordinates and an A-scan profile (c) 66
Figure 7.8. 3D rendering of the balloon, obtained from a pullback at a pressure of 4 atm 67
Figure 7.9. IVOCT images of the balloon at pressures of 2 atm (a), 3 atm (b) and 4 atm (c) and the corresponding balloon deformation profiles (d-f) with color maps in μm 73
Figure 7.10. IVOCT characterization of balloon diameter (a), and wall thickness (b) 75
Figure 7.11. IVOCT characterization of balloon compliance 75
Figure 8.1. Sample IVOCT image in polar (a) and Cartesian (b) coordinates, and a sample A-scan (c) from Scenario 1 81
Figure 8.2. Sample IVOCT image in polar (a) and Cartesian (b) coordinates, and a sample A-scan (c) from Scenario 2 83
Figure 8.3. Stress-strain data from uniaxial tensile tests with linear fits for Phantom 1, Phantom 2, and Phantom 3, fabricated with different silicone formulation providing different mechanical properties 87
Figure 8.4. Contour detection in IVOCT images of Phantom 2 at pressures of 0 atm (a), and 4 atm (b) 88
Figure 8.5. Comparison of inner and outer diameters obtained for the three phantoms from image analysis 88

Figure 8.6. Contour detection in IVOCT images of the phantom during the balloon unfolding (a,b) and during the balloon inflation (c,d) process.....90
Figure 8.7. Inner and outer diameters of the phantom during the balloon unfolding and the balloon inflation process.....91
Figure 8.8. Layer thickness characterization of the phantom during the balloon unfolding and the balloon inflation process.....91
Figure 9.1. Optimization of material model parameters for the balloon.....96
Figure 9.2. Balloon image at pressure of 0 atm (a), and balloon mesh (b).....98
Figure 9.3. Ogden parameters (a) and the residual error (b) during optimization.....99
Figure 9.4. Comparison of diameter values obtained from experiment and from simulation with the optimized material parameters.....100
Figure 9.5. IVOCT images of Phantoms 2 at pressure of 0 atm (a), and 4 atm (b), the generated meshes (c), and the simulation result for the pressure of 4 atm (d).....101
Figure 9.6 Comparison of inner and outer diameters obtained for the three phantoms from experiments and simulations.....101
Figure 9.7. IVOCT image at 0 atm (a) at 1 atm (b), and at 2 atm(c), the corresponding mesh (d), and simulation results at 1 atm (e) and at 2 atm (f).....103
Figure 9.8. Inner and outer diameters obtained from experiments and simulations.....104
Figure 10.1. Sample image in polar (a) and Cartesian (b) coordinates.....107
Figure 10.2. Description of different steps to extract one luminal contour node.....108
Figure 10.3. Detection of the luminal contour nodes represented as red dots.....110
Figure 10.4. Balloon inflation control system.....112
Figure 10.5. Hardware implementation of the balloon inflation control system.....113
Figure 10.6. The diameter (a), the volume (b), and the pressure (c), obtained from control experiments applying different target diameters (4.1, 4.3 mm).....116
Figure 10.7. The diameter (a), the volume (b), and the pressure (c), obtained from control experiments using different flow rate gains (500, 750 and 1000 mL/h).....117
Figure 10.8. Acquired images at milestone diameters (a-c), the diameter (d), the volume (e), and the pressure (f) during the control experiment using a sequence of target diameters.....119
Figure 11.1. Schematic of the IVOCT probe inside the balloon catheter.....122
Figure 11.2. The excised heart setup.....123
Figure 11.3. Main steps to prepare the beating heart setup.....124
Figure 11.4. The beating heart setup.....124
Figure 11.5. A sample IVOCT image in polar (a) and in Cartesian (b) coordinates.....125

Figure 11.6. Description of different steps to extract luminal contour nodes, sample A-scans (a,b), averaging results (c,d), median filtering results (e,f), and gradient operation results (g,h) 127
Figure 11.7. Detection of the balloon contour, provided by the detected red dots 128
Figure 11.8. Results of balloon inflation experiment in an excised heart: IVOCT images (a-c), balloon diameter (d), delivered volume (e) and inflation pressure (f) 130
Figure 11.9. The diameter (a), the volume (b), and the pressure (c), obtained from control experiments using various target diameters (2.1, 2.3 mm). 132
Figure 11.10. The diameter (a), the volume (b), and the pressure (c), obtained from control experiments using different flow rates (100, 250 and 400 mL/h)..... 134
Figure 11.11. Acquired images at various diameters (a-d), and the diameter (e), the volume (f), and the pressure (g) during the control experiment using a sequence of target diameters 135

List of tables

Table 7.1. Balloon forming parameters 61
Table 10.1. Performance characteristics of control experiments using different target diameters (4.1, 4.3 mm) 116
Table 10.2. Performance characteristics of control experiments using different flow rate gains (500, 750 and 1000 mL/h) 118
Table 11.1. Performance characteristics of control experiments using different target diameters (2.1, 2.3 mm) 133
Table 11.2. Performance characteristics of control experiments using different flow rate gains (100, 250 and 400 mL/h) 134

List of acronyms

A	Adventitia
B	Balloon
BMS	Bare metal stent
DES	Drug-eluting stent
FD-OCT	Fourier domain optical coherence tomography
F	Ferrule
FPS	Frames per second
FSHS	Full-scale histogram stretch
GRIN	Graded index
I	Intima
IBD	Institute for Biodiagnostics
IMI	Industrial Materials Institute
IVOCT	Intravascular optical coherence tomography
IVUS	Intravascular ultrasound
LAD	Left anterior descending
LB	Laser beam
M	Media
MRI	Magnetic resonance imaging
NRC	National Research Council
OCT	Optical coherence tomography
OCTIB	Optical coherence tomography imaging balloon
OF	Optical fiber
OFDI	Optical Fourier domain imaging
P	Phantom
PS	Polymer sheath
PT	Polymer tube
R	Reference
RAP	Right-angle prism
SS-OCT	Swept source optical coherence tomography
TD-OCT	Time domain optical coherence tomography

CHAPTER 1: INTRODUCTION

Atherosclerosis is a condition in which fatty materials, known as plaque, accumulate in the walls of arteries. This condition may lead to stenosis (narrowing) or blockage of arteries, preventing the blood from feeding the downstream tissues with oxygen. Angioplasty, including balloon angioplasty and stent implantation, is a minimally-invasive procedure to widen a narrowed artery in order to facilitate blood flow. In balloon angioplasty, based on X-ray guidance, a balloon catheter is navigated through the vasculature towards the area of stenosis. The balloon which is folded at the distal end of the catheter is inflated and deflated several times to expand the narrowed artery and provide the desired luminal diameter where the luminal diameter is monitored on X-ray. In stent implantation procedures, a stent, i.e. a tubular mesh structure, is mounted on the balloon. When the balloon is deployed, the stent is permanently embedded in the vessel wall to maintain the desired diameter.

1.1 Statement of the problem and objectives

The results of angioplasty are not always permanent. Throughout the history of angioplasty, many patients have been subject to repeat procedures due to a phenomenon called restenosis [13-21], where the artery narrows again after the procedure. Restenosis has been mainly linked to arterial injury during angioplasty which is caused by excessive stretching of arterial walls [14-16].

A large rate of restenosis has been reported for balloon angioplasty [13, 14]. Application of bare metal stents (BMS) improved the rate of restenosis but was prone to in-stent

restenosis [16-18]. The use of drug-eluting stents (DES) further reduced the rates but restenosis remains a problem [19-21]. Moreover, in comparison with BMS, the advent of DES provided a pharmacological approach rather than an improvement in the mechanical approach.

In the current practice of angioplasty, the balloon inflation is performed manually, rendering the results operator-dependent. Excessive or rapid inflation of the balloon could damage the artery. In addition, the applied pressure trajectories to inflate the balloon are not recorded. The pressurization procedure is not standardized which adds to the complexity of comparing the results among different institutions.

During angioplasty, the results are verified by angiography. Although this imaging technique is still the gold standard, it exposes the patients to harmful X-ray. Furthermore, it provides only silhouette views of the vasculature with low resolution. This sometimes is a source of error and discrepancy in estimating the luminal diameter of the arteries [22]. Error in assessment of luminal diameter during the intervention could affect the selection of deployment pressures. In post-angioplasty follow-ups, it could also affect the assessment of restenosis.

The objective of this thesis is to provide methods that could improve development of angioplasty devices, characterization of tissue deformation, modeling and simulation of angioplasty procedures, and balloon inflation strategies.

1.2 Methodology

In order to address the stated problems and achieve the objective, various methods and techniques were used to monitor, characterize, simulate and control the balloon inflation process:

1. Monitoring: We used optical coherence tomography (OCT) [23] to monitor balloon inflation. OCT is a non-destructive imaging modality that provides cross-sectional images of microstructure. Among various OCT techniques, we used swept-source optical coherence tomography (SS-OCT). Catheterized probes allow for intravascular optical coherence tomography (IVOCT). Integration of an IVOCT probe in a balloon catheter provided us with the opportunity to monitor the balloon inflation in real-time.
2. Characterization: Image analysis techniques [24, 25] were applied to IVOCT images to extract the geometry of various structures and characterize their deformation. Using these techniques, different features in an image were extracted to detect balloons, artery phantoms, artery phantom layers, and the lumen of porcine arteries.
3. Simulation: Finite-element analysis [26] was used to simulate experiments involving balloon inflation in air and in artery phantoms. The geometries of the structures were extracted from IVOCT images. Material models were obtained either from uniaxial tensile tests or IVOCT monitoring results. The results of the simulations were compared with the IVOCT monitoring results.
4. Control: Control theory [27] was applied to design feedback loops to achieve desired pressure and diameter during balloon inflation. The diameter control method was experimentally tested. Using this method, the luminal diameter was estimated from IVOCT images in real-time and used in a feedback loop. A controller then controlled the action of a programmable syringe pump to achieve a desired diameter. To control the inflation, the diameter of the lumen is estimated as

that of a circle with the same cross-sectional area. This method is applicable for complex lumen morphologies, providing a good measure of lumen patency.

In various experiments, IVOCT was applied to monitor balloon inflation in air, in artery phantoms, in an artery of an excised porcine heart, and in an artery of a beating porcine heart. Both semi-compliant and compliant balloons were used. The balloons were inflated by a computerized mechanism. Inflation pressures were measured by a pressure transducer. In some experiments, phantoms with various mechanical properties were used. In some experiments, a multi-layer phantom was used with layers simulating artery layers.

1.3 Motivation

Cardiovascular disease is the leading cause of death [28]. For instance, more than 80,000,000 American adults (one in three) have one or more kinds of heart disease and angioplasty is performed on over 1 million patients, costing over 40 billion dollars, every year in the United states alone [29].

Before the invention of stents, up to one third of patients were subject to restenosis [16]. In some reports, stent implantation reduced the rate of restenosis by 10 % [17, 18]. Considering the number of patients who are treated by angioplasty, even a small rate of restenosis affects a significant number of patients.

The presence of a large number of patients suffering from atherosclerosis combined with the shortcomings of angioplasty such as restenosis necessitate constant investigation and development of new methods and tools to improve angioplasty procedures. Further research not only could lead to better long-term results such as a reduction in the rate of restenosis, but also could provide safer conditions for angioplasty which is a safety-

critical procedure. Our research focuses on improving monitoring techniques and balloon deployment strategies.

Improved monitoring could be provided by OCT. OCT has seen tremendous developments over the last few years. The development of high-measurement rate of SS-OCT systems in combination with the availability of catheterized probes led the path to the clear demonstration of the clinical relevance of IVOCT [30]. This imaging method has not yet reached its full potential. In this thesis, we propose new applications of IVOCT.

In the literature, the use of intravascular imaging is suggested, together with angiography, mainly to achieve two goals. The first goal is to achieve a more precise assessment of artery walls [22].The second goal is to achieve a more precise assessment of the results after deployment of a stent [31-34].

The frequently used intravascular imaging modality is intravascular ultrasound (IVUS). In comparison with IVOCT, IVUS provides a better penetration depth. IVUS allows visualizing the vessel wall structure, even when the imaging probe is surrounded by blood. On the other hand, IVOCT has a resolution about 10 times superior to that of IVUS. It has been shown that in comparison with IVUS, IVOCT provides a more accurate assessment of vessel wall layers [35] stent deployment [36] and plaque morphology [37]. The high resolution of IVOCT renders this method an appropriate choice in the proposed applications, i.e. monitoring, characterization, simulation, and control, where precision is essential. Furthermore, in the proposed applications the inflated balloon displaces the blood. Therefore, the blood does not affect the quality of the images.

Deployment strategies could be improved using control methods. Since the first time that Dr. Gruentzig performed angioplasty in 1977, the core of the process has not evolved significantly. The high computational power of today's computers has not been incorporated in the process appreciably. Computer-assisted balloon inflation could improve the procedure. Imaging and image analysis could be performed in real-time. The inflation pressure and volume values could be recorded, leading to a more standard approach to balloon inflation and providing data for statistical analysis. Finally, balloon inflation could be controlled to achieve desired specifications, e.g. pressures and diameters, providing superior results in comparison with the manual inflation approach.

1.4 Contribution

In angioplasty, in order to verify the results of balloon inflation by intravascular imaging, the operator usually has to withdraw the balloon catheter and replace it with an intravascular imaging catheter. Real-time imaging data during balloon inflation are rare. This is due to the complexity associated with using an integrated imaging balloon catheter. We integrated an IVOCT probe in a balloon catheter to monitor the balloon inflation in real-time. This led to development of a setup that satisfied the following objectives:

1. Monitoring of balloon deployment [1, 2]: We provide images acquired during balloon inflation process. These images shed light on the process of balloon deployment. Application of image analysis techniques to IVOCT images, acquired during balloon inflation, resulted in an assessment of balloon diameters and thicknesses at various pressures. Both monitoring and characterization results could be used by researchers to improve mathematical modeling of the balloon

deployment process. They could also be used by balloon manufacturers to validate the performance of a balloon.

2. Monitoring and characterization of phantom deformation [3, 7, 8]: IVOCT imaging during balloon deployment in phantoms resulted in a qualitative assessment of phantom deformation. This method could be applied to monitor the deformation of arteries, and study the conditions which lead to rupture of the vessel wall or vulnerable plaques. Application of image analysis techniques to IVOCT images, acquired during balloon inflation, resulted in an assessment of phantom diameters and layer thicknesses at various pressures. This method could be used to study quantitatively the response of arteries to different balloon dimensions, balloon folding strategies, and balloon deployment strategies.
3. Simulation [4, 9]: In the literature, articles that provide an experimental validation of angioplasty simulation are rare. Furthermore, no concrete method has been suggested to experimentally validate simulation results. In this thesis, we propose IVOCT monitoring and characterization of deformation as a method to validate simulation results. As examples, we present a comparison of finite-element simulation and experimental results for two different scenarios.
4. Real-time control of balloon inflation [5, 6, 10-12]: In angioplasty, balloon inflation is performed manually. Excessive stretch of artery wall could cause injury. In this thesis, we propose control methodologies to control the balloon inflation. This is the first time that the balloon inflation process is formulated as a control problem. Various simulations were performed where the pressure or the diameter was controlled. The diameter control method was experimentally tested when the

balloon was inflated in an artery phantom, in an artery of an excised porcine heart, and in an artery of a beating porcine heart.

The proposed methods and the results could benefit cardiovascular research, medical device industry and clinicians.

1.5 Outline

In Chapter 2, an overview of angioplasty, related intravascular imaging techniques, and restenosis is provided. In Chapter 3, the SS-OCT principles and the experimental imaging setup are presented. A background review of the applied image analysis techniques is provided in Chapter 4. In Chapter 5, an overview of finite-element simulation and the applied software are discussed. The proposed inflation control methods and simulation of these control methods are presented in Chapter 6. The experimental details and results of monitoring and characterization of balloon deformation in a deployment tester are provided in Chapter 7. The experimental details and results of monitoring and characterization of the deformation of phantoms during balloon deployment are presented in Chapter 8. Comparison of finite-element simulation and experimental results is provided in Chapter 9. Chapter 10 presents experimental validation of controlled inflation in an artery phantom. Chapter 11 presents experimental validation of controlled inflation in porcine arteries of an excised heart, and a beating heart model. Concluding remarks and suggestions for future work are included in Chapter 12.

CHAPTER 2: ANGIOPLASTY

A historical overview of angioplasty is provided in [38]. Few innovations in the history have influenced medicine as profoundly as cardiac catheterization. This 60-year-old technique together with angiography has allowed an access to the entire circulatory system, leading to investigational and interventional therapy for cardiovascular diseases. The first time, a surgeon in Germany, Werner Forssman, catheterized his own heart in 1929. He was not satisfied with the existing diagnostic methods of the 1920's. At the time, it sparked controversy. Fear of undesired consequences of invading the heart suspended continuation of such activities until the 1940s. The right ventricle and the pulmonary arteries were accessed in 1942 and 1943, respectively. This helped the first pressure recording and blood gas sampling from the right atrium. Transluminal dilation of leg arteries was first reported in 1964. The first dilation of a stenotic coronary artery using a balloon was performed by Gruentzig in 1977. Since its inception, this technique, known as angioplasty, has been the most commonly performed coronary intervention. However, angioplasty does not always provide a permanent cure. Patients are sometimes subject to repeat procedures due to a phenomenon, called restenosis. In the following, we provide a brief review of angioplasty procedures, vascular imaging, and the related research.

2.1 Angioplasty procedures

The presence of atherosclerotic plaque in the walls of an artery could lead to stenosis (narrowing) of the blood vessel, preventing the oxygen-rich blood from feeding organs. The treatments for such a condition include angioplasty. Angioplasty is a minimally-

invasive intervention, usually performed by an interventional radiologist or an interventional cardiologist, in a catheterization lab.

In balloon angioplasty, a catheter, with a balloon folded at its distal end, is inserted into the patient's body through a needle puncture, usually introduced into the femoral artery. The catheter is navigated through the vasculature towards the area of stenosis. Radio-opaque markers are placed on the tip of the catheter to locate it inside the body, using real-time X-ray images. When the balloon is in place, it is inflated to widen the artery. After a period of maintaining an inflation pressure the balloon is deflated. If the results are not satisfactory, the process of inflation and deflation is repeated several times each successive time usually with higher inflation pressures. When the artery is widened to a desired luminal diameter, the catheter is withdrawn from the patient's body. Balloon angioplasty is demonstrated in Figure 2.1.

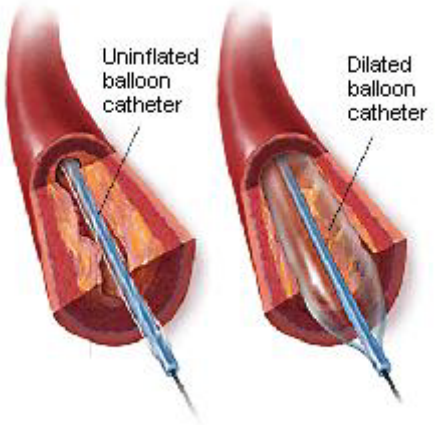

Figure 2.1. Balloon angioplasty (image provided courtesy of Boston Scientific. © 2011 Boston Scientific Corporation or its affiliates. All rights reserved.)

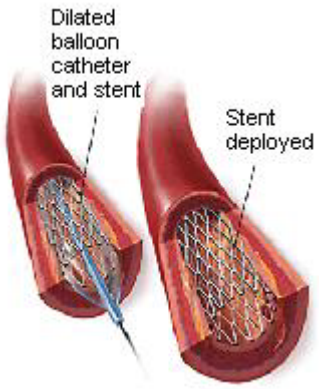

Figure 2.2. Stent implantation (image provided courtesy of Boston Scientific. © 2011 Boston Scientific Corporation or its affiliates, All rights reserved.)

After balloon angioplasty, the artery may return to its original state due to a phenomenon called elastic recoil. This can happen hours after the intervention. Bare metal stents (BMS) were introduced to resolve this problem. BMS are deployable scaffold structures which are mounted on balloon catheters. After the balloon is inflated and the stent is deployed, the stent is implanted permanently in the artery wall and refrains from elastic recoil. Figure 2.2 shows the stent implantation procedure. However, stents have not been the ultimate solution to the problem. An implanted stent is an element that is not native to the body. This results in development of a tissue inside the stent, called neointima. This tissue could sometimes be sufficiently thick to narrow the artery again, causing the so-called in-stent restenosis. The stent in an artery could also trigger the body's immune system. Patients, who are treated by a stent, are asked to take anti-platelet medication, such as aspirin, to prevent formation of blood clots in the stent, known as in-stent thrombosis.

Drug-eluting stents (DES) were introduced to resolve the problems related to BMS. These stents release drugs to prevent hyperplasia (cell proliferation). Several studies confirm superior performance of DES in comparison with BMS. However, DES did not provide an ultimate solution to the problem of restenosis [20].

2.2 Vascular imaging

In this section, we introduce two imaging modalities, namely angiography and intravascular ultrasound (IVUS), which are frequently used in angioplasty.

2.2.1. Angiography

Angiography is an imaging technique in which a radio-opaque contrast agent is injected into the blood vessels while images of the vasculature, called angiograms are being acquired using an X-ray-based technique such as fluoroscopy. For many years, angiography was the only technique to visualize the lumen of blood vessels. Angiograms provide a profile of the vasculature. Upon injection of the contrast agent a narrowing in an artery reveals itself on angiograms. Figure 2.3 demonstrates an angiogram, in which a stenosis is marked by an arrow.

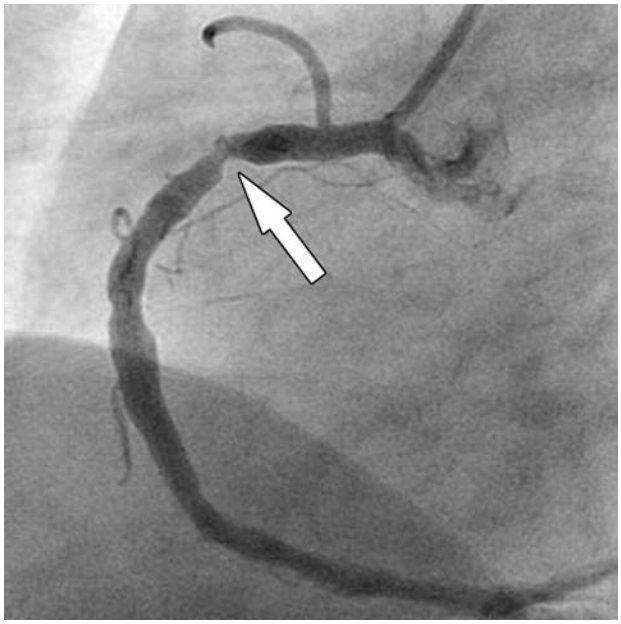

Figure 2.3. Stenosis identified on an angiogram (image provided courtesy of the Radiological Society of North America [39])

2.2.2. Intravascular ultrasound

Intravascular ultrasound (IVUS) imaging devices have been the gold standard to visualize a cross-sectional view of the blood vessel. These devices use a miniaturized ultrasound probe on the distal end of a specially designed catheter, which can navigate through the vasculature and send signals to be processed by the computerized equipment at the proximal end. IVUS could provide not only information about the lumen but also about the plaque behind the inner walls of the vessel, which was not accessible by angiography. The ability to visualize the plaque revealed the fallacy of some previous beliefs about the causes of heart attack and helped better identify culprit lesions. Previously, the hypothesis was that the degree of accumulation of the plaque would determine the cause of acute coronary events. After investigation with IVUS, it was discovered that the type of plaque is the determining factor and most of the time rupture of vulnerable plaque is the reason [40, 41]. Figure 2.4 presents an IVUS image of an artery.

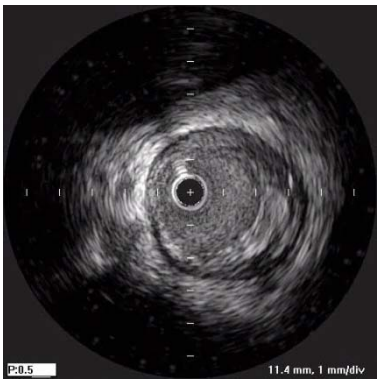

Figure 2.4. An IVUS image of an artery (image source: National Research Council Canada)

2.3 Related research

Although balloon angioplasty became a standard way of dilating the stenotic artery, it started to reveal some shortcomings. Up to one third of patients were subject to repeat

procedures [13, 16]. Since the introduction of stents the rate of restenosis has decreased. However, occurrence of in-stent restenosis is still problematic [19-21].

Some studies found evidence that restenosis and complications in angioplasty are related to the excessive mechanical stretching of the vessel wall during the intervention [14-16]. This led to the development of various approaches addressing the problem from different angles:

1) Intravascular imaging: The discovery of the main reason behind heart attacks, explained in the previous section, motivated some cardiologists to combine IVUS with angiography to study the development of atherosclerosis and restenosis. Some researchers have investigated application of IVUS in verifying the results of angioplasty, e.g., apposition of stent to the vessel wall after it is deployed [31-34]. The use of other intravascular imaging methods, e.g., intravascular optical coherence tomography (IVOCT) [36] and magnetic resonance imaging (MRI) [42], has also been reported.

2) Mechanical analysis: There have been articles where mechanical properties of arteries were characterized [43], with the aim to improve the results of angioplasty. In several articles [44-52] angioplasty is simulated by means of finite-element method.

3) Deployment methodologies: Some researchers investigated computerized inflation of balloons [53]. Such method was also tested in clinical trials [54, 55]. In some articles, computerized recording and use of pressure-volume measurements is suggested in cardiovascular research [56-60] and clinical applications [61, 62].

In this thesis, we propose novel and more advanced methods, inspired from previous research:

1) Intravascular imaging: In the literature, there is generally a lack of experimental data, obtained during balloon deployment. We propose monitoring and characterization, using IVOCT imaging during balloon deployment (Chapters 7 and 8). The results shed light on the interaction between the balloon and the tissue.

2) Mechanical analysis: The application of IVOCT imaging is not limited to monitoring and characterization but can also be extended to modeling and simulation. We propose IVOCT monitoring and characterization results as a method to validate finite-element simulation of balloon inflation (Chapter 9).

3) Deployment methodologies: We propose balloon inflation control methods based on pressure and diameter feedbacks. We present simulation of these methods (Chapter 6) as well as experimental validation of the diameter control method (Chapters 10 and 11).

The proposed research may not only benefit the restenosis research, but more generally it may improve angioplasty device design and procedures.

CHAPTER 3: OPTICAL COHERENCE TOMOGRAPHY

Optical coherence tomography (OCT) is an imaging modality that is now being used in many clinical applications [23], including cardiovascular research [30]. It is a non-destructive imaging technique, divided into two categories: the time-domain OCT (TD-OCT) [63] and the Fourier-domain OCT (FD-OCT) which itself is further divided into spectral domain OCT (SD-OCT) [64, 65] and swept source OCT (SS-OCT), [66-68] also known as optical Fourier domain imaging (OFDI) [69]. Imaging in this thesis was performed with SS-OCT. We thus briefly review SS-OCT principles and describe our SS-OCT setup.

3.1 SS-OCT principles

A basic configuration of the SS-OCT setup is presented in Figure 3.1. The light coming from the wavelength-swept source is split by an optical coupler into two parts, one of which goes into the reference arm and the other into the sample arm. The light reflected from the reference arm with intensity I_r and the backscattered light from the sample with intensity I_s are then combined in the coupler to create interference fringes. Assuming that the sample arm only contains a single reflector, the intensity received by the photodetector is given by:

$$I = I_r + I_s + 2\sqrt{I_r I_s}\cos\left[\frac{2\pi}{c}\upsilon(t)\cdot 2\Delta z\right], \tag{3.1}$$

where c is the speed of light, $\upsilon(t)$ is the optical frequency as a function of time t and Δz is the optical path delay between the two arms of the interferometer. In the presence of

many reflectors, Eq. (1) takes a more complicated form to include a term describing the mutual interference between the reflectors.

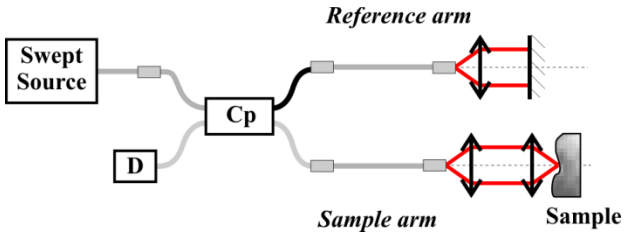

Figure 3.1. Basic configuration of a fibered SS-OCT setup (Cp: coupler, D: detector).

For a source providing an ideal linear sweep in frequency, we have $\upsilon(t) = \upsilon_0 + (\Delta\upsilon/\Delta t)\cdot t$, where υ_0 is the start sweep optical frequency, and $\Delta\upsilon$ is the swept bandwidth during the time interval Δt. Most commercial sources for SS-OCT do not provide such an ideal linear sweep, but the nonlinearity can be corrected with one of the many techniques found in the literature [70-72].

Assuming an ideal linear sweep, the modulation term of the interference fringes is given by:

$$I_{\text{mod}} \propto \cos\left[\frac{2\pi}{c}\upsilon_0 \cdot 2\Delta z + \frac{2\pi}{c}\frac{\Delta\upsilon}{\Delta t}\cdot t \cdot 2\Delta z\right], \tag{3.2}$$

The amplitude of the inverse Fourier transform of I_{mod} is then computed:

$$\left|\mathrm{F}^{-1}\left[I_{\text{mod}}\right]\right| \propto \left[\delta(f - f_1) + \delta(f + f_1)\right] \tag{3.3}$$

where $\delta(f)$ is the frequency domain impulse function and $f_1 = \frac{2\Delta z}{c}\frac{\Delta\upsilon}{\Delta t}$. The depth information Δz is thus recovered by computing:

$$\Delta z = \frac{1}{2}\cdot c \cdot \frac{\Delta t}{\Delta\upsilon}.f_1. \tag{3.4}$$

This simple model demonstrates one of the shortcomings of SS-OCT and FD-OCT in general; one cannot distinguish the positive depths from the negative depths. This is

referred to as the mirror artifact, which is avoided in our system by placing the sample on one side of the zero-delay position in the sample arm.

3.2 Experimental imaging setup

The experimental setup that was applied for OCT imaging was provided by the Industrial Materials Institute (IMI) of the National Research Council (NRC) of Canada. A detailed description of this setup is provided in [73]. This setup was composed of an SS-OCT system, an intravascular optical coherence tomography (IVOCT) probe, and a rotation-translation unit. These elements and their interconnections are illustrated in Figure 3.2. Next, we present a more detailed description of each element.

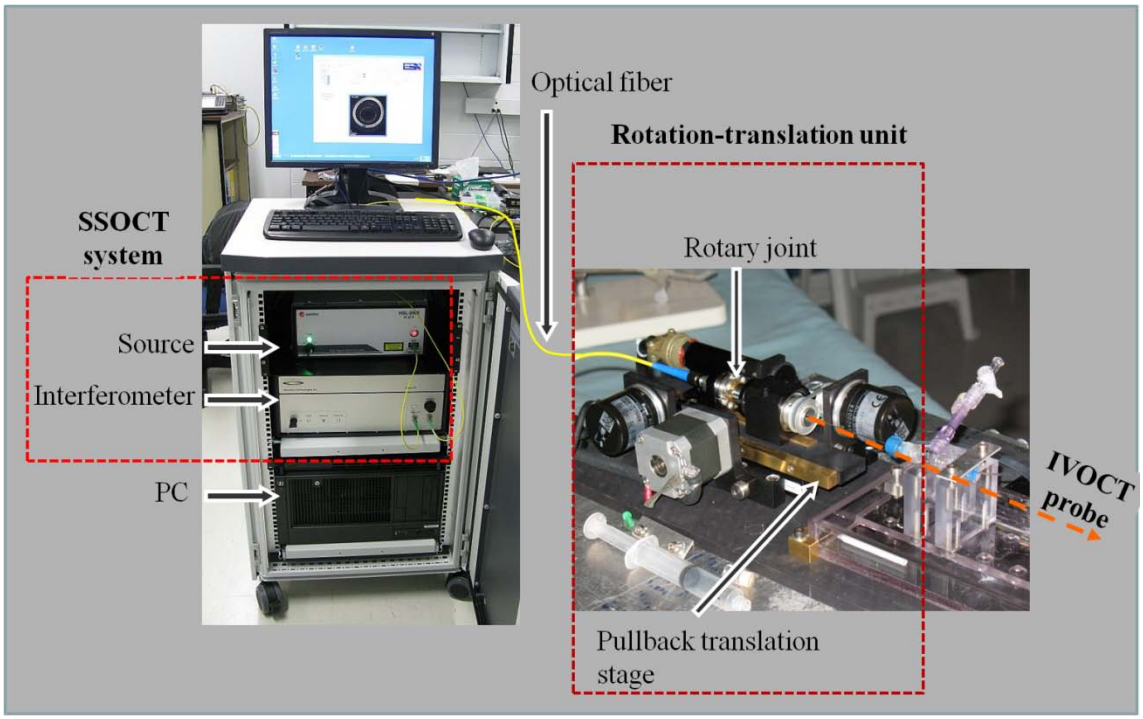

Figure 3.2. Experimental imaging setup

3.2.1. SS-OCT system

We used a custom-built SS-OCT system that operates with a commercial swept source. In the experiments, we used a wavelength-swept laser source (HSL2000, Santec), operating

with a sweep rate of 30 kHz and a sweep range of over 110 nm around 1.31 µm wavelength to provide a measured axial OCT resolution of about 12 µm in air. The SS-OCT system was configured as a Mach-Zehnder interferometer with balanced detection and was packaged as a mobile unit. The setup is presented in Figure 3.3.

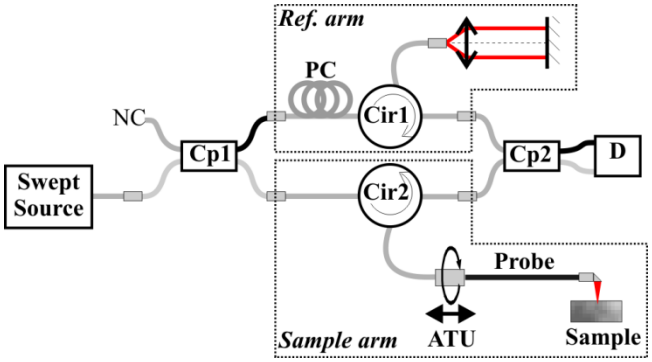

Figure 3.3. Schematic of the SS-OCT setup (Cp1 and Cp2: couplers, PC: polarization controller, Cir1 and Cir2: circulators, D: balanced detection, NC: not connected, ATU: artery testing unit).

3.2.2. IVOCT probe

Figure 3.4 schematically demonstrates the composition of the IVOCT probe. The probe applied in experiments was composed of a single-mode optical fiber (OF) enclosed within a spiral metallic tube in the proximal region and within a polymer tube (PT) in the distal region. At the tip of the probe, the light beam (LB) was focused by a graded index (GRIN) lens and redirected at 90° by a right-angle prism (RAP). The optical components were enclosed in a metallic ferrule (F). The ferrule was 700 µm in diameter but the maximum probe diameter was 800 µm at the spiral metallic tube.

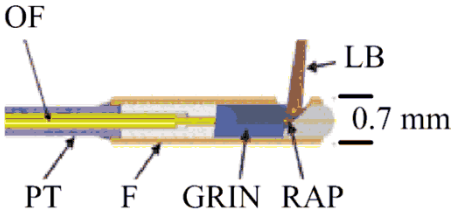

Figure 3.4. Schematic of the IVOCT probe

3.2.3. Rotation-translation unit

Rotation and translation of the probe were ensured by a rotation-translation unit. This unit provided pull-back speeds of 150 μm/s to 2.5 mm/s. SS-OCT imaging was typically performed at 20 to 30 frames per second (FPS). As Figure 3.2 shows, both the SS-OCT system and the IVOCT probe are connected to the rotation-translation unit. In this figure, the optical fiber connecting the SS-OCT system to the rotation-translation unit is depicted by a yellow line.

CHAPTER 4: GRAY-SCALE IMAGE ANALYSIS

A gray-scale image is an image in which each pixel is represented by a scalar, referred to as intensity. Various intensities correspond to various shades of gray. The lowest and the highest intensities correspond to black and white, respectively. A digital gray-scale image can be represented by a matrix. Each element of the matrix corresponds to a pixel in the image. The value of each element provides the intensity for the corresponding pixel.

As IVOCT images are gray-scale images, we discuss some techniques for gray-scale image analysis applied in this thesis. This discussion is divided into three sections, namely, global operations which were applied to improve image display, local operations which were applied for noise reduction and feature extraction, and finally image registration and object characterization achieved as the goals of image analysis.

Figure 4.1(a) shows a synthetic image, used to explain different operations. This image contains features, i.e., a ridge and an edge, which are exploited in later discussions. The image intensity range is [0, 1]. The pixels corresponding to the column, j_0, of the image matrix are marked by red. Figure 4.1(b) presents the intensity profile of this column.

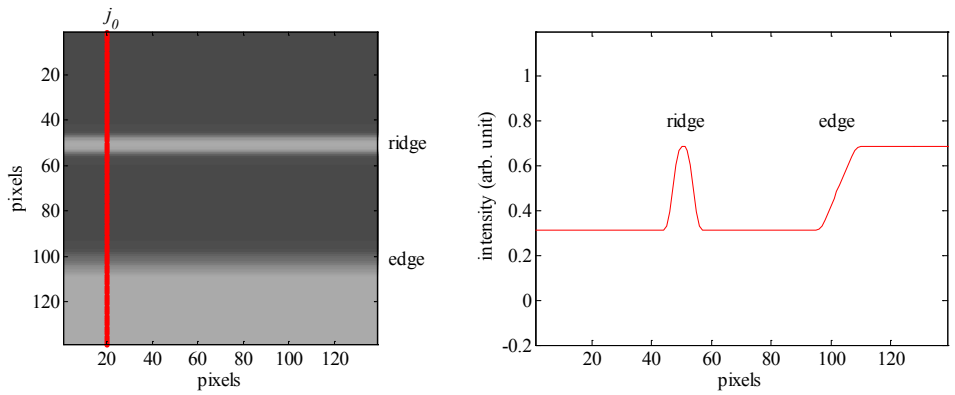

Figure 4.1. A grayscale image (a) and the column j_0 of the corresponding image matrix (b)

4.1 Global operations

A global operation [25] or a point operation [24] treats all pixels in an image identically. It may be independent of pixel values or may incorporate statistics of all pixel values in the image. A global operation is a function, g, applied to the intensity value of each pixel in an image, I, providing a new image, J:

$$J(i, j) = g(I(i, j)). \tag{4.1}$$

Global operations could be linear or nonlinear. Linear global operations apply a linear function g:

$$J(i, j) = a.I(i, j) + b. \tag{4.2}$$

where a is an intensity scaling factor and b is an additive intensity offset.

A tool that is used to design different operations on an image is the image histogram. The image histogram, $H(q)$, is a plot of the frequency of occurrence of each quantized gray level, q, in the image. Figure 4.2 presents the histogram of the image in Figure 4.1(a). This histogram shows that the pixel intensities do not span the full range of [0, 1].

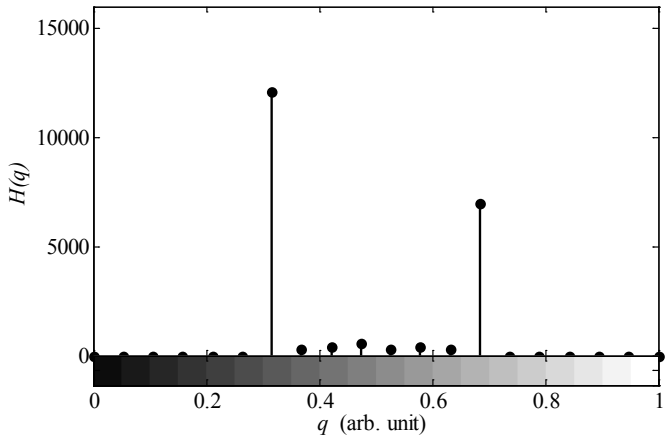

Figure 4.2. Image histogram

A linear operation can be applied to stretch the histogram to the full range to provide a better visual distinction of different regions:

$$J(i,j) = \frac{1}{M-m}(I(i,j)-m), \tag{4.3}$$

where

$$m = \min(I), M = \max(I). \tag{4.4}$$

This operation is called full-scale histogram stretch (FSHS) or contrast stretch [24]. Figure 4.3 demonstrates the result of applying FSHS to the image in Figure 4.1(a). As this figure shows, there is a higher contrast between the bright and dark regions in the new image. The stretched histogram is presented in Figure 4.4.

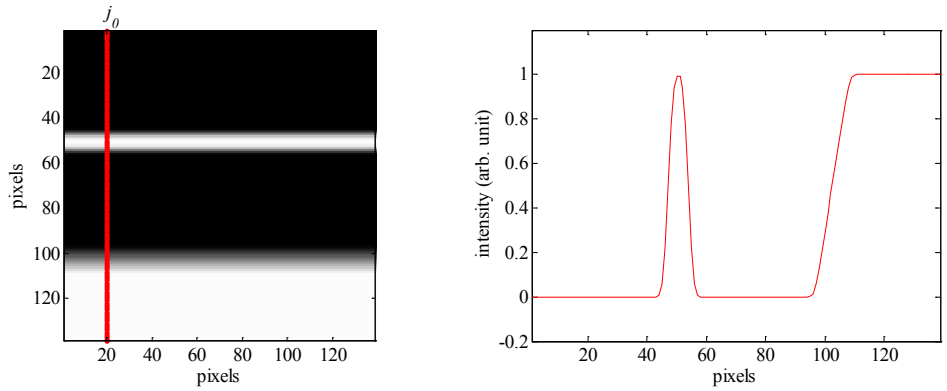

Figure 4.3. The grayscale image obtained from FSHS (a) and the column j_0 of the corresponding image matrix (b)

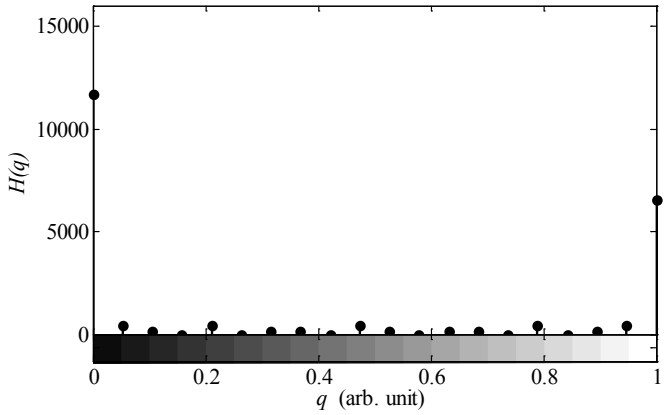

Figure 4.4. Image histogram after application of FSHS

A linear operation can also be used to reverse the bright and dark regions:

$$J(i, j) = 1 - I(i, j). \tag{4.5}$$

Figure 4.5 presents the result of applying this operation to the image in Figure 4.3(a).

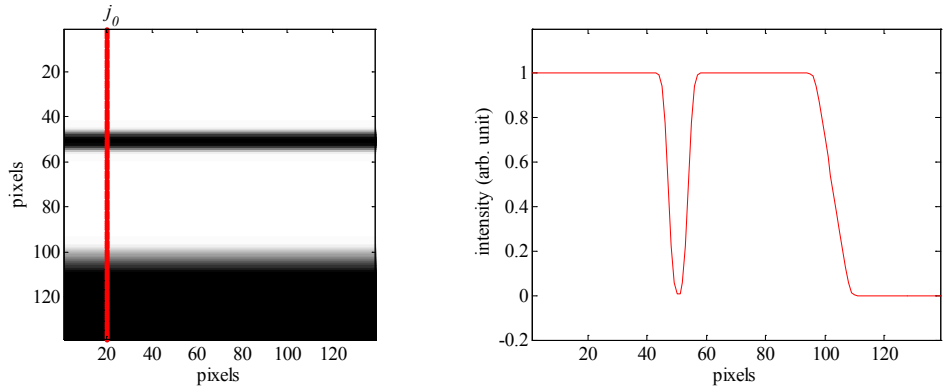

(a) **(b)**

Figure 4.5. The grayscale image after reversing bright and dark regions (a) and the column j_0 of the corresponding image matrix (b)

The operation g in (4.1) can also be defined by a nonlinear function. An example is a logarithmic function to display intensities on a logarithmic scale. The intensities can be scaled to span the range of [0, 1] on a logarithmic scale:

$$J(i, j) = \frac{\log(\frac{1}{m} I(i, j))}{\log(\frac{M}{m})}, \tag{4.6}$$

where m and M are defined in (4.3).

In IVOCT images, we used global operations to adjust contrast and brightness to improve image display.

4.2 Local operations

Local operations are adaptive operations which are dependent on regional pixel values. We applied local operations for noise reduction and feature extraction in IVOCT images.

A feature, e.g., an edge or a ridge, may also be detected, based on the intensity properties of that feature. Various objects in images are usually recognized by edges or ridges. A ridge and an edge are identified in Figure 4.1. A ridge in a two-dimensional image is a curve that is formed by points that are local maxima of the intensity in at least one direction. An edge is a curve that is formed by points at which there exist sharp variations or, in mathematical term, discontinuities in intensity. Detection of an object can be performed by detection of edges and ridges. Most of the time, an image not only provides a manifestation of the objects of interest, known as signal, but also those that are not of interest, known as noise. Noise reduction facilitates extraction of features in an image.

In many algorithms in order to reduce noise or to enhance or detect a feature, such as an edge or a ridge, a convolution is performed to replace each pixel value of an image matrix, $I_{X\times Y}$, with a weighted average of a set of pixels in its neighbourhood. The weights are obtained from a discrete approximation, $h(i,j)$, of the analytical form of a desired filter and are included in a matrix, $H_{P\times Q}$, known as a filter mask or a convolution kernel [25]. A mask has odd dimensions, P and Q, which determine the size of the applied neighbourhood. These dimensions are usually much smaller than the image dimensions, X and Y. The two-dimensional convolution is defined as:

$$I_H(i,j) = I * h = \sum_{n=j-\frac{Q-1}{2}}^{j+\frac{Q-1}{2}} \sum_{m=i-\frac{P-1}{2}}^{i+\frac{P-1}{2}} I(m,n)h(i-m,j-n), \tag{4.7}$$

where I_H is the image obtained from convolution. Similar to convolution, given by (4.7), a cross-correlation may be performed, where the filter h, is no longer reversed.

A feature in an image possessing a known shape, size, or orientation may be extracted directly by matching a template of that feature in the image. In this method, a filter mask

is generated as a sub-image providing a template of the feature. The pixel that maximizes the cross-correlation of the image with the template filter is detected as it locates the feature of interest in the image. In the following, we explain some of the techniques applied for noise reduction, edge detection and ridge detection in an image.

4.2.1. Noise reduction

Noise may come from various sources in electronic or optical instruments. In image analysis, objects that are not of interest could also be considered as noise. The noise may be reduced using various filtering techniques. In order to discuss some of these techniques, we synthetically add noise to the image in Figure 4.1(a). Usually a component of image noise is referred to as speckle noise or salt-and-pepper noise. Salt-and-pepper noise is usually reserved to binary images, where the pixel values are either 0 or 1. Although our sample image in Figure 4.1(a) is not a binary image, we use salt-and-pepper noise as it allows for a more clear demonstration of the filtering methods. Figure 4.6 shows the result of applying salt and pepper noise to the image in Figure 4.1(a). The density of the applied noise is 0.04. Noise reduction can be performed using linear or nonlinear filters.

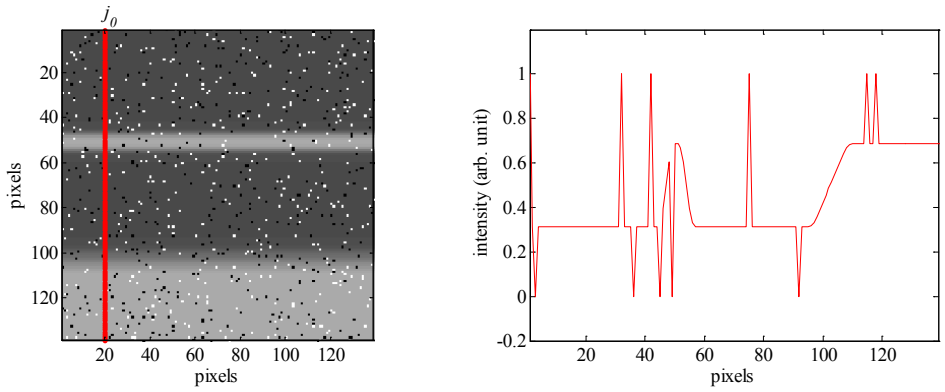

(a) **(b)**

Figure 4.6. The grayscale image after adding salt and pepper noise (a) and the column j_0 of the corresponding image matrix (b)

4.2.1.1. Linear filters

The simplest linear filter to reduce noise is the uniform filter [25]. This filter provides a moving average operation, replacing each pixel intensity with the average of intensities of pixels within a defined neighbourhood to smooth sharp transitions in intensity. Application of a uniform filter is equivalent to application of a mask with all elements equal to 1. Figure 4.7 presents the result of applying a uniform filter to the image in Figure 4.6(a) using a 3×3 mask. As this figure shows, the amplitude of noise is reduced at various pixels. Some pixels have become noisy as a result of averaging with noisy pixels. These pixels constitute gray patches around noisy pixels.

In designing a smoothing filter, larger weights could be allocated to the central pixels. An example is a Gaussian filter, h_g, with standard deviation, σ, in both directions, providing a bell-shaped surface, given by:

$$h_g(i,j) = \frac{1}{2\pi\sigma^2} e^{\frac{-(i^2+j^2)}{\sigma^2}} \tag{4.8}$$

For an $R \times R$ mask, $-(R-1)/2 < i, j < (R-1)/2$. Application of Gaussian filter is slower than a uniform filter as it requires both multiplication and summation.

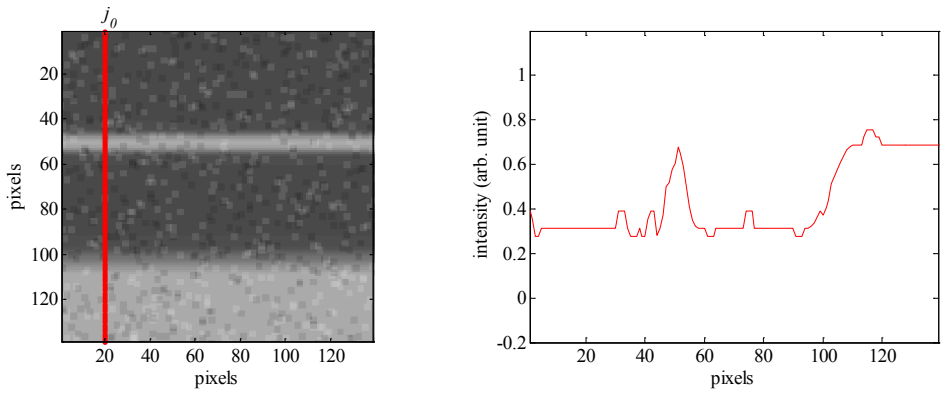

(a) **(b)**

Figure 4.7. The grayscale image after application of a uniform filter (a) and the column j_0 of the corresponding image matrix (b)

4.2.1.2. Nonlinear filters

A commonly applied nonlinear filter is a median filter which can effectively reduce speckle and salt and pepper noise without corrupting or displacing image features such as edges. Application of a median filter replaces the intensity of each pixel with the median value of intensities of pixels within a defined neighbourhood. Figure 4.8 shows the result of applying a median filter in a 3×3 neighbourhood of all pixels in the noisy image of Figure 4.6(a). As this figure shows, the median filter has eliminated the noise in most of the image. This can also be verified more clearly on the presented profile for the column j_0. In IVOCT images, a median filter was mostly used to reduce noise.

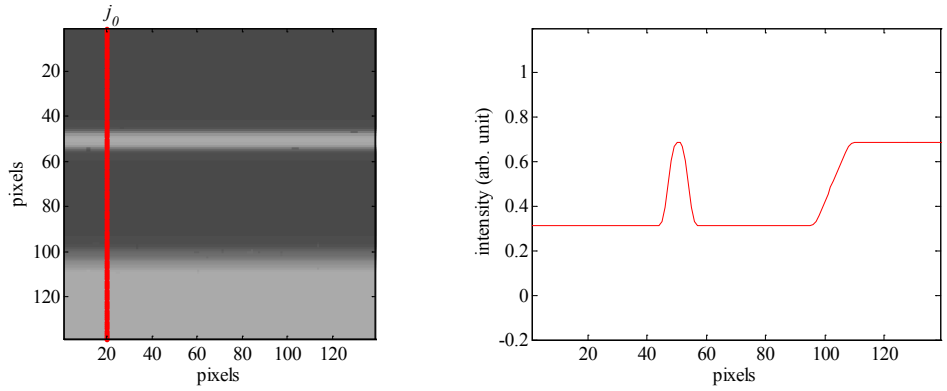

(a) **(b)**

Figure 4.8. The grayscale image after application of a median filter (a) and the column j_0 of the corresponding image matrix (b)

4.2.2. Ridge detection

A discussion on different definitions of a ridge is presented in [74].Various ridge-based methods have been used in different applications, e.g., extraction of roads in aerial images [75] and segmentation of vessel trees [76]. In IVOCT images, reflection of light at the interface between two structures generates peaks in intensity. These peaks form a ridge in the IVOCT images. Therefore, detection of a ridge leads to detection of interface between different structures.

The ridge in Figure 4.1(a) can be detected by detecting the corresponding peaks on various columns in the image matrix. The techniques to detect a peak include detection of a local maximum, detection of a local null value of the first derivative along with a negative value in the second derivative, or extraction of the peak position after curve fitting. The results can be improved by applying an initial filtering to reduce noise.

In general, peak detection in one dimension does not provide the desired robustness, since images are usually noisy and ridges take more complex shapes. In order to improve robustness, a method can be applied based on the rotating kernel transformation [77]. In this method, the image is convolved with various filters each representing a line segment at a particular angle. An example set of filters and corresponding masks is presented in Figure 4.9. A pixel on a ridge maximizes the convolution with the filter corresponding to the angle of the tangent to the ridge at that pixel. In this way, weights are assigned to the neighbouring pixels to decide whether a pixel belongs to a ridge. This method can be used to extract lines and curves in an image. In IVOCT images, ridge detection is performed based on this method.

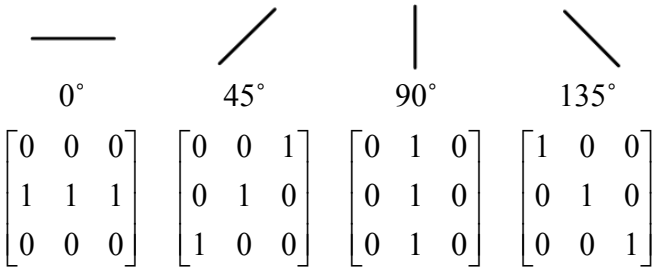

Figure 4.9. A rotating kernel and the set of corresponding masks

4.2.3. Edge detection

Edge detection techniques are commonly used to segment images and to distinguish various objects in an image. In IVOCT images, the average intensity corresponding to various structures is different. This causes a change in intensity at the interface between

the structures, forming an edge in the image. Similar to a ridge, an edge may also correspond to the boundary between two structures in an IVOCT image.

As an edge marks a change in intensity, the most direct method to edge detection is based on finding the local extrema of the first derivative. The edge in Figure 4.1(b), may be detected as a local maximum of the derivative of the vector given by column j_0. To detect an edge in a two-dimensional image, the gradient is used. The gradient ∇ of a function f of two variables, x and y, is defined as:

$$\nabla f(x,y) = \frac{\partial f(x,y)}{\partial x} u_1 + \frac{\partial f(x,y)}{\partial y} u_2, \tag{4.9}$$

where u_1 and u_2 are the unit vectors in the x and y directions. Since the goal is to detect edges in digital images, discrete approximations to derivative operators are used. The discrete-space gradient estimate $\hat{\nabla}$ of an image, I, can be calculated as:

$$\hat{\nabla} I(i,j) = I_1(i,j) v_1 + I_2(i,j) v_2, \tag{4.10}$$

where v_1 and v_2 are the unit vectors in the direction of the discrete-space variables i and j, and:

$$\begin{cases} I_1(i,j) = I(i,j) * h_1(i,j), \\ I_2(i,j) = I(i,j) * h_2(i,j), \end{cases} \tag{4.11}$$

where h_1 and h_2 are derivative approximation filters in orthogonal directions. A simple approximation is the central difference [24], providing:

$$\begin{cases} I_1(i,j) = \frac{1}{2}\left[I(i+1,j) - I(i-1,j)\right], \\ I_2(i,j) = \frac{1}{2}\left[I(i,j+1) - I(i,j-1)\right]. \end{cases} \tag{4.12}$$

Filters, h_1 and h_2 correspond to the central difference masks, H_1 and H_2 :

$$H_1 = \begin{bmatrix} 0 & 0 & 0 \\ -1 & 0 & 1 \\ 0 & 0 & 0 \end{bmatrix}, H_2 = \begin{bmatrix} 0 & -1 & 0 \\ 0 & 0 & 0 \\ 0 & 1 & 0 \end{bmatrix}. \tag{4.13}$$

For detection, smoothing filters can be used to reduce the noise. When applying a linear smoothing filter, it does not make a difference if the filter is applied before or after the gradient operation. Because based on the differentiation property of convolution, for a function, f, and a smoothing filter, h, we have:

$$\nabla(f * h) = \nabla f * h. \tag{4.14}$$

Various derivative operators have been constructed based on combining the central difference operator with a smoothing filter. For example, the Prewitt operator [25] combines this operator with a uniform filter, and the Sobel operator [25] combines it with a Gaussian operator.

In addition, based on the differentiation property of convolution, we have:

$$\nabla(f * h) = f * \nabla h, \tag{4.15}$$

Therefore, the image may also be directly convolved with the difference of the smoothing filter. For example the image can be convolved with a difference of boxes filter or the derivative of a Gaussian filter as shown in [78]. Therefore, the detection filter can be designed based on the edge template.

In a 1D space, an edge can also be detected as the zero-crossing of the second derivative. This inspires Laplacian-based methods, e.g., Laplacian of Gaussian (LoG) method [79], for edge detection in 2D images.

4.3 Image registration and object characterization

Extraction of features in an image may provide information for image registration. The extracted features could also be used to identify and characterize different objects in the image.

4.3.1. Image registration

In different applications, various images of a scene may need to be aligned because of different factors, e.g., displacement of the imaging device. The process of aligning images of a scene is known as image registration [80]. In this process the coordinates of various images may be unified using the coordinates of a number of corresponding points. The set of these points can be detected as image features.

In our experiments, IVOCT images needed to be registered because of the variability of depth in various images. As will be explained, the prism surface was first detected in all images. All images were then registered based on the detected position of the prism surface.

4.3.2. Object characterization

Extraction of features in an image can provide information about the geometry of various objects in the image. The coordinates of the extracted features should be transformed from pixel values to distance values with appropriate units, e.g., millimeters. In IVOCT images the coordinates were first obtained in optical distance, i.e., the product of the geometrical distance and the refractive index. Then these values were converted to true geometrical distances. In IVOCT images, this resulted in characterization of diameters and thicknesses of balloons, artery phantoms and porcine arteries.

CHAPTER 5: FINITE-ELEMENT SIMULATION

An overview of the finite-element method, its concepts, and its applications is provided in [26]. Finite-element method is a numerical method to analyze problems that are too complex to be solved by analytical techniques. It is used in various applications to analyze deformation, stress, temperature, etc. In this method, many algebraic equations are generated and solved simultaneously on a computer.

To apply the finite-element method to analyze deformation and stress, the following steps need to be taken:

1) Divide the geometry of each structure into finite elements and generate a mesh.

2) Specify the mechanical properties of each material.

3) Specify the boundary conditions for the structure, e.g., where it is fixed.

4) Identify the node groups in the mesh that are subject to various forces.

Next, we provide a brief overview of constitutive modeling, as it was used to specify mechanical properties of materials.

5.1 Constitutive modeling

A constitutive equation provides the relationship between the stress and the strain in a material. An overview of cardiovascular solid mechanics, including definitions of various stress and strain tensors, is provided in [81].

The simplest constitutive equation is provided by Hooke's law, where the relationship between the stress and the strain is linear. A common form of Hooke's law for an isotropic material in tensor notation is given by:

$$\sigma = \frac{E\upsilon}{(1+\upsilon)(1-2\upsilon)} tr(\varepsilon)\cdot \mathrm{I} + \frac{E}{1+\upsilon}\varepsilon \tag{5.1}$$

where σ is the stress tensor, ε is the strain tensor, E is Young's elastic modulus, υ is Poisson's ratio, I is the second-order identity tensor and $tr(.)$ is the trace operator. In our simulations, phantoms were modeled as isotropic linear elastic materials.

For polymer and biological tissue, the relationship between the stress and the strain is in general nonlinear. A hyperelastic material is a material for which there exists a strain energy function whose derivative with respect to strain provides the stress. Ogden material model [82] can be used to model nonlinear stress-strain relationship for complex materials. The strain energy function for this model is given by:

$$W = \sum_{i=1}^{n} \frac{\mu_i}{\alpha_i} (\lambda_1^{\alpha_i} + \lambda_2^{\alpha_i} + \lambda_3^{\alpha_i} - 3), \tag{5.2}$$

where $\lambda_j, j = 1,2,3,$ are the principal stretch ratios (square roots of the eigenvalues of the right Cauchy-Green tensor) and μ_i, α_i and n are material constants. Various stress tensors can be obtained based on the derivative of this energy function with respect to λ_j. In our simulations, an Ogden model was used to generate a simulation model for the balloon.

Next, we describe the in-house finite-element software, which was used in the simulations in this thesis.

5.2 In-house FEM software to simulate angioplasty

Previously, finite-element software, called Qform, was developed at the Industrial Materials Institute (IMI) of the National Research Council (NRC) of Canada. This software has been used to simulate angioplasty [83]. To describe a simulation procedure

for Qform, one needs to specify the inputs, the applied solving protocol, and the outputs in a "Definition" file.

5.2.1. Inputs

The inputs to the software comprise mesh files, mechanical properties for each material, boundary conditions, and loading conditions.

5.2.1.1. Mesh

The mesh files can be stored in different formats. In Qform, the PATRAN file format is used. The first step in generating a mesh is to define a grid of nodes as the vertices of the elements to be constructed. Various methods could be applied to construct elements based on the generated nodes. For example, for a set of points, S, in the same plane the Delaunay triangulation [84], $T_D(S)$, generates triangular elements in such a way that no point is inside the circumcircle of any triangular element. In a PATRAN file, each element is defined by its vertices together with a unit normal. In angioplasty simulation, mesh files should be provided for the balloon, for the artery, and if applicable, for the stent.

5.2.1.2. Mechanical properties

A mesh may represent a structure composed of different materials with different mechanical properties. The mechanical properties of each material are provided in the definition file. Different constitutive models can be used, e.g., linear elastic and Ogden. In angioplasty simulation, mechanical properties should be provided for the balloon, the artery, and if applicable, for the stent.

5.2.1.3. Boundary conditions

In the definition file, one can specify how a structure is supported. In angioplasty simulation, a node on the outside of the artery or the artery phantom can be fixed to avoid rigid translation when the load is applied.

5.2.1.4. Loading conditions

In the definition file, the nodes that are subject to loading conditions are specified. In angioplasty simulation, these nodes correspond to the balloon mesh, as the pressure is applied inside the balloon. The goal is to simulate the response of tissue, for a pressurization range of interest. The pressurization range is divided into a number of loading steps. The size and the number of steps are also determined in the definition file. The results are calculated and saved at the end of each loading step.

5.2.2. Solving protocol

An iterative or a direct method can be used for solving the equations corresponding to each load step. An iterative method generates a sequence of improving approximations to a solution. A direct method, on the other hand, applies a finite sequence of operations. An example is using the Gaussian elimination method to solve a system of equations. Iterative methods are used for nonlinear problems. They are also used for linear problems with a large number of variables. In Qform, the choice of the solver may be defined in the definition file. Additionally, various criteria, such as the maximum number of iterations or tolerance values, are provided in the definition file as the criteria to stop the iterations at each load step.

5.2.3. Outputs

In the definition file, the node groups of interest can be identified. In angioplasty simulation, these nodes can be the ones corresponding to the artery borders, or the ones corresponding to the balloon. As a result of the simulation, different data could be saved, including strain and stress, corresponding to the specified node groups.

5.3 Interface with intravascular imaging

An interface was generated previously at IMI, where Qform could be provided, with geometries extracted from segmented intravascular ultrasound (IVUS) images, and the corresponding mechanical properties. The tissue's response could then be simulated for various balloons and stents.

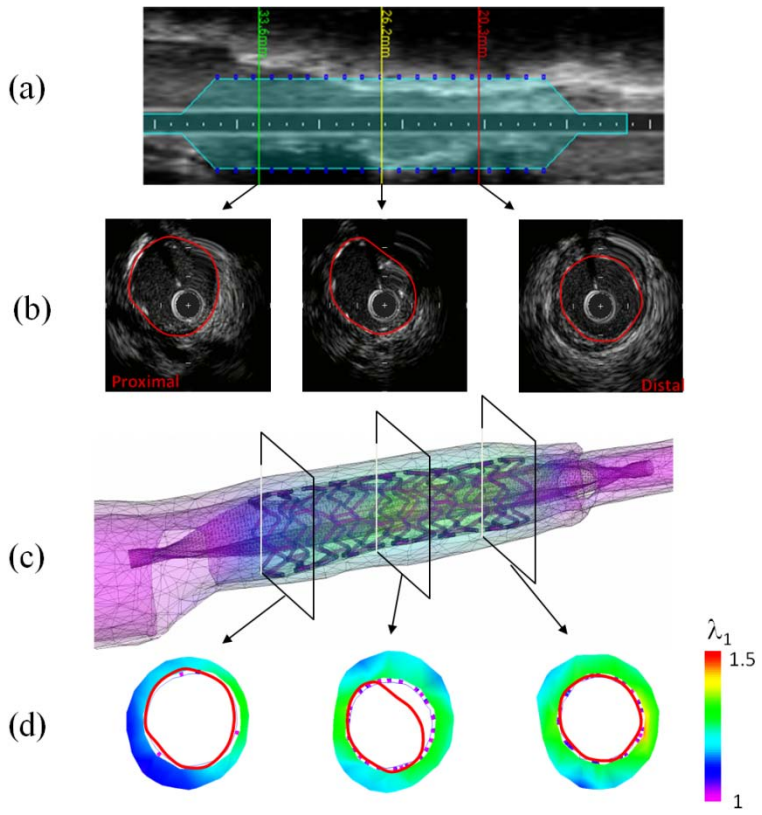

Figure 5.1. Side view of artery (a), cross-sectional images (b), meshing (c), and simulation results (d)

We present an example case where simulation is performed based on acquired IVUS images. As Figure 5.1(a) demonstrates, a side view of the artery is generated based on the IVUS images acquired during a pullback. Based on the luminal reference diameter of the artery, a balloon or a stent-mounted balloon of desired dimensions can be selected. In Figure 5.1(a), the balloon can be distinguished in green and the stent is represented by blue markers on the balloon. Three cross-sections of interest can be chosen, which are demonstrated by the vertical red, yellow and green lines at various depths. Figure 5.1(b) presents the IVUS images corresponding to the three selected cross-sections. In these images, the luminal borders are demonstrated by red contours. Figure 5.1(c) shows the geometric models generated for the balloon, stent, and the artery. Finally, Figure 5.1(d) provides examples of simulated deformation profiles. In Figure 5.1(d), the red contours correspond to the initial lumen border. The dots represent stent struts after deployment. The deformation for various regions can be analyzed by color-coded graphs.

5.4 Validation

IVUS images, such as those in Figure 5.1(b) are not acquired during balloon inflation. In order to validate the results of the finite-element simulation, we propose application of IVOCT imaging during balloon inflation. Example scenarios of simulation and experimental results are provided in Chapter 9.

CHAPTER 6: BALLOON INFLATION CONTROL

One of the goals of this thesis is to introduce angioplasty as a novel field for application of control engineering methods. In angioplasty procedures, balloon inflation is performed manually, where excessive or rapid inflation of the balloon could damage the artery. Computerized balloon inflation control can improve the procedure by providing desired pressures and diameters and by reducing arterial damage. Although in the literature, some researchers and clinicians have proposed computerized balloon inflation [53-55], no formal control theories have been presented. In [53, 54], inflation pressure is controlled. In [55] a computerized gradual inflation is applied without any control.

In this chapter, we propose balloon inflation control, based on the inflation pressure and the luminal diameter. For various scenarios, we present simulation results. The experimental validation of the diameter control scenario is presented in Chapters 10 and 11. First, we present an experimental angioplasty simulation setup to introduce some experimental elements as well as theoretical concepts that are discussed subsequently. Then, we present methods to control inflation pressure and luminal diameter of the artery. At the end, we provide the concluding remarks.

6.1 Experimental angioplasty simulation setup

Figure 6.1 demonstrates the components and their interconnections in an angioplasty simulation setup. This setup emulates the practice of manual balloon inflation. A syringe is used to inflate the balloon. Although the volume is not commonly measured in angioplasty, it can be measured using various methods, e.g., by using an encoder to determine the relative position of the plunger. A pressure transducer can be used to

measure the pressure. The balloon can be inflated to deform an artery phantom or an excised artery in a saline bath at a temperature of 37˚C.

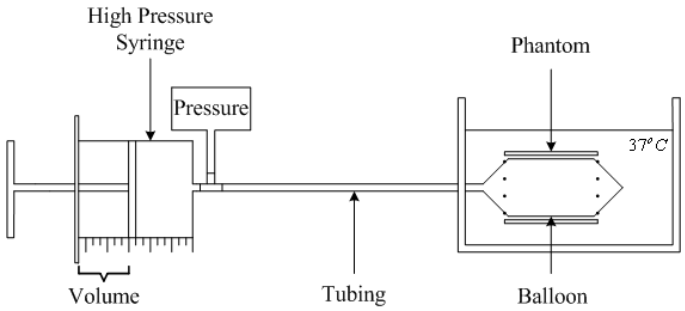

Figure 6.1. Interconnection between components in a balloon inflation setup

A concept that we use in this chapter to discuss the control methods, is the compliance. In cardiovascular physiology [85], the compliance, C, of a hollow structure is defined as the variation of the measured volume, ΔV, with respect to the variation of the measured pressure, ΔP:

$$C = \frac{\Delta V}{\Delta P}. \tag{6.1}$$

In classification of balloons, this definition is modified as the variation of the balloon diameter versus pressure. Balloons can be divided into three categories, namely, non-compliant, semi-compliant, and compliant balloons. Typical diameter-pressure curves for these three types of balloons are demonstrated in Figure 6.2. A non-compliant balloon has a nominal diameter, D_0. Ideally, after the nominal diameter is achieved, a non-compliant balloon does not achieve larger diameters by further pressurization until it reaches its burst pressure. Diameter-pressure curve for a non-compliant balloon is shown in Figure 6.2(a). Similar to a non-compliant balloon, a semi-compliant balloon has a nominal diameter, D_0. However, As shown in Figure 6.2(b), it can still be inflated to diameters slightly larger than its nominal diameter. A compliant balloon does not have a nominal

diameter. It can be continuously inflated until it reaches its burst pressure. As Figure 6.2(c) shows, the diameter of the compliant balloon increases at a growing rate at higher pressures.

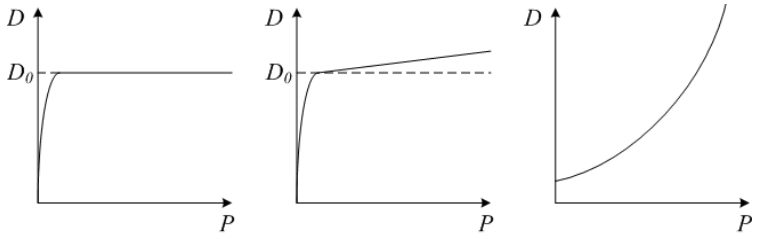

(a) **(b)** **(c)**

Figure 6.2. Diameter-pressure curves for a non-compliant (a), a semi-compliant (b), and a compliant (c) balloon

Although for classification of balloons the compliance is defined based on the diameter, in all other discussions we use the definition in (6.1). Some researchers [59, 60] have assumed that the compliance of the non-compliant balloon inflated in air is in parallel with the compliance of the system (composed of syringe, tubing, connectors, pressure transducer, etc.). For such a system, the pressure, which is applied to the balloon and to the system, is the same and is equal to the pressure in the medium. Therefore, denoting the system pressure by P_S, the balloon pressure by P_B, and the medium pressure by P, we have:

$$P_S = P_B = P. \tag{6.2}$$

The cumulative volume change, ΔV, due to the pressure change, ΔP, is the summation of the volume change in the system, ΔV_S, and the volume change in the balloon, ΔV_B, obtained from:

$$\Delta V = \Delta V_S + \Delta V_B. \tag{6.3}$$

If we respectively, define the compliance of the system and the balloon, C_S and C_B as:

$$C_S = \frac{\Delta V_S}{\Delta P_S}, C_B = \frac{\Delta V_B}{\Delta P_B}, \tag{6.4}$$

by using (6.2) and (6.3), we obtain the aggregate compliance as:

$$C = \frac{\Delta V}{\Delta P} = \frac{\Delta V_S + \Delta V_B}{\Delta P} = \frac{\Delta V_S}{\Delta P_S} + \frac{\Delta V_B}{\Delta P_B} = C_S + C_B. \tag{6.5}$$

Assuming that the system has a small compliance, the measured pressure and volume in Figure 6.1 can provide an estimate of the compliance of the balloon. When the balloon is inflated in a surrounding structure, such as a phantom or an artery, these measurements provide an estimate of the compliance of the combination of the balloon and the surrounding structure. Although, (6.1) provides a definition of compliance based on linearization, in our formulations, we use the generally nonlinear relationship between the pressure and volume measurements:

$$P = F_{PV}(V), \tag{6.6}$$

where F_{PV} is a nonlinear function. Figure 6.3 demonstrates a typical graph for the function F_{PV}.

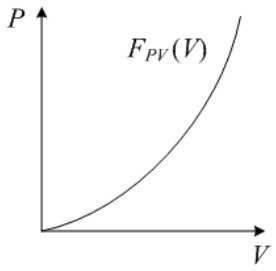

Figure 6.3. A typical pressure-volume curve

6.2 Pressure control

The first control method is based on pressure feedback to inflate the balloon to desired pressures. Let us consider the setup in Figure 6.1. Instead of using a manual syringe, one may use a programmable syringe pump, which can deliver or withdraw liquid with a

desired flow rate. A control problem can be formulated as that of finding the flow rate which provides the desired pressure trajectory. We propose two control methods. The first method is based on a proportional feedback and the second method is based on online estimation of the compliance curve.

6.2.1. Proportional control

Figure 6.4 demonstrates how pressure measurements can be used in a feedback loop to control the balloon inflation. In this figure, the role of each element is interpreted in the context of a conventional control system, composed of an actuator, a plant, a sensor, and a controller:

1) The actuator is a programmable syringe pump to deliver or withdraw liquid with flow rate f. The volume of liquid, V, is used to inflate or deflate the balloon.

2) The plant is the relationship between the volume and the pressure, F_{PV}.

3) The sensing is provided by a pressure transducer to measure the inflation pressure, P.

4) The controller is implemented in a personal computer (PC). It calculates the flow rate, f, based on the error, e, defined as the difference between the desired pressure trajectory, P_d, and the measured pressure, P. The controller then sends the flow rate value as a command to the pump.

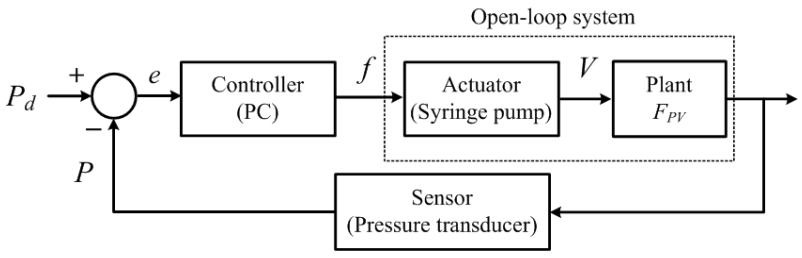

Figure 6.4. Inflation control based on pressure feedback

A state-space representation [27] for the open-loop system can be obtained as:

$$\begin{cases} \dot{x}(t) = u(t) \\ y(t) = F_{PV}(x(t)) \end{cases} \tag{6.7}$$

where t is the time variable, $x(t) = V(t)$, $u(t) = f(t)$, and $y(t) = P(t)$.

In the closed-loop system, the objective is to achieve a desired output, $y_d(t) = P_d(t)$. A proportional output feedback control can be used as:

$$u = k_p(y_d\text{-}y) = k_p(y_d\text{-}F_{PV}(x)). \tag{6.8}$$

In experiments, the actual pressure can be measured by a pressure transducer. In the simulations, it was calculated as the output of the function, $F_{PV}(x)$. For the purpose of simulation, in order to provide a function curve similar to the one in Figure 6.3, let us assume that the plant is given by:

$$F_{PV}(V) = V^{\alpha}, \tag{6.9}$$

where α is a positive constant integer. Figure 6.5 demonstrates the performance of two proportional controllers, with proportional gains of 0.5 mL(atm·s)$^{-1}$ and 1.5 mL(atm·s)$^{-1}$ for the plant given by (6.9) when $\alpha = 2$. This figure presents the simulated pressure, error in pressure, flow rate and volume. In an angioplasty procedure [86], first, the pressure is increased to a predetermined value and maintained for a period of time. Subsequently, the pressure is increased to a larger value either directly after the first pressurization phase or after deflation of the balloon. The process is continued until desired results are achieved. Using a controlled inflation system provides more opportunities and more accurate conditions. At higher pressures, the pressurization rate can be decreased, with the aim to reduce the risk of arterial injury. In addition to reducing the pressurization rate at higher pressures, the size of the pressurization step can be reduced. These factors were

considered in generating the desired pressure, shown by a dashed line in the pressure graph of Figure 6.5. As this figure shows, the desired pressure was composed of two consecutive phases of pressurization. In each phase it was increased following a ramp-shaped function of time. The first ramp had a slope of 0.50 atm/s and the second ramp had a slope of 0.25 atm/s. The first pressure step was 3 atm and the second pressure step was 1.5 atm. Figure 6.5 confirms that in both cases, the simulated pressure tracked the desired trajectory. Furthermore, increasing the proportional gain, from 0.5 $mL(atm \cdot s)^{-1}$ to 1.5 $mL(atm \cdot s)^{-1}$, resulted in better tracking.

In both cases, the steady-state error converged to zero for a constant pressure target and converged to a constant value for a ramp pressure target. The presence of an integration operation in the open loop system, corresponding to the syringe pump, generates the dynamics of a type 1 system [27], which is consistent with this observation of the steady-state error. One solution to eliminate the constant steady-state error for the ramp is the addition of an integral term to construct a proportional-integral control law. This, however, is achieved at the price of introducing oscillations and less stability in the system.

Figure 6.6 demonstrates the simulation of the performance of the proportional controller, with a gain of 0.5 $mL(atm \cdot s)^{-1}$ for a variable degree of nonlinearity in the plant, given by (6.9), when $\alpha = 2$ and $\alpha = 4$. As can be seen, the controller provides better tracking for the plant corresponding to $\alpha = 4$. This plant provides a smaller compliance, resulting in faster dynamics for the convergence of pressure values.

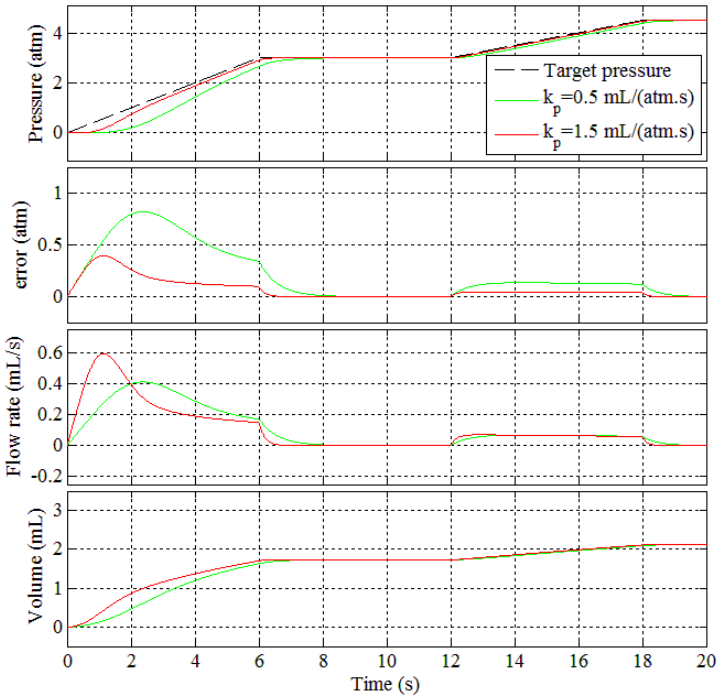

Figure 6.5. Proportional control for two different gains

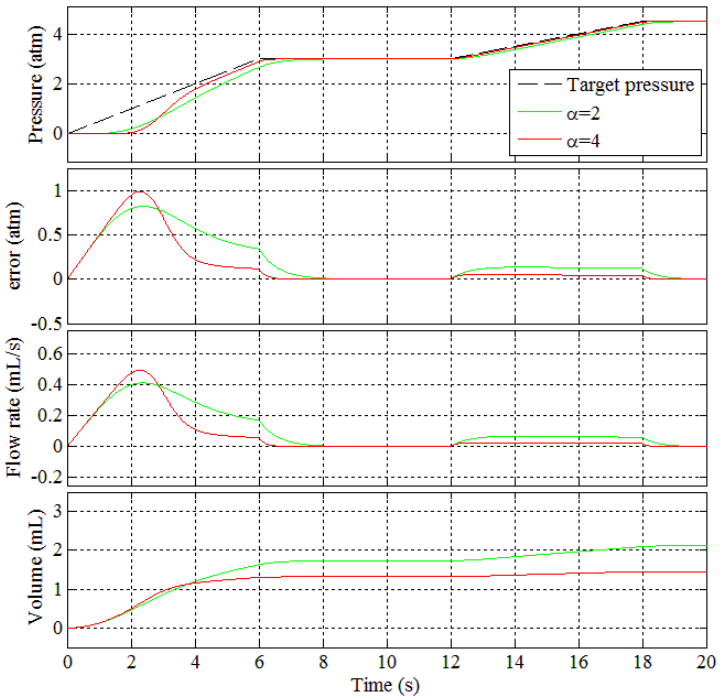

Figure 6.6. Proportional control for $\alpha = 2$ and $\alpha = 4$

6.2.2. Control based on online estimation of the compliance curve

The proportional controller may provide convergence to desired pressure values. However, the proportional gain needs to be optimized based on knowledge of the plant,

which could be patient specific and not available *a priori*. In this section, we propose a method to control the pressure based on online estimation of the plant.

In this method, similar to the proportional controller design, the flow rate is considered as the control signal. Let us denote the measured pressure and volume as P and V. In order to achieve the desired pressure, P_d, based on (6.9), assuming that F_{PV} is one-to-one, the desired volume, V_d, is obtained as:

$$V_d(t) = F_{PV}^{-1}(P_d(t)). \tag{6.10}$$

The desired flow rate, f_d, is then obtained as the derivative of the volume with respect to time:

$$f_d(t) = \frac{dF_{PV}^{-1}(P_d(t))}{dt}. \tag{6.11}$$

This flow rate provides the desired pressure. However, the function F_{PV} is not known. To resolve this problem, we propose estimation of the compliance, and consequently the flow rate, from a real-time extrapolation approach. In this method, initially a flow rate, f_0, is applied. For extrapolation, a minimum of n_0 pressure-volume samples are obtained with a sampling time T:

$$(P[0], V[0]),...,(P[n_0 - 1], V[n_0 - 1]), \tag{6.12}$$

where $P[n] = P(nT), V[n] = V(nT)$. Pressure control starts after the time sample $n_0 - 1$. The desired pressure for $n \geq n_0$ is $P_d[n]$. In order to achieve this desired pressure, the desired volume is:

$$V_d[n] = \hat{F}_{PV}^{-1}(P_d[n]). \tag{6.13}$$

where $\hat{F}_{PV}^{-1}$ is a sliding estimate of F_{PV}^{-1}. This estimate is obtained from extrapolation of n_0 previous samples and is updated in real-time. In order to achieve the volume in (6.13), the flow rate is modified from f_0 to:

$$f_d[n] = \frac{V_d[n] - V[n-1]}{T} = \frac{\hat{F}_{PV}^{-1}(P_d[n]) - V[n-1]}{T}. \tag{6.14}$$

For the steady-state volume, V_{ss}, we have:

$$V_{ss}[n-1] \cong \hat{F}_{PV}^{-1}(P_d[n-1]). \tag{6.15}$$

Hence using (6.14) and (6.15) we obtain the steady-state flow rate, f_{ss} :

$$f_{ss}[n] \cong \frac{\hat{F}_{PV}^{-1}(P_d[n]) - \hat{F}_{PV}^{-1}(P_d[n-1])}{T}, \tag{6.16}$$

which is a discrete approximation of the desired flow rate, f_d, in (6.11), indicating that the operating point on F_{PV} is moving along the desired pressure trajectory, P_d.

In order to simulate the performance of this control method, let us incorporate some experimental limitations. First, we define a saturation function as:

$$s(x) = \begin{cases} -a & x \le -a \\ x & -a < x < b \\ b & b \le x \end{cases} \tag{6.17}$$

where a and b are positive constants which determine saturation limits. We then apply limits on the flow rate and the rate of change of flow rate:

$$f_{sat}[n] = s_1\left(f_d[n-1] + s_2\left(f_d[n] - f_d[n-1]\right)\right), \tag{6.18}$$

where s_1 and s_2 are saturation functions corresponding to the limits (a_1, b_1) on the flow rate and (a_2, b_2) on the rate of change of flow rate, respectively. Therefore, the flow rate in the simulation is generated as:

$$f[n]=\begin{cases} f_0 & n \le n_0 \\ f_{sat}[n] & n > n_0 \end{cases} \tag{6.19}$$

Figure 6.7 demonstrates the simulation of this control method for the plant given by (6.9) when $\alpha = 2$. In this simulation, for the saturation functions we used $a_1 = b_1 = 5\,\text{mL/s}^2$ and $a_2 = b_2 = 1\,\text{mL/s}$. This figure presents the simulated pressure, convergence error, flow rate and volume. The desired pressure is depicted by a dashed line. In this simulation, a linear extrapolation was used. Therefore, in order to start the control method only two samples were required $(n_0 = 1)$. However, in order to graphically present the two phases of identification and control, pressure control was started at 2 s, marked by a circle. As Figure 6.7 shows, the pressure started tracking the desired trajectory once the control mechanism was switched on. This performance is superior to the one provided by the proportional controller in the previous section.

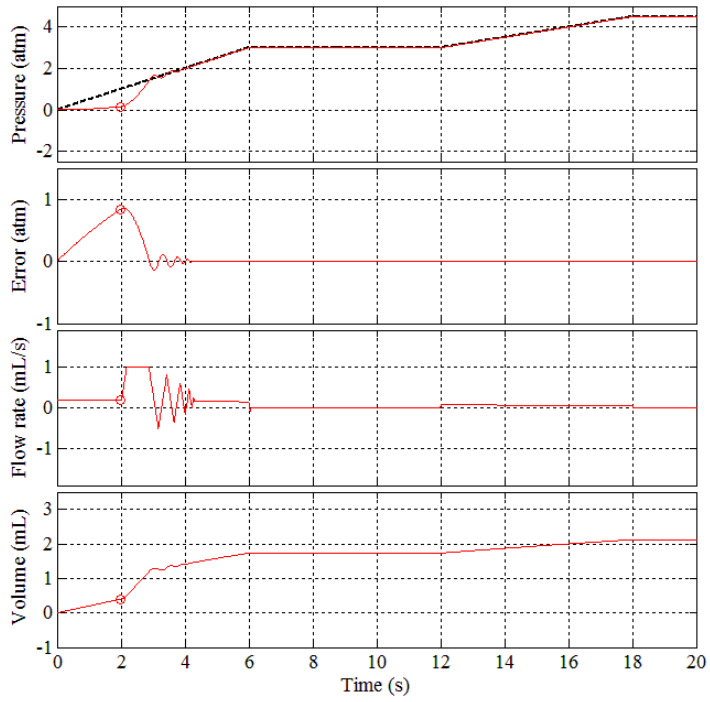

Figure 6.7. Pressure control based on online estimation of the compliance curve

6.3 Diameter control

In the previous sections, we discussed pressure control. In angioplasty, although pressure control can provide safer procedures, the determining factor to continue or stop balloon inflation is the luminal diameter of the artery. In this section, we discuss the control of the luminal diameter.

The proposed closed-loop control system is presented in Figure 6.8.

1) The actuator is a programmable syringe pump to deliver or withdraw liquid with flow rate f. The volume of liquid, V, is used to inflate or deflate the balloon.

2) The plant is composed of two components. The first component, F_{PV}, provides the pressure-volume relationship. The output of the first component is the pressure, P, which causes deformation of the artery. The second component F_{DP}, provides the pressure-diameter relationship. The output of the second component is the luminal diameter, D, of the deformed artery.

3) The sensing is composed of the two stages, namely, intravascular imaging and image analysis. In order to use the luminal diameter in a feedback loop, intravascular images are used. Image analysis techniques are applied to these images to estimate the diameter in real-time.

4) The controller is implemented in a PC. It calculates the flow rate, f, based on the error, e, between the desired diameter, D_d, and the measured diameter, D. The controller then sends the flow rate value as a command to the pump.

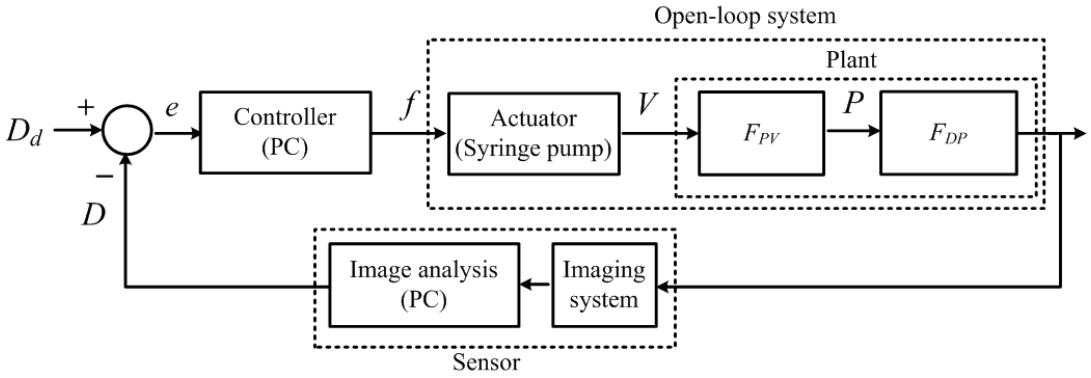

Figure 6.8. Inflation control based on diameter feedback

The experimental results to be provided in Chapters 11 and 12 correspond to the diameter control proposed in this section. Here, we present diameter control simulation results.

A state-space representation for the open-loop system can be obtained as:

$$\begin{cases} \dot{x}(t) = u(t) \\ y(t) = F_{DP}(F_{PV}(x(t))) \end{cases} \tag{6.20}$$

where t is the time variable, $x(t) = V(t),\ u(t) = f(t),$ and $y(t) = D(t).$

In the closed loop system, the objective is to achieve a desired output, $y_d = D_d.$ As will be shown in Chapter 11 and 12, the controller used in experiments was designed to generate a positive constant flow rate command to inflate the balloon when the actual diameter was smaller than the desired diameter and a negative constant flow rate command to deflate the balloon when the actual diameter was larger than the desired diameter. This function of the controller was provided by a sign function. In simulations to be presented here, in order to avoid fast switching caused by the sign function, we used a saturation function, $s,$ given by (6.17). The applied control law was, therefore, given by:

$$u = s(k_p.(y_d - y)) = s(k_p.(y_d - F_{DP}(F_{PV}(x)))), \tag{6.21}$$

where the term inside the saturation function is a proportional control with gain, $k_p,$ similar to the proportional pressure control method presented before.

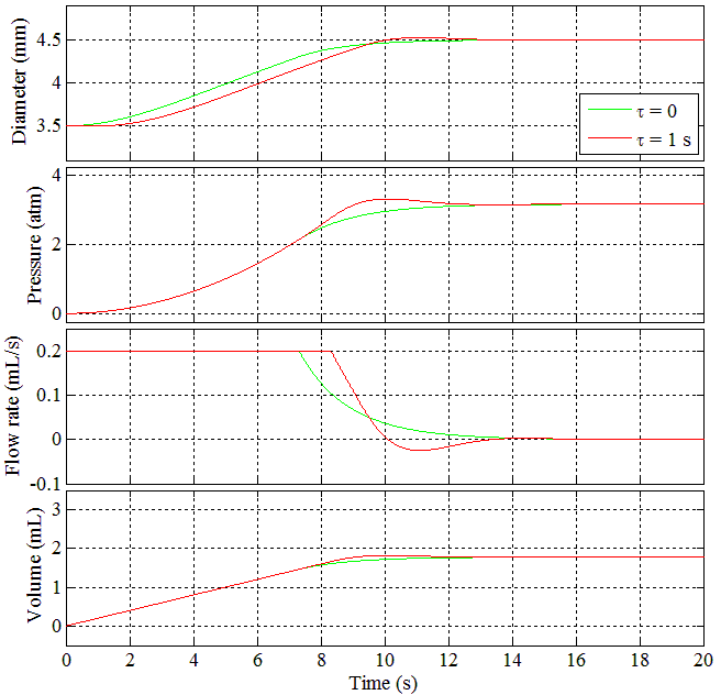

Figure 6.9. Diameter control with and without a time delay

In the experiments, the actual diameter was estimated by image analysis. In the simulations, it was calculated as the output of the function, $F_{DP}(F_{PV}(x))$. The function F_{PV} was generated by (6.9) with $\alpha = 2$. The function $F_{DP}(P)$ was generated in such a way to provide values relevant to the experimental data:

$$F_{DP}(P) = D_0 + 0.7\ln(P+1). \tag{6.22}$$

where D_0 is the initial luminal diameter. Both of these functions provided values in a range relevant to the experimental results. Since the balloon in the setup of Figure 6.1 is the most distal component, there could be a delay between the time that pressurization is started by the syringe and the time that the balloon starts to increase the luminal diameter. We simulated this as a time delay, τ in one of the simulation scenarios.

Figure 6.9 demonstrates the results of the diameter control simulation for two scenarios with and without a time delay for $k_p = 1$ mL(atm·s)$^{-1}$. In this figure, simulated diameter,

pressure, flow rate, and volume are presented. In the simulation, the initial diameter was 3.5 mm and the target diameter was 4.5 mm. Using the saturation function, the flow rate was limited to 0.2 mL/s. As Figure 6.9 confirms, in both scenarios, the diameter converged to the desired value. In the scenario, where there was a time delay of 1 s, the controller also responded to diameter variations with a delay. This resulted in a diameter overshoot beyond the desired value, as observed in Figure 6.9.

6.4 Pressure and diameter control

In the previous sections, we presented methods to control the pressure or the diameter during the balloon inflation. In this section, we combine the previous methods and propose a cascade control strategy, presented in Figure 6.10. In this control system, Controller 1 in the inner loop corresponds to pressure and Controller 2 in the outer loop corresponds to diameter. In this system, it is not possible to control both pressure and diameter simultaneously to desired values as the diameter is dependent on the pressure. However, this structure provides the possibility of achieving a desired diameter with desired specifications on pressure, e.g., rate of pressurization.

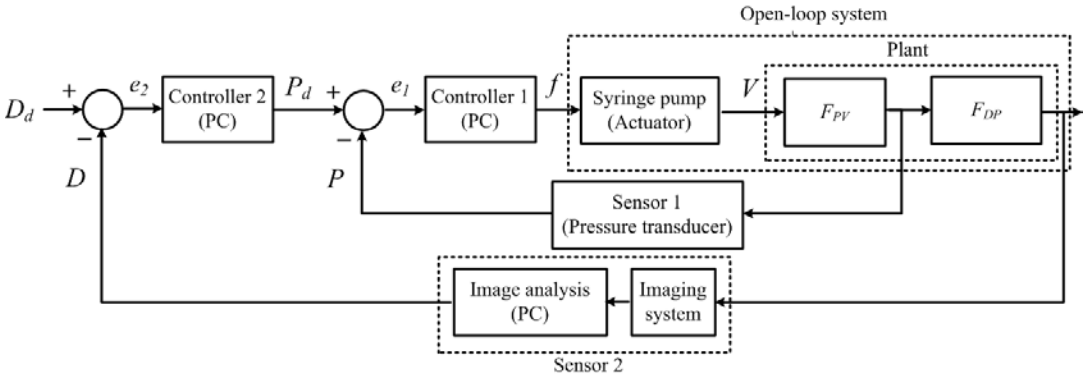

Figure 6.10. Inflation control based on pressure and diameter feedback

A state-space representation for the open-loop system can be obtained as:

$$\begin{cases} \dot{x}(t) = u_1(t) \\ y(t) = \begin{bmatrix} y_1(t) \\ y_2(t) \end{bmatrix} = \begin{bmatrix} F_{PV}(x(t)) \\ F_{DP}(F_{PV}(x(t))) \end{bmatrix} \end{cases} \tag{6.23}$$

where t is the time variable, $x(t) = V(t), u_1(t) = f(t),$ and $y(t) = \begin{bmatrix} P(t) & D(t) \end{bmatrix}^T$.

In the closed-loop system, the objective is to achieve the desired pressure, $y_{d_1} = P_d$, and the desired diameter $y_{d_2} = D_d$. We provide an example of the cascade control, based on previously discussed pressure control and diameter control. The goal is to achieve a desired diameter value with a desired limit on the pressurization rate. In angioplasty, limiting the pressurization rate may provide a safer procedure and reduce arterial injury. The Controller 1 is a proportional controller with gain, k_{p_1}, similar to the one in (6.8). The control law, u_1, generated by this controller is defined as:

$$u_1 = k_{p_1}(y_{d_1} - y_1) = k_{p_1}(y_{d_1} - F_{PV}(x)). \tag{6.24}$$

The desired pressure trajectory which is provided to the inner loop is determined by the control law, $u_2 = P_d$, generated by Controller 2. In addition, this control law determines the direction of the syringe plunger movement to inflate or deflate the balloon to achieve the desired diameter. This control law is defined as the integral of the diameter control term (6.21) with gain k_{p_2} :

$$u_2 = \int_0^t s(k_{p_2}.(y_{d_2}(\lambda) - y_2(\lambda)))\, d\lambda = \int_0^t s(k_{p_2}.(y_{d_2}(\lambda) - F_{DP}(F_{PV}(x(\lambda)))))\, d\lambda, \tag{6.25}$$

where the upper and lower limits, (a, b) of the saturation function, s, defined in (6.17), determine the maximum rate for inflation and deflation in the desired pressure trajectory. When the proportional control term exceeds the saturation limits, a ramp control signal is

generated after integration. The ramp slope, $-a$ corresponds to maximum deflation rate and the ramp slope, b, corresponds to maximum inflation rate. As the deflation rate does not pose any risk in angioplasty, the limit, $-a$ can be relaxed.

Figure 6.11 demonstrates the results of simulations for two values of $b = 0.25$ atm/s, and $b = 0.50$ atm/s. In both cases, no lower limit was defined in the saturation function. In these simulations we used $k_{p_1} = 3$ mL(atm·s)$^{-1}$ and $k_{p_2} = 5$ atm/mm. In Figure 6.11, simulated diameter, pressure, flow rate, and volume are shown. The initial diameter was 3.5 mm and the target diameter was 4.5 mm. In both scenarios, the target diameter was achieved successfully, however, with different speeds. In the pressure graph, the desired pressure trajectory, $u_2 = P_d$, generated by the Controller 2 in each scenario, is depicted by a dashed line. This figure confirms how introducing the ramp slopes of 0.25 atm/s and 0.50 atm/s in the desired pressure trajectory can provide a desired limit on the pressurization rate to achieve the target diameter.

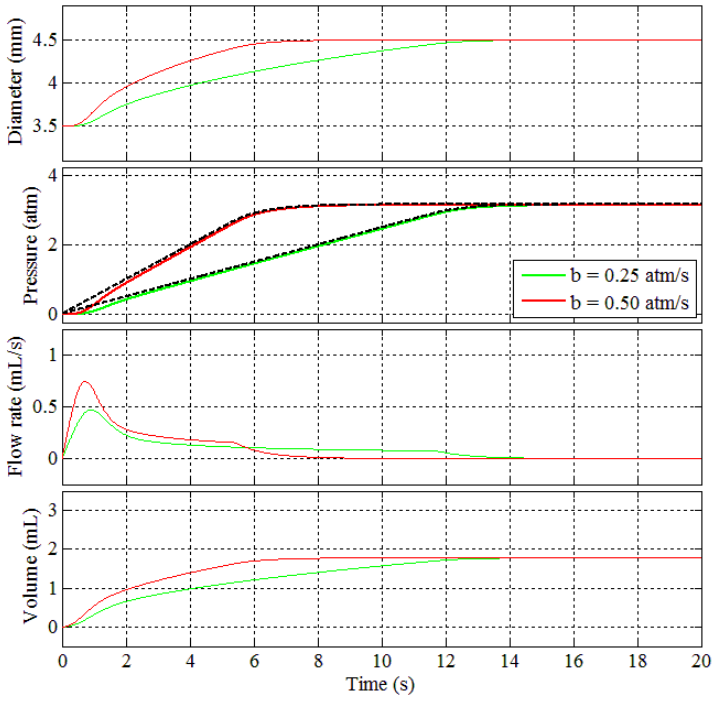

Figure 6.11. Diameter control with different pressurization rates

Figure 6.12 demonstrates the results of simulation for two scenarios with and without a time delay for $k_{p_1} = 3$ mL(atm·s)$^{-1}$ $k_{p_2} = 5$ atm/mm and $b = 0.50$ atm/s. No lower limit was defined in the saturation function. In Figure 6.12, simulated diameter, pressure, flow rate, and volume are presented. The initial diameter was 3.5 mm and the target diameter was 4.5 mm. In both scenarios, the diameter converged to the desired value. As the diameter graph in Figure 6.12 confirms, in the scenario with a time delay of 1 s, the delay in controller response resulted in a diameter overshoot beyond the desired value.

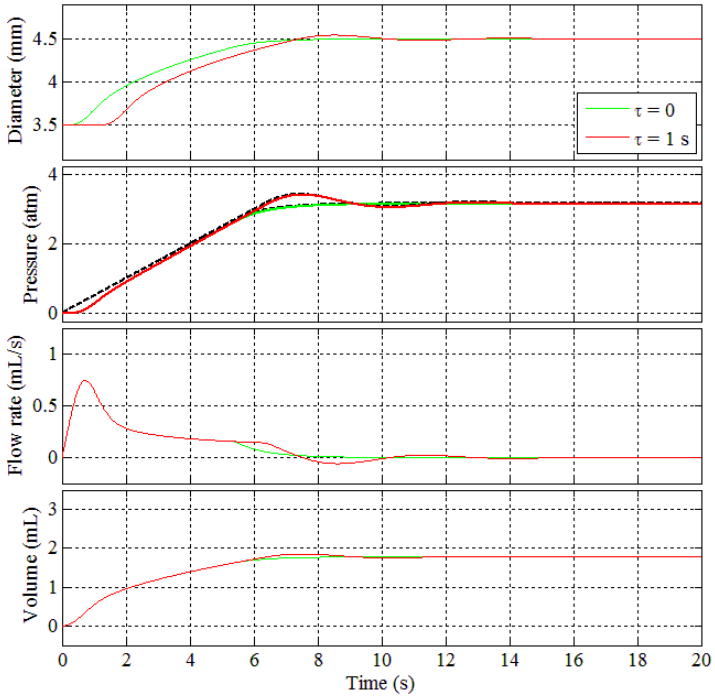

Figure 6.12. Diameter control with a desired pressurization rate with and without a time delay

6.5 Concluding remarks

In this chapter, we formulated balloon inflation as a conventional control problem and provided simulation results for various scenarios. The aim was to introduce some ideas and concepts to apply control methodologies to angioplasty. Using these concepts, more complex methods could be developed. Experimental relevance of these methods should be rigorously investigated. Experimental implementation is generally a challenging task,

in particular for validation of the diameter control method as it requires real-time image analysis in a feedback loop. In Chapters 11 and 12, we provide experimental validation of the proposed diameter control method in Section 6.3. Initially, this required development of an integrated imaging balloon catheter. In the next chapter, we present monitoring and characterization of balloon deformation using IVOCT. The results in subsequent chapters were obtained using the developed imaging balloon catheter.

CHAPTER 7: IVOCT MONITORING AND CHARACTERIZATION OF BALLOON DEFORMATION IN A DEPLOYMENT TESTER

In this chapter, we propose a novel application of the IVOCT technology, i.e., the monitoring of balloon inflation in a balloon deployment tester. A deployment tester is used to test the quality of balloons through inflation under predetermined conditions. Traditionally, it can be equipped with a laser scanner that is used externally to provide measurements of the balloon's outer diameter at a given location. Such assessment, unfortunately, is limited to a side view and a particular angle. Figure 7.1 illustrates such a technique to monitor balloon inflation in a heated water bath.

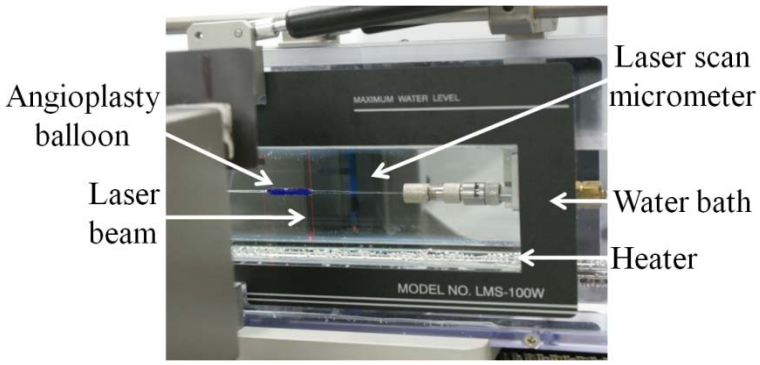

Figure 7.1. Balloon inflation monitoring using a laser scanner

Combining IVOCT with a deployment tester allows a full characterization of balloon diameter and wall thickness during the inflation process. Measurements are not limited to a single location but with a quick pullback the whole balloon can be imaged at a given pressure. Combining the computerized balloon inflation provided by the deployment tester with the accurate measurements of IVOCT results in a tool that can benefit many applications. For balloon development alone, one can validate balloon performance,

explore new designs, validate balloon deformation models, or extract mechanical properties. The system can be used with a phantom or an excised artery to provide further applications. Therefore, this provides not only a method to follow balloon inflation with realistic conditions, but also a setup to simulate angioplasty procedures with IVOCT monitoring.

In this chapter, we first present the method that was used to fabricate the balloon, the structure of our optical coherence tomography imaging balloon (OCTIB) catheter and the integration of the OCTIB catheter in the deployment tester. We then present and discuss the results of balloon deformation monitoring. Subsequently, we present the applied image analysis techniques and the resulting characterization of balloon deformation. At the end, we provide the concluding remarks.

7.1 Balloon production

Since semi-compliant balloons are applied in angioplasty, a semi-compliant balloon was used to perform this first investigation of the combination of IVOCT with a balloon deployment apparatus. The balloon fabrication process [87] is generally composed of three main phases, i.e., extrusion, double-end stretching and balloon forming. In the first phase, the aim is to extrude tubing with high concentricity and uniform wall thickness. An extruded polyurethane tube (Pellethane, 55D, Dunn Industries, Inc.) was used for balloon production. In the customary second phase, i.e., the double-end stretching, both ends of the tube are stretched under high temperature, leaving in the middle an unstretched segment, called parison. The polyurethane, used in this work, is more elastic than other balloon production materials, e.g., Pebax. A long stretch would cause the material to shrink back to its original length. Therefore, this second-phase was skipped and no

double-end stretching was performed. In the third phase, the balloon forming is executed through a blow molding process by a balloon-forming machine (9810H, Interface Catheter Solutions), illustrated in Figure 7.2. In blow molding, the operator places the proximal end of the tube into the chuck on the left side, which is connected to a supply of compressed nitrogen. The distal end goes through the centre mold and the distal-end plugs. Compressed nitrogen is blown through the proximal end at a low pressure, while the heater jaws warm up the piece. Different stages of the balloon forming process are demonstrated in Figure 7.3. During the primary heating stage, the pressure and temperature are raised, followed by axial pre-stretching of both ends. The process then enters the primary stretch phase, where both ends are further stretched at a predetermined speed to a specified length. This causes the tube to be extended inside the mold and expanded due to pressure, which leads to formation of the balloon. A secondary stretch is applied to form the cones of the balloon on both sides. At the end of the process the mold is cooled down, the pressure is released and the balloon is ready to be removed from the mold.

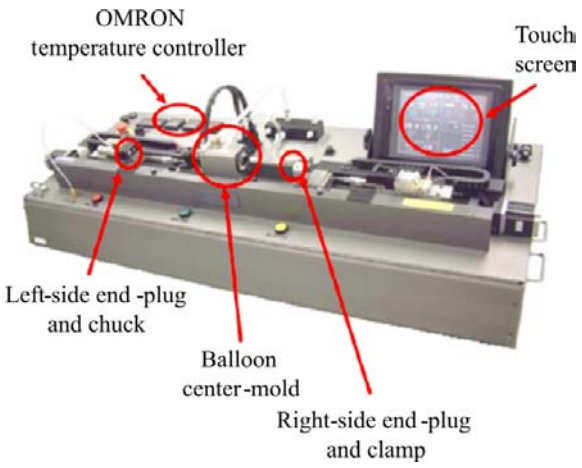

Figure 7.2. The balloon forming machine (9810-H, Interface Catheter Solutions)

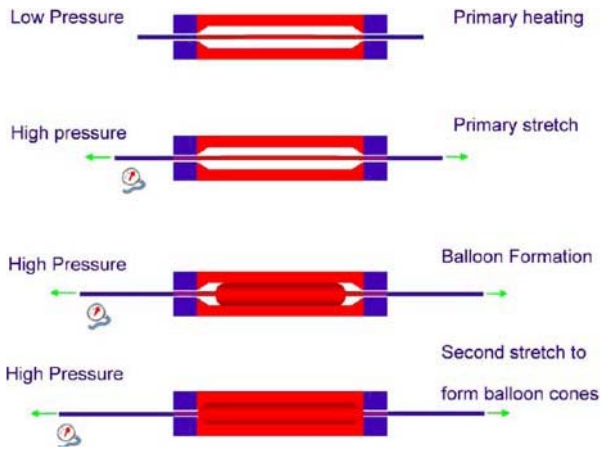

Figure 7.3. Balloon forming stages

Table 7.1 presents the values of parameters that were used for different stages of the balloon forming process. The machine advances from each stage to the next, once a user-defined terminating condition on temperature, pressure, etc. is satisfied. The choice of these conditions and the applied stretch, pressure and temperature, affect the balloon quality, e.g., wall thickness, mechanical properties and burst pressure.

The balloon forming process produced a semi-compliant balloon with dimensions of 4 mm x 15 mm, with an inner diameter of 1.2 mm and an outer diameter of 1.50 mm in the balloon tubing.

Table 7.1. Balloon forming parameters

	Primary heating	Primary stretch and balloon formation	Secondary stretch
Mold temperature target (°C)	90	170	175
Pressure (atm)	5	30	20
Stretch (mm)	30	35	38
Terminating condition	Temperature >80°C	After 4 seconds	Temperature >150°C

7.2 Structure of the OCTIB catheter

The OCT system, described in Chapter 3, was applied in experiments. Figure 7.4(a) schematically demonstrates the composition of the OCTIB catheter. The IVOCT probe was described in detail in Section 3.2.2. In the OCTIB catheter, a polymer sheath (PS) was used to protect the IVOCT probe and to prevent it from drifting away from the center

of the balloon while rotating. The diameter of the polymer sheath needed to be close to the diameter of the probe in order to facilitate inclusion of the IVOCT assembly inside the balloon. On the other hand, it needed to provide sufficient space to allow the probe to be easily rotated with minimal friction. A heat-shrinkable Teflon tube (FEP, Zeus, Inc.) was chosen to achieve the desired characteristics. Teflon was a suitable material for this application, since it is translucent and causes low friction. After shrinking, approximate inner and outer diameters of 0.9 mm and 1.0 mm were respectively obtained for the Teflon tube. The probe and its polymer sheath were inserted into the balloon (B), as shown in Figure 7.4(a).

Figure 7.4(b) presents a photo of the OCTIB catheter. Although imaging was performed with infrared light, red light was included in the system to locate the measurement region visually. Red light departing the IVOCT probe is clearly visible in Figure 7.4(b).

Figure 7.5 provides a cross-sectional view for the proximal tube of the OCTIB catheter. As shown in this figure, the polymer sheath divided the lumen of the balloon catheter into two isolated lumens. The lumen between the polymer sheath and the balloon was allocated to high-pressure liquid, used for deployment of the balloon. Within the polymer sheath, a low-pressure lumen contained the rotating IVOCT probe. In our design, it was essential to isolate the two lumens; if the high pressure water was allowed inside the polymer sheath, it would be necessary to entrap it with a tight sealing at the proximal end. This could restrict or hamper the probe motion. The two-lumen approach revealed to be an efficient solution. In the next section, we describe how both lumens were connected to their respective low-pressure and high-pressure lines.

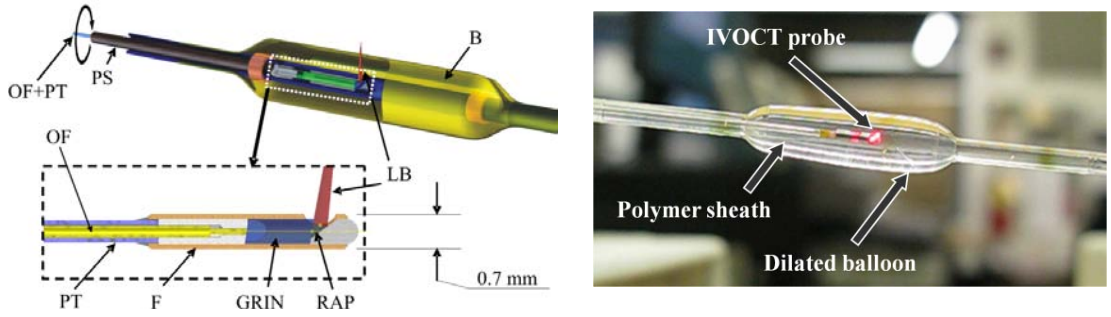

(a) (b)

Figure 7.4. Schematic (a) (B: Balloon, F: ferrule, PS: polymer sheath, GRIN: gradient-index lens, LB: light beam, OF: optical fiber, PT: polymer tube, RAP: right-angle prism) and illustration of the OCTIB catheter (b)

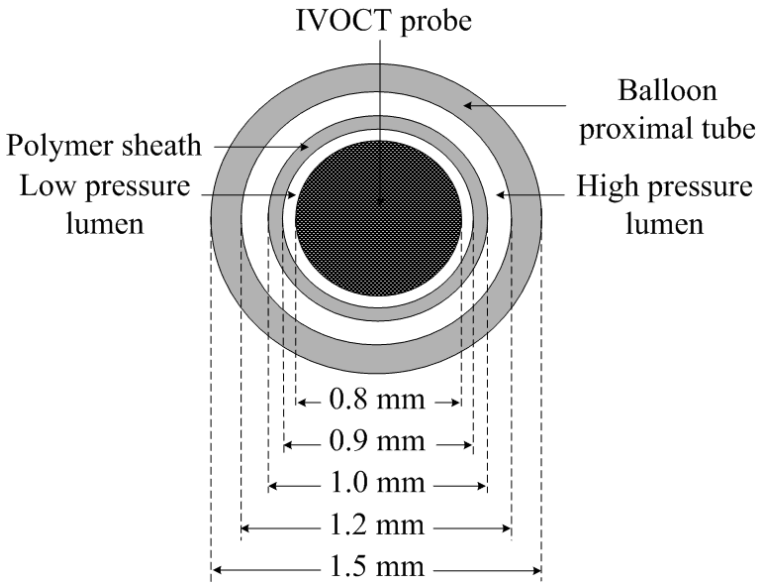

Figure 7.5. Cross-section of the OCTIB catheter (proximal side)

7.3 Integration of the OCTIB catheter in a deployment tester

Angioplasty is usually performed using a manual inflation device monitored by a pressure gauge. However, in order to quantify, record, and analyze the measurements, we used a computerized deployment setup which was based on a hydraulic pressure tester (Interface Catheter Solutions, model PT-3070). Figure 7.6 provides a schematic and illustrations of the experimental setup, used to deploy the balloon. This setup allowed for programming customized inflation and deflation cycles with desired pressures. In the experiments, demineralized water was used as the pressurization medium. The IVOCT probe and the

polymer sheath were introduced into the balloon catheter through a T-connector as shown in Figure 7.6. This connector also provided a connection between the deployment tester and the high-pressure lumen, delimited by the polymer sheath and the balloon catheter.

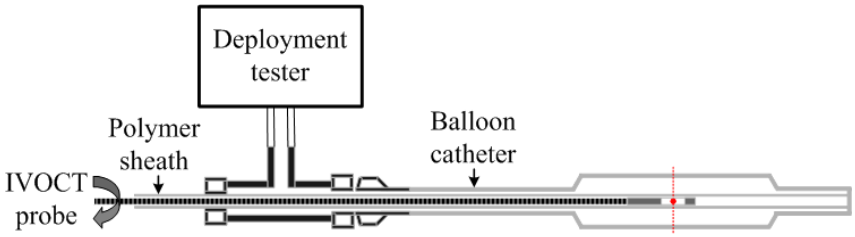

(a)

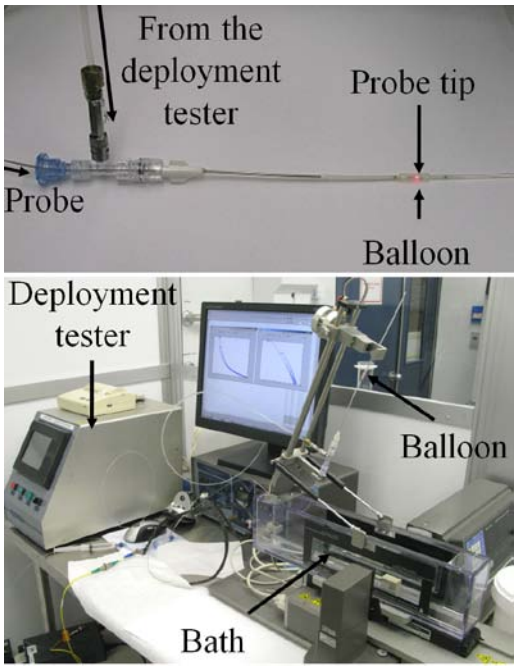

(b)

Figure 7.6. Schematic (a) and illustration of OCTIB catheter in the deployment tester

7.4 IVOCT monitoring of balloon deformation

IVOCT provided gray scale images of the balloon during inflation. Each image was originally stored in polar coordinates where the horizontal and the vertical axes corresponded to the probe rotation angle and the radial depth, respectively. Figure 7.7(a) demonstrates an image of the inflated balloon in polar coordinates. The image was provided by a matrix whose elements represented the values of intensity at various pixels.

The IVOCT image in Figure 7.7(a) is displayed on a logarithmic scale. To provide a better distinction between various regions, the dark and bright regions were reversed. In Figure 7.7(a), the values on the primary image axes (bottom and left) represent the pixel values. The values on the secondary (top and right) axes represent the angle in degrees and the depth in millimeters in optical distance, i.e. the product of the geometrical distance and the refractive index.

Figure 7.7(b) demonstrates the IVOCT image of the inflated balloon in Cartesian coordinates, which was obtained from the image in polar coordinates using a polar-to-Cartesian transformation.

In Figure 7.7(a,b), the polymer sheath (PS) and the balloon (B) are represented each by two contours, corresponding to their inner and outer surfaces. Inner and outer surfaces of the balloon, B_I and B_O, are identified. The innermost contour represents the prism surface (R). The prism surface is represented by R as it is used as a reference for image registration, as will be explained later. The radial pixel size in our images was 8 μm in optical distance. Each column in the image matrix represents depth scanning at a particular angle and is called an A-scan. In our balloon inflation monitoring experiment, imaging was performed at a rate of 20 FPS. Since the sweep rate of our source was 30 kHz, each frame included 1500 A-scans, providing an angular resolution of about 0.2°. In Figure 7.7(a,b), a sample A-scan is depicted by a red line. This A-scan is presented in Figure 7.7(c). On the A-scan the surfaces, corresponding to the balloon, polymer sheath and the prism, appear as spikes.

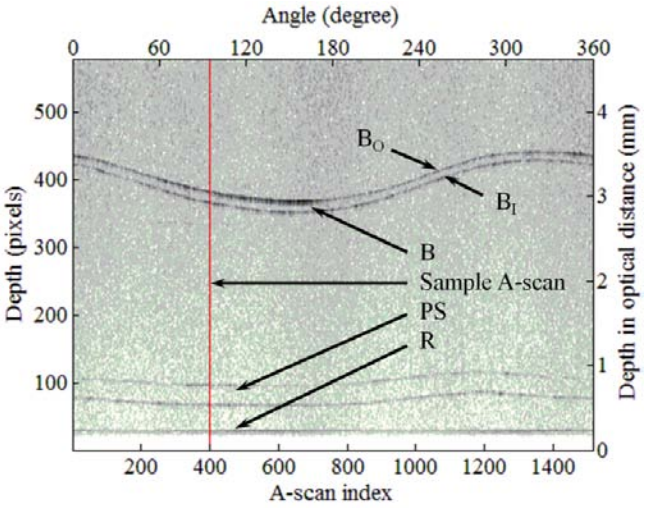

(a)

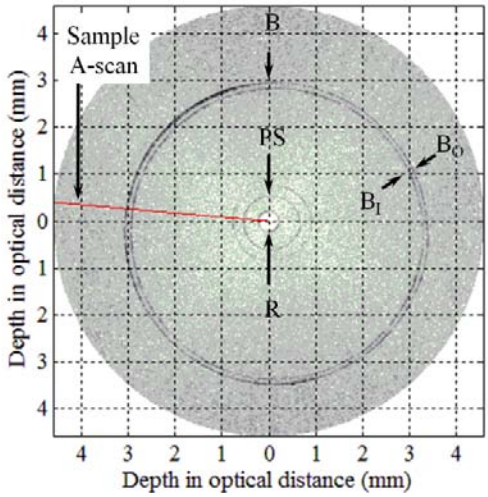

(b)

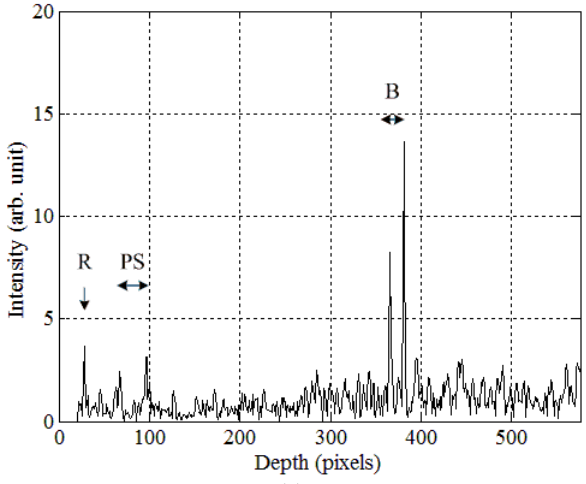

(c)

Figure 7.7. IVOCT image of the balloon in polar (a) and Cartesian (b) coordinates and an A-scan profile (c)

Figure 7.7 presents imaging of the balloon at a particular pressure. Images acquired during balloon inflation could be used to generate a movie clip. A movie clip presenting balloon inflation monitoring results is available in [1].

A pullback of the probe makes it possible to carry out a volumetric assessment of the balloon at different pressures and check the homogeneity of the balloon deformation along the longitudinal axis. Combination of the obtained tomographic images can provide a three-dimensional view of the balloon. A 3D view was generated using commercial software (ORS Visual, Object Research Systems) which is presented in Figure 7.8. The 3D view is composed of 200 cross-sectional images. These images were acquired during a motorized pullback at a speed of 2.5 mm/s at an inflation pressure of 4 atm, giving a 125 μm step between two successive cross-sectional images. The pullback started in the tube distal to the balloon and stopped in the tube proximal to the balloon.

The monitoring results, described in this section, provide a qualitative demonstration of the new opportunities provided by the combination of IVOCT with a balloon deployment tester.

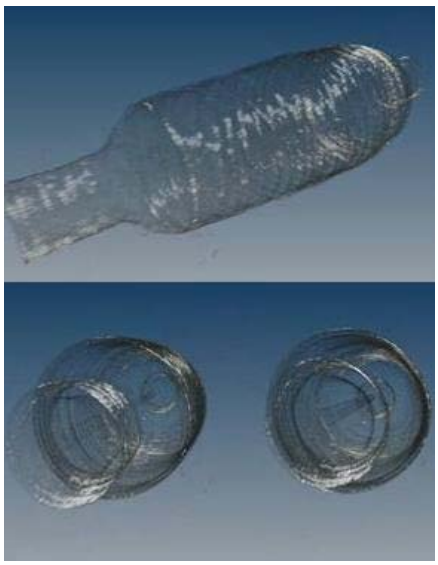

Figure 7.8. 3D rendering of the balloon, obtained from a pullback at a pressure of 4 atm

7.5 Image analysis

In order to extract balloon diameter and thickness values, contours corresponding to balloons surfaces were detected in IVOCT images. All algorithms were applied to image matrices in polar coordinates, denoted by $I_{X\times Y}$ where X is the maximum depth in the image in pixels and Y is the number of A-scans. In the notation $I(i,j)$, i represents the row number or depth in pixels and j represents the column number or the A-scan index. Since the column number corresponds in fact to an angular value, in our notations periodic boundary conditions are used, so the first and last A-scans are adjacent A-scans.

In the following, we describe our image registration method as a first step. Then we present our ridge detection and sequential algorithms to detect contours. Finally, we describe how pixel values of the detected contour nodes are converted to values in geometrical distance.

7.5.1. Image registration

Images were registered in the radial direction to eliminate the variability of imaging depth. All images were registered by adjusting the depth with respect to a reference. The prism surface (R) was considered as the reference, as its distance from the center of rotation was known. In IVOCT images, the prism surface was distinguished as a contour, at an almost constant depth on various A-scans. Therefore, a constant depth value was estimated in each image. The prism surface appeared as spikes on A-scans. Therefore, it was detected by a peak detection technique. As the goal was to obtain one constant value for all A-scans, the peak detection was performed after averaging all A-scan profiles. The peak was detected in a search interval, S_R, which was experimentally defined. The detection algorithm was formulated as:

$$i_R = \arg\max_{i \in S_R} \left\{ \frac{1}{Y} \sum_{n=1}^{Y} I(i, j+n) \right\}, \tag{7.1}$$

where i_R was obtained as the depth of the prism surface in pixels (in our algorithm, $S_R = [1, 50]$). Using this value, the image, *I*, was either cropped in radial direction or padded with rows of zeros to position the prism surface at the correct pixel location, providing the correct distance from the center of rotation.

7.5.2. Ridge detection

In order to characterize balloon deformation, the contours, $\mathrm{B_I}$, and $\mathrm{B_O}$, as identified in Figure 7.7, were detected. One node per A-scan was detected for each contour. These contours can be distinguished by spikes (local maxima) on most A-scans. Therefore, they were detected as ridges. Let j (where $j \in [1, Y]$) denote the A-scan index. A search interval, S_j, was obtained on each A-scan, as explained later in our sequential algorithm, to isolate the contour of interest from other contours. Then, by finding the maximum of a moving average we detected the contour node on S_j. The moving average was applied across A-scans to increase the robustness of the algorithm when the contour spike was absent on the corresponding A-scan. The node detection algorithm was formulated as:

$$i_j = \arg\max_{i \in S_j} \left\{ \frac{1}{2w+1} \sum_{n=-w}^{w} I(i, j+n) \right\}, \tag{7.2}$$

where w is the size of the averaging window and i_j is obtained as the depth of the detected node on A-scan j (in the applied algorithm, $w = 5$). This method is equivalent to the one described in Section 4.2.2 based on the rotating kernel transformation, using only

a horizontal line kernel. The horizontal line kernel provided sufficiently accurate results as the contours did not demonstrate sharp variations across A-scans.

7.5.3. Sequential algorithm for contour detection

The contour nodes, i_j, and the search intervals, S_j, were obtained sequentially from one A-scan to the neighbouring A-scan. Therefore, for each contour, detection of the first node on the first A-scan was the key to detection of the subsequent nodes on the subsequent A-scans. Next, we describe how the first node was detected for each contour.

The first node was detected on an arbitrarily selected A-scan. Let j_0 denote the column number in *I*, representing the selected A-scan. First, a pixel at a depth i_B, was detected between the two contours, B_1, and B_O, on A-scan j_0. This pixel was used to define the search intervals to detect the first node of each contour. We exploited the vicinity of the two ridges corresponding to the balloon's inner and outer surfaces. A template filter, F, was generated based on the estimated balloon thickness, given by:

$$F(i.j)=\begin{cases}-1 & -\dfrac{T-1}{2}\le i\le\dfrac{T-1}{2}\\ 1 & \text{otherwise}\end{cases}\qquad i\in[-\alpha,\alpha], j\in[-\beta,\beta], \tag{7.3}$$

where α,β are positive integers, which determine the size of the template, and T is a parameter corresponding to the minimum thickness of the balloon in pixels (in the applied algorithm, $T=11$, $\alpha=10$, and $\beta=5$). Then i_B was obtained as the pixel maximizing the cross-correlation with the template:

$$i_B=\arg\max_i\sum_{n=j_0-\beta}^{j_0+\beta}\sum_{m=i-\alpha}^{i+\alpha}I(m,n)F(m-i,n-j_0). \tag{7.4}$$

The contour, B_I, was on the inner side of the detected pixel. Therefore, we defined a search interval,

$$S_{j0} = [i_B, i_B - 2\alpha], \tag{7.5}$$

on A-scan j_0 and applied (7.2) to find the depth of the first node for B_I.

The second node was detected on the neighbouring A-scan with index $j = j_0 + 1$. First, a search interval was defined around the depth of the previously detected node, given by:

$$S_j = [i_{j-1} - z,\ i_{j-1} + z], \tag{7.6}$$

where z determined the size of the search interval (in the applied algorithm, $z = 3$). Then, we applied (7.2) to detect the second node on the second A-scan. The process of finding the search interval using (7.6) and detecting nodes using (7.2) was continued sequentially on the subsequent neighbouring A-scans until one node was detected per A-scan.

To detect the contour, B_O, we defined a search interval,

$$S_{j0} = [i_B, i_B + 2\alpha], \tag{7.7}$$

on A-scan j_0 and applied (7.2) to find the depth of the first node. The rest of the nodes were obtained using a sequential algorithm, similar to the detection of B_I nodes.

7.5.4. Conversion from pixel values to values in geometrical distance

Image analysis algorithms provided contour nodes in pixel values. Pixel values were converted to depth values in millimeters in geometrical distance. Next, we provide a general formulation of this conversion which is also used in later discussions. Let us assume that in order for the light to reach a surface of interest, it needs to cross l media with refractive indices, $n_1, n_2, ..., n_l$. Let us also assume that the l contours corresponding

to the surface of interest and the interfaces between these media have been detected. If we denote the depth (in pixels) of the detected node for the *k*th contour on A-scan j as i_j^k the true geometrical distance, r_j^l, for the node on the surface of interest is obtained by:

$$r_j^l = r_R + s_{axial} \cdot \left(\frac{i_j^1 - i_R}{n_1} + \frac{i_j^2 - i_j^1}{n_2} + \ldots + \frac{i_j^l - i_j^{l-1}}{n_k} \right), \tag{7.8}$$

where r_R is the distance of the prism surface from the center of rotation in millimeters in geometrical distance and S_{axial} is the step size corresponding to each pixel in radial direction in optical distance.

In our conversions, $r_R = 0.15$ mm and $S_{axial} = 8\,\mu$m were used. In order to obtain the depth of the nodes corresponding to B_I, and B_O, refractive indices of 1.33 and 1.50 were used for water and polyurethane (balloon), respectively.

7.6 IVOCT characterization of the balloon deformation

In this section, we present a more quantitative assessment of balloon inflation, which was achieved by image analysis techniques. Figure 7.9 presents cross-sectional images of the balloon at pressures (*P*) of 2, 3 and 4 atm. Each IVOCT image (Figure 7.9(a-c)) is coupled with a deformation profile (Figure 7.9(d-f)), which provides a detailed analysis of balloon diameter and thickness at different angles. The magenta circle in Figure 7.9(a-c) represents the detected prism surface. As Figure 7.9(a-c) shows, the under-deployed segments are closer to the center of the balloon and generally have a larger wall-thickness. In Figure 7.9(d-f), these segments are depicted in blue. The over-deployed segments, on the other hand, are farther from the center and generally possess a smaller

wall thickness. These segments are depicted in red. The thickness values represented next to the color map in Figure 7.9(d-f) represent values in micrometers.

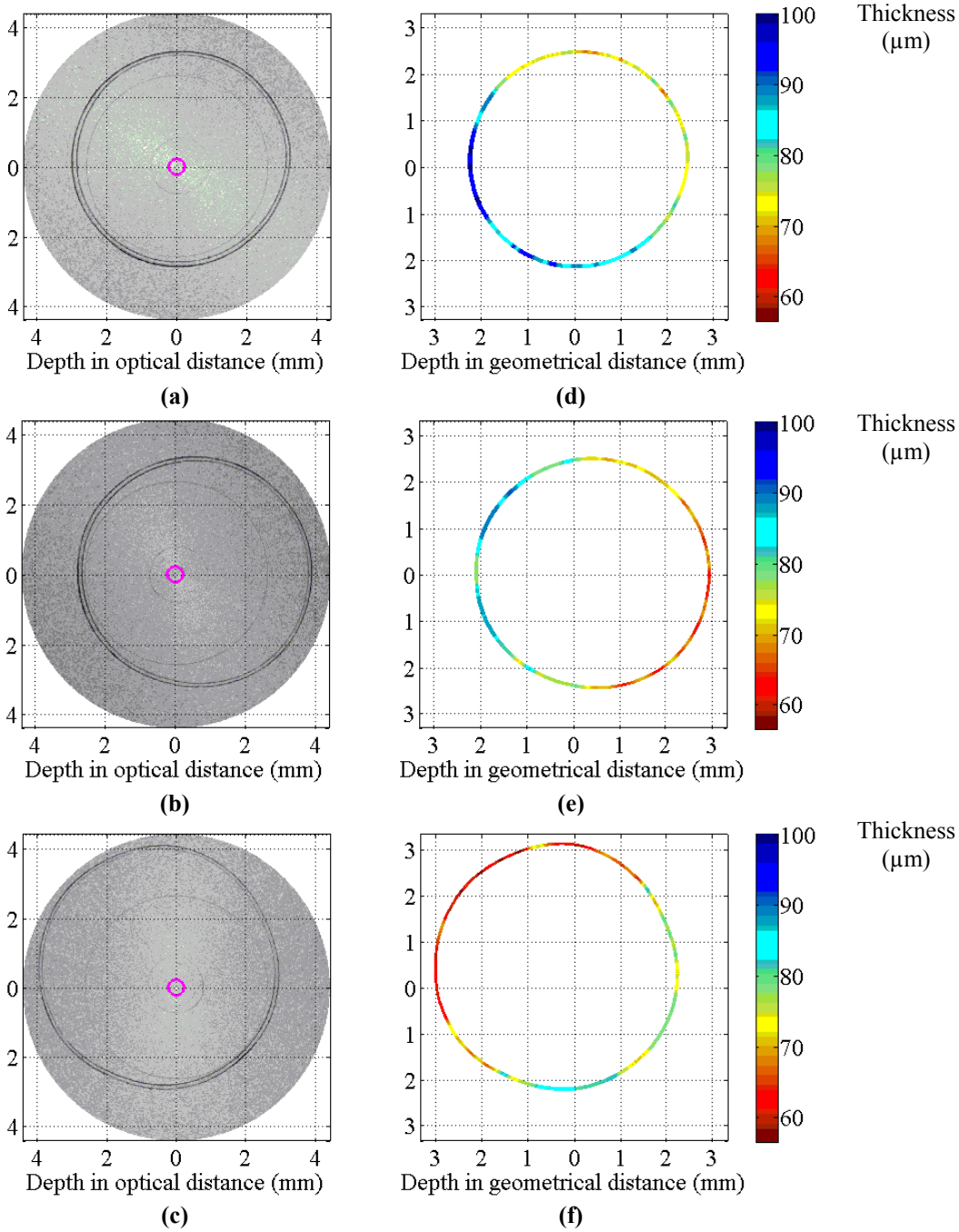

Figure 7.9. IVOCT images of the balloon at pressures of 2 atm (a), 3 atm (b) and 4 atm (c) and the corresponding balloon deformation profiles (d-f) with thickness color maps in µm

An overall assessment of the balloon diameter and thickness at different pressures is presented in Figure 7.10. As shown in Figure 7.10(a), the average of the diameter ($\overline{D}$) over different angles increased from 4.2 mm at a pressure of 0 atm to 5.3 mm at a pressure of 4 atm. Figure 7.10(a) also depicts the ratio of the standard deviation of the diameter (σ_D) to its average ($\overline{D}$), which can be helpful in characterizing deployment symmetry. This ratio increased as pressure was increased from 1 atm to 4 atm. This is consistent with the fact that the balloon was deployed more asymmetrically at larger pressures (Figure 7.9(f)). The ratio decreased as the pressure was increased from 0 atm to 1 atm. The reason is that at a pressure of 0 atm, the balloon was not fully deployed to a round shape. Therefore, at a pressure of 0 atm, the diameter variation at different angles was larger than the diameter variation at a pressure of 1 atm.

As demonstrated in Figure 7.10(b), the average thickness of the wall ($\overline{T}$) over different angles decreased from 91.5 μm to 71.7 μm as pressure was increased from 0 atm to 4 atm. The ratio of the standard deviation of the wall thickness (σ_T) to its average ($\overline{T}$), determines the extent to which uniform wall thickness is preserved at different pressures (Figure 7.10(b)). The higher the slope of this ratio with respect to pressure, the faster the balloon approaches its burst pressure. Figure 7.10(b) reveals that the wall thickness became less uniform when pressure was increased from 0 atm to 3 atm, a trend that seemed to stop when the pressure was further increased from 3 atm to 4 atm.

Next, we present a characterization of compliance for the balloon. As defined in (6.1), the compliance is the variation of the volume with respect to the internal pressure. Let us assume that the cross-sectional area of the balloon does not vary significantly in the axial

direction. By measuring variation of cross-sectional area with respect to pressure, a normalized-over-the-length value is obtained for the compliance.

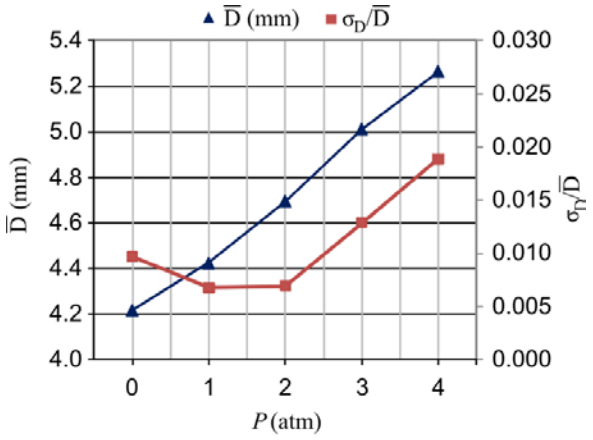

(a)

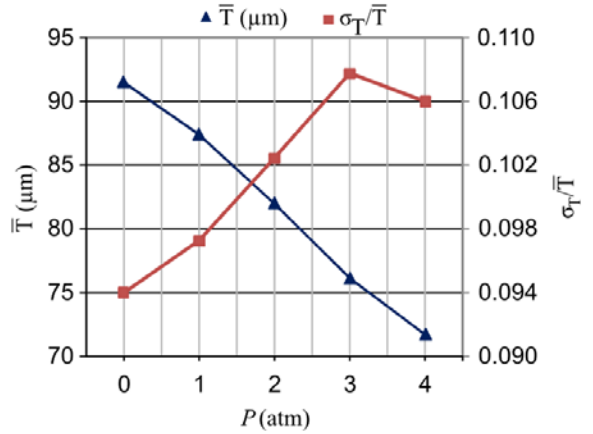

(b)

Figure 7.10. IVOCT characterization of balloon diameter (a), and wall thickness (b)

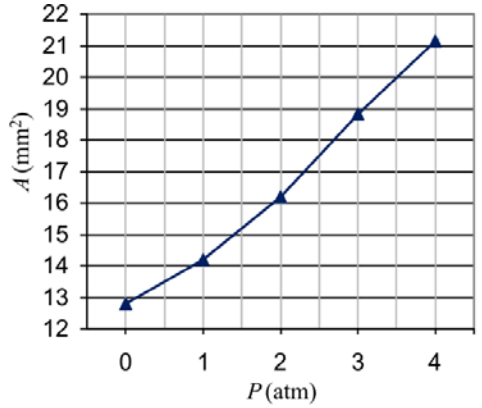

Figure 7.11. IVOCT characterization of balloon compliance

Figure 7.11 demonstrates the cross-sectional area, A, at different pressures. Since the balloon was not under pressure at 0 atm, the corresponding point was eliminated in estimation of the compliance. Using linear regression, a normalized compliance of 2.35 $(\mu L/atm).mm^{-1}$ was calculated.

7.7 Concluding remarks

We presented an innovative integration of IVOCT imaging in a balloon deployment setup. The resulting setup allows accurate real-time monitoring of balloon inflation under predetermined conditions and is a valuable tool to validate and optimize balloon designs. Using image analysis techniques, we assessed the balloon diameter and wall thickness at different pressures. Such assessment is important in controlling the balloon quality.

Although the focus was on characterization of the balloon quality, the proposed setup has many more applications. One of the goals of the balloon forming process is to obtain material with increased stiffness, which is achieved by heating and stretching. The mechanical properties of the resulting balloon are not known. IVOCT characterization could provide a non-destructive method to extract these properties. It can also be used in the development of future generation of minimally invasive devices, such as balloons and stents, and in clinical applications for angioplasty.

CHAPTER 8: IVOCT MONITORING AND CHARACTERIZATION OF PHANTOM DEFORMATION

Some researchers have proposed imaging of the vessel wall after angioplasty to assess the results. Among the proposed imaging modalities are intravascular ultrasound (IVUS) [31-34] and intravascular optical coherence tomography (IVOCT) [35-37]. IVOCT provides detailed cross-sectional imaging of the artery wall with a resolution in the order of ten micrometers, a resolution about 10 times better than that of IVUS. It has been shown that in comparison with IVUS, IVOCT provides a more accurate assessment of vessel wall layers [35] stent deployment [36] and plaque morphology [37].

In this chapter, we propose application of IVOCT monitoring in characterization of tissue deformation during angioplasty balloon inflation. In clinical practice, real-time intravascular imaging is not performed during balloon inflation. In order to visualize the artery, the operator deflates and withdraws the balloon catheter and replaces it with an imaging catheter to visualize the artery. In our setup, we use the OCTIB catheter, described in the previous chapter, to provide intravascular images during balloon inflation. Earlier, we proposed IVOCT monitoring and characterization of the balloon deformation. In the current chapter, we present extension of this method to characterize the deformation of the structure surrounding the balloon. This is done in two experimental scenarios involving a semi-compliant balloon and artery phantoms.

In the first scenario, three phantoms were fabricated with different mechanical properties [88]. Then we characterized the deformation of each phantom using IVOCT image analysis. The goal was to investigate if various mechanical properties of phantoms

resulted in a relevant and measureable difference in image-based characterization of their deformation during inflation of an angioplasty balloon. Sensing variation of mechanical properties of phantoms becomes more challenging in the presence of a balloon which is made of a much stiffer material. Such investigation is potentially helpful in characterizing the mechanical properties of atherosclerotic arteries or distinguishing the composition of plaques, using balloon inflation monitoring results.

In the second scenario, the goal was to investigate further the IVOCT capability by considering a more complex case. The balloon was in a folded state prior to inflation and the inner diameter of the phantom was smaller than the nominal diameter of the balloon. This allowed studying two stages of phantom deformation: during balloon unfolding and during balloon inflation. Additionally, the phantom was a three-layer tubular structure to better mimic a true artery. So, not only were the IVOCT images processed to provide the inner and outer diameter of the phantom during balloon unfolding and inflation, but the layer thicknesses were also determined. To our knowledge, no experimental result on monitoring the unfolding balloon has been published. The method proposed in this chapter could provide insightful experimental information to improve the balloon folding and balloon deployment strategies.

In this chapter, we first provide details of our experimental setup and the two experimental scenarios. Then, we present the applied image analysis techniques and the resulting characterization of phantom deformation. At the end, we provide our concluding remarks.

8.1 Experimental setup

The OCT system, described in Chapter 3, was applied in experiments. The phantoms were deformed using the OCTIB catheter, described in Section 7.2. A commercial syringe pump (PHD 4400, Harvard Apparatus) was used to inflate the balloon. A pressure transducer (MLH150PSB01A, Honeywell) was used to measure the inflation pressures. Two experimental scenarios were considered. In each scenario, we used the pump to inflate the balloon with incremental pressure steps. When the pressure was stabilized at each step, IVOCT monitoring was performed. A pressure range of 0 to 4 atm was applied.

8.2 Scenario 1: IVOCT monitoring of the deformation of single-layer phantoms with different mechanical properties during balloon inflation

For this scenario, three phantoms were produced with different silicone formulations [88]. Different formulations resulted in different mechanical properties, e.g., different degrees of elasticity. The mechanical properties were in a relevant range in comparison to those of a true artery [43]. We characterized the mechanical properties of the phantoms before the monitoring experiments, using uniaxial tensile tests. During the fabrication of each phantom, a rectangular sample was produced from the same mixture, which was subjected to uniaxial tensile tests. The tensile tests provided stress-strain data for each phantom material showing a linear elastic behaviour for each phantom material. The Young's modulus was obtained as the slope of the linear fit for each stress-strain curve. All phantoms that were used in this scenario had a single layer and had a nominal luminal diameter of 4 mm, which was equal to the nominal diameter of the balloon.

Figure 8.1(a,b) shows a sample IVOCT image, obtained in this scenario, in polar and Cartesian coordinates. The polymer sheath (PS), the balloon (B), and the phantom (P) are each represented by two contours, corresponding to their inner and outer surfaces. Contours, P_I and P_O, represent the phantom inner and outer surfaces. As the outer surface of the balloon overlapped the inner surface of the phantoms, both surfaces are represented by a single contour. Similar to the results in Chapter 7, the prism surface was used as a reference for image registration. The innermost contour represents the prism surface (R). The profile of the A-scan, depicted by a red line in Figure 8.1(a,b), is presented in Figure 8.1(c). As the outer surface of the balloon overlapped the inner surface of the phantom, the balloon surfaces and the phantom surfaces appear as three spikes on the A-scan in Figure 8.1(c). The surfaces of the polymer sheath and the prism also appear as spikes.

8.3 Scenario 2: IVOCT monitoring of the deformation of a three-layer phantom during balloon unfolding and balloon inflation

In this experiment, a more realistic and more complex case was considered, where the phantom had a luminal diameter of 3.2 mm, which was smaller than the balloon's nominal diameter, i.e., 4 mm. In this case, the balloon was inflated starting in a folded state. The phantom deformation thus occurred in two regimes: first during the balloon unfolding and then during the balloon inflation. In addition, the phantom was built with three layers which provided OCT signature of artery layers [88]. For simplicity, these layers were made with the same mechanical properties. A more complex phantom could be fabricated with different mechanical properties for each layer [88].

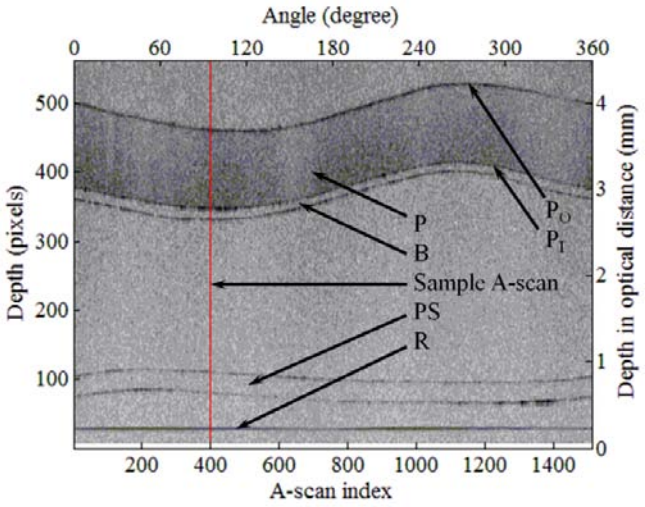

(a)

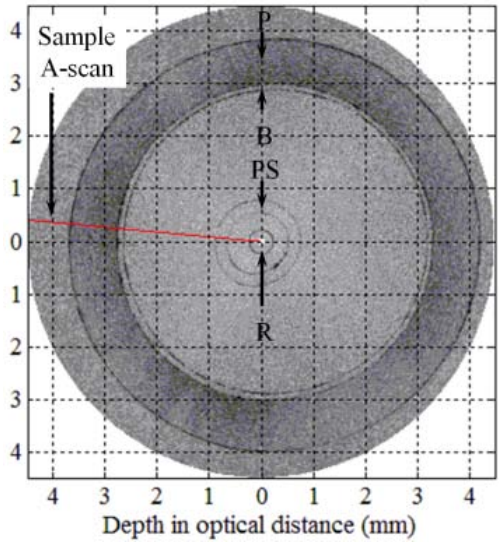

(b)

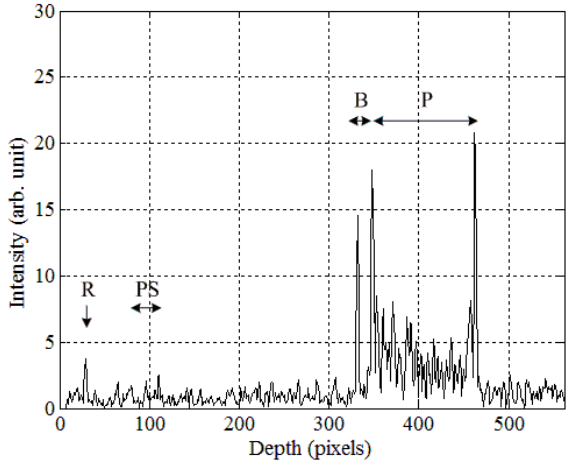

(c)

Figure 8.1. Sample IVOCT image in polar (a) and Cartesian (b) coordinates, and a sample A-scan (c) from Scenario 1

Figure 8.2(a,b) shows a sample image of a folded balloon inside the phantom in polar and Cartesian coordinates. In this figure, the artery phantom layers, phantom intima (I), phantom media (M), and phantom adventitia (A) are identified. Contours, C_I, C_M, and C_A, represent the intima, the outer media surface, and the outer adventitia surface. The image was partially distorted, due to deflection of light in the balloon folding flap.

The profile of the A-scan, depicted by a red line, in Figure 8.2(a,b) is presented in Figure 8.2(c). The balloon surfaces correspond to two spikes. The spike corresponding to the outer surface of the balloon overlapped the one corresponding to the intima. Media and adventitia can be distinguished as regions with different intensity levels.

8.4 Image analysis

In order to characterize the deformation of phantoms, various contours were detected using image analysis techniques. We present the algorithms that were applied to extract contours which delimited phantoms or phantom layers. All algorithms were applied to image matrices in polar coordinates. To describe these algorithms, we use the same notations, described in Section 7.5. In both scenarios, we applied the image registration method, described in Section 7.5.1.

In Scenario 1, phantoms' inner and outer contours, P_I, and P_O, were detected (see Figure 8.1(a)). In Scenario 2, contours C_I, C_M, and C_A, were detected (see Figure 8.2(a)). Each contour was classified as either a ridge or an edge.

In the following, we describe our ridge detection, edge detection and sequential algorithm to detect these contours. Then, we describe how pixel values of the detected contour nodes were converted to values in geometrical distance.

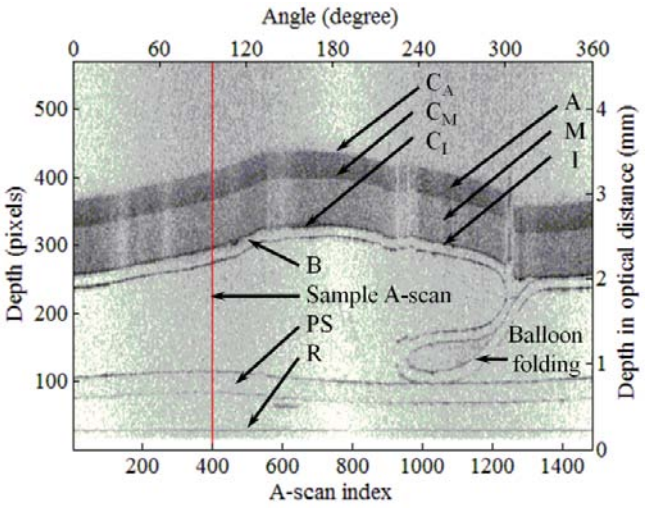

(a)

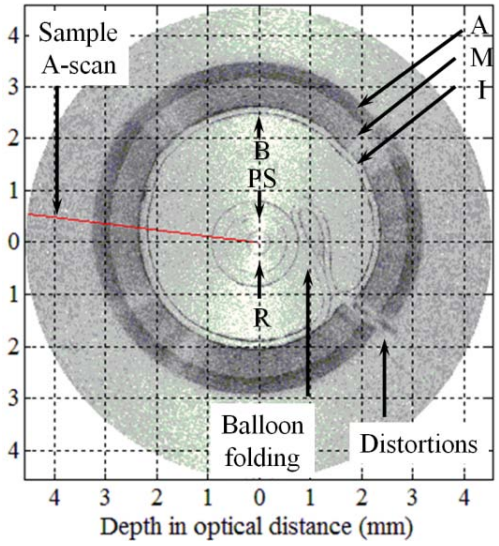

(b)

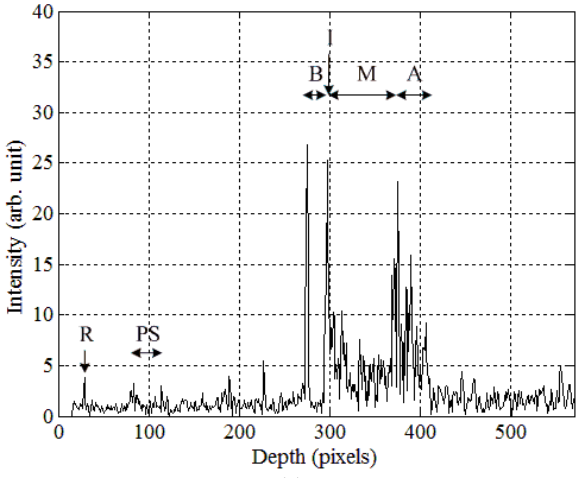

(c)

Figure 8.2. Sample IVOCT image in polar (a) and Cartesian (b) coordinates, and a sample A-scan (c) from Scenario 2

8.4.1. Ridge detection

The contours P_I, P_O, and C_I can be distinguished by spikes (local maxima) on most A-scans. These contours were detected as ridges, using a method similar to the one described in Section 7.5.2.

8.4.2. Edge detection

The contours C_A and C_M corresponded to borders of regions with different intensity elevations. These contours were detected as edges. Let j (where $j \in [1, Y]$) denote the A-scan index. A search interval, S_j, was obtained on each A-scan to isolate the contour of interest from other contours. An edge filter, F, was obtained from a function G, defined as:

$$G(i) = \begin{cases} -1 & i < 0 \\ 0 & i = 0,\ i \in [-w, w], \\ 1 & i > 0 \end{cases} \tag{8.1}$$

where w is a positive integer (in the applied algorithm, $w = 30$).

Based on the direction of the edge, $F = G$ was used to detect C_M, and $F = -G$ was used to detect C_A. Then, by finding the maximum of a cross-correlation, we detected the contour node on S_j. The cross-correlation was performed between the A-scan j and F:

$$i_j = \arg\max_{i \in S_j} \sum_{m=i-w}^{i+w} I(m, j) F(m - i), \tag{8.2}$$

where i_j was obtained as the depth of the detected contour node on A-scan j.

8.4.3. Sequential algorithm for contour detection

A sequential algorithm similar to the one described in Section 7.5.3 was used to detect phantom contours.

Detection of P_I, P_O, and C_I:

The contours, P_I in Scenario 1 and C_I in Scenario 2, not only represented the inner phantom surface, but also the outer balloon surface. Therefore, due to regional similarity in A-scan profiles, these contours were detected the same way that the outer balloon surface, B_O, was detected as explained in Section 7.5.3.

Detection of the contour, P_O, followed that of the contour, P_I. To detect the first node of the contour, P_O, a search interval was defined on the outer side of the detected first node for P_I. Then (7.2) was applied to find the first node for P_O. The process of finding the search interval using (7.6) and detecting nodes using (7.2) was continued sequentially on the subsequent neighbouring A-scans until one node was detected per A-scan.

Detection of C_A and C_M:

Detection of the contour, C_A, followed that of the contour, C_I. To detect the first node of the contour, C_A, a search interval was defined on the outer side of the detected first node for C_I. Then (8.2) was applied to find the first node for C_A. The process of finding the search interval using (7.6) and detecting nodes using (8.2) was continued sequentially on the subsequent neighbouring A-scans until one node was detected per A-scan.

Detection of the contour, C_M, followed that of the contours, C_I and C_A. To detect the first node of the contour, C_M, a search interval was defined between the detected first nodes for C_I and C_A. Then (8.2) was applied to find the first node for C_M. The process of finding the search interval using (7.6) and detecting nodes using (8.2) was continued sequentially on the subsequent neighbouring A-scans until one node was detected per A-scan.

In Scenario 2, at low inflation pressures, the balloon was still folded causing a distortion in some images. In such images, we detected the contours semi-automatically. An operator first selected A-scans which delimited the undistorted regions of the image. The segments of the contours C_I, C_M, and C_A corresponding to the undistorted regions were detected automatically, using the previously described sequential algorithm. Then the missing segments of the contours were obtained by interpolation performed by the user. At higher inflation pressures, where the balloon was unfolded completely, contour detection was automatic.

8.4.4. Conversion from pixel values to values in geometrical distance

Image analysis algorithms provided contour nodes in pixel values. Pixel values were converted to depth values in millimeters in geometrical distance. The depth values in geometrical distance were obtained using (7.8) with the same parameter values, provided in Section 7.5.4. All phantoms and phantom layers were built with different silicone formulations but with the same refractive index. A refractive index of 1.41 was used in our calculations for all phantom and phantom layers.

8.5 IVOCT characterization of phantom deformation

In this section, we present the characterization results, achieved by the applied image analysis techniques.

8.5.1. Scenario 1

The mechanical properties of the phantoms were characterized using the stress-strain data from uniaxial tensile tests. In these tests, rectangular samples from each silicone formulation were subjected to mechanical extension. Figure 8.3 presents these data for the three phantom materials in dots with different colors. Using linear fits, Young's modulus (*E*) values of 1.07 MPa, 0.44 MPa, and 0.09 MPa were obtained for the three phantoms. In Figure 8.3, these phantoms are identified as phantoms 1, 2, and 3, where Phantom 1 is the stiffest phantom and Phantom 3 is the softest phantom among the three phantoms.

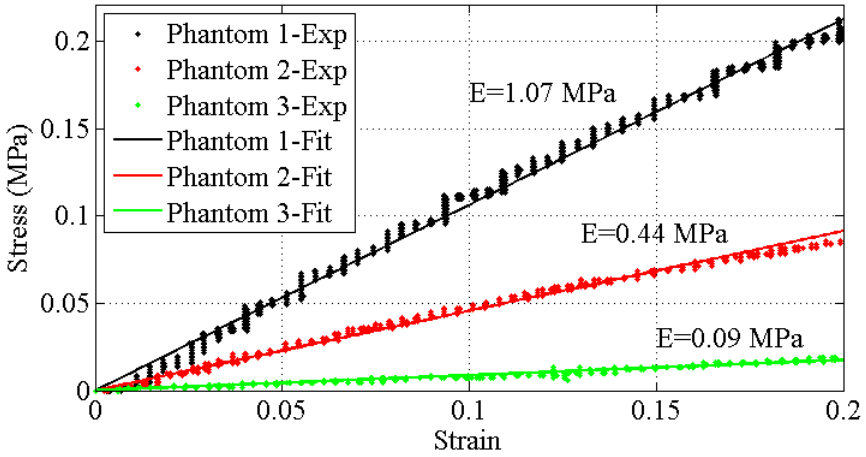

Figure 8.3. Stress-strain data from uniaxial tensile tests with linear fits for Phantom 1, Phantom 2, and Phantom 3, fabricated with different silicone formulation providing different mechanical properties

In the IVOCT monitoring experiments, images were acquired during balloon inflation for pressures from 0 to 4 atm with 0.5 atm steps. Figure 8.4(a,b) shows, as examples, the IVOCT images of the Phantom 2 at pressures of 0 atm and 4 atm. The detected inner and

outer surface contours of the phantom are shown in blue and red, respectively. From the detected contours, average inner and outer diameters of the phantoms were calculated.

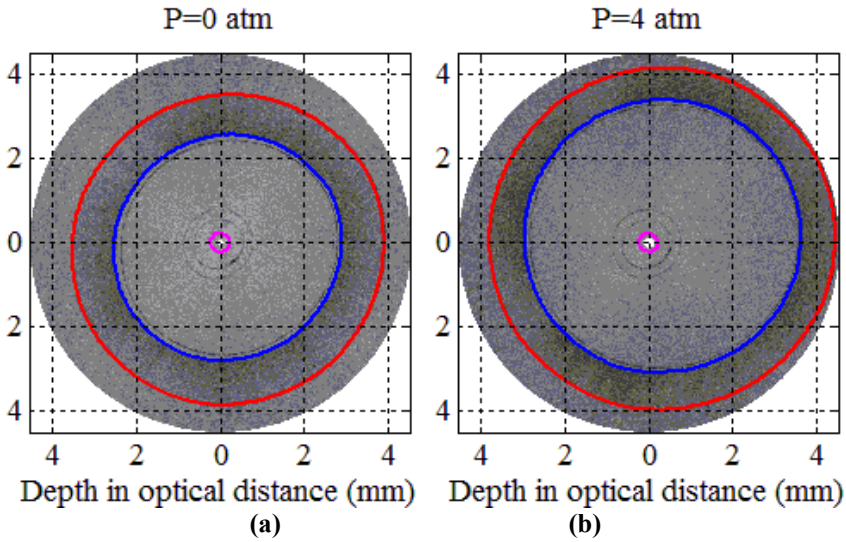

Figure 8.4. Contour detection in IVOCT images of Phantom 2 at pressures of 0 atm (a), and 4 atm (b)

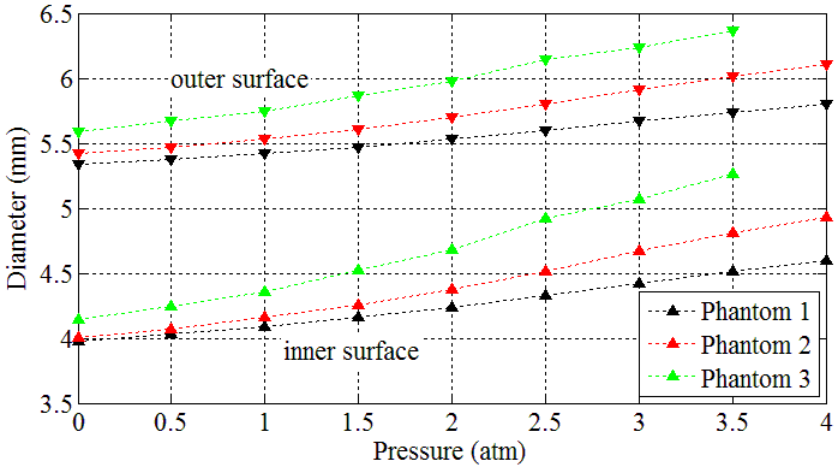

Figure 8.5. Comparison of inner and outer diameters obtained for the three phantoms from image analysis

Figure 8.5 presents these diameter values for different phantoms at different pressures. In the experiment involving Phantom 3, the maximum applied pressure was 3.5 atm, because at higher pressures, some sections of the phantom were outside the IVOCT image range. As Figure 8.5 shows, Phantom 1 had the smallest and Phantom 3 had the largest diameter growth rate. Therefore, considering the mechanical properties of the phantoms, IVOCT monitoring relevantly provided an indication of the mechanical properties of the

surrounding structure. This means that one may be able to detect variation in such mechanical properties, even in presence of a balloon which is made of a much stiffer material. Therefore, IVOCT monitoring during balloon inflation may also be used to characterize mechanical properties of arteries.

8.5.2. Scenario 2

In this scenario, IVOCT images were acquired for pressures ranging from 0 to 4 atm with steps of 1 atm. Figure 8.6(a) illustrates the IVOCT image of the folded balloon inside the phantom at pressure of 0 atm. Figure 8.6(b) presents the acquired image at pressure of 1 atm, where the balloon was partially unfolded. Figure 8.6(c) presents the acquired image at pressure of 2 atm where the balloon was completely unfolded. Figure 8.6(d) presents the acquired image at pressure of 4 atm where the balloon was inflated. In Figure 8.6(a-d), the detected blue and red contours correspond to the inner and outer surfaces of the phantom, respectively. These contours were used to measure the inner and outer diameters of the phantom.

Figure 8.7 presents the calculated average diameters. Based on IVOCT monitoring results in Figure 8.7, the phantom underwent two phases of deformation with different rates. The first phase corresponded to pressures between 0 and 2 atm when the balloon was still being unfolded. Therefore, in this phase the balloon did not contribute to resistance against the pressurization resulting in a larger diameter growth rate for the phantom. As Figure 8.6(c) shows, at the end of this phase the balloon was completely unfolded. The second phase corresponded to pressure values larger than 2 atm. Since at the end of the first phase the balloon was completely unfolded, in this phase, further pressurization inflated the balloon. Therefore, in this phase, the balloon and the phantom both resisted

the pressure, resulting in a smaller diameter growth rate for the phantom. IVOCT can not only monitor the evolution of the inner and outer diameters of the phantom, but also of the variation of the layer thicknesses.

Figure 8.8 demonstrates values for layer thicknesses averaged over the full angular range. Using error bars, this graph also presents the standard deviation of the thicknesses over the full angular range. A similar two-phase trend can be distinguished in the layer thickness variation. The rate of decrease in the layer thicknesses is larger during the balloon unfolding process than it is during the balloon inflation process.

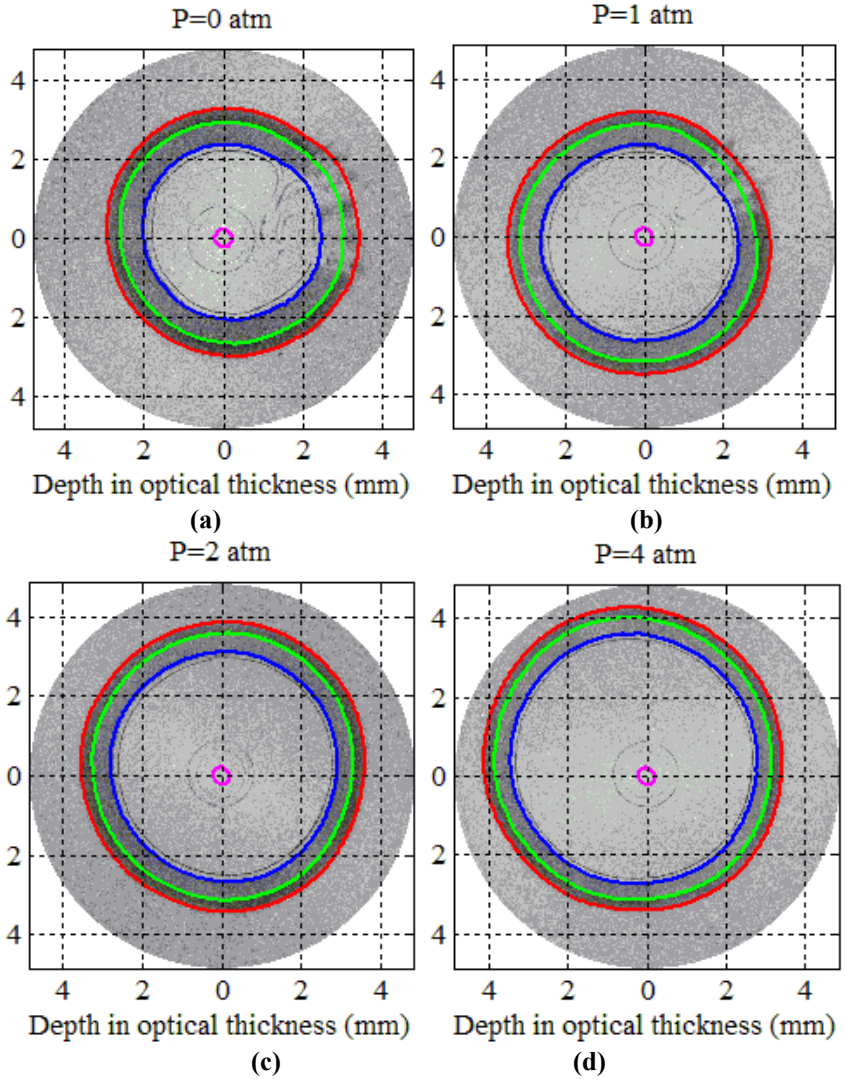

Figure 8.6. Contour detection in IVOCT images of the phantom during the balloon unfolding (a,b) and during the balloon inflation (c,d) process

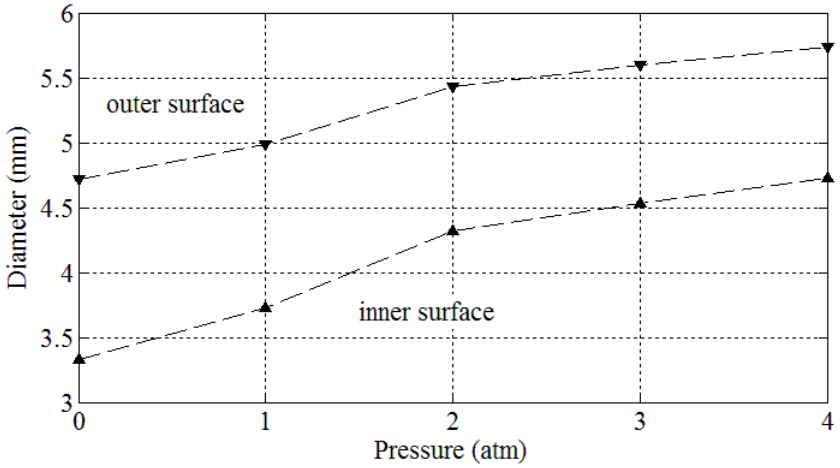

Figure 8.7. Inner and outer diameters of the phantom during the balloon unfolding and the balloon inflation process

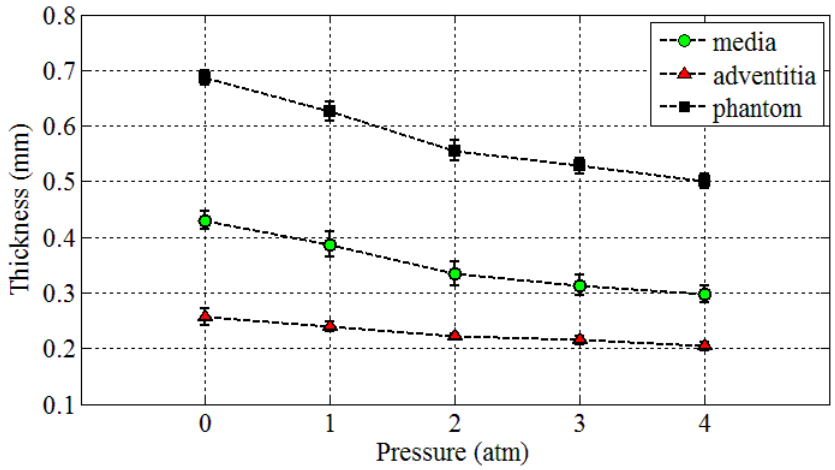

Figure 8.8. Layer thickness characterization of the phantom during the balloon unfolding and the balloon inflation process

All results presented so far, including the IVOCT images, presented in Figure 8.6, correspond to steady state, i.e., when the pressure is stabilized at each pressure step. A movie clip presenting layer thickness characterization during a continuous inflation is provided in [3]. This technique could potentially be useful to monitor the deformation of wall structure or the plaque in real-time for clinical or research purposes.

In the current balloon folding configuration, depicted as a C-shape in Figure 8.6(a), there was only one folded segment in the balloon. The balloon could also unfold starting with a different configuration, e.g., with multiple folds [89]. Regardless of the folding

configuration, we expect to see a similar two-phase trend for the diameter and thickness values versus pressure measurements. In the first phase, there is at least one folded segment in the balloon and in the second phase, the balloon is fully unfolded.

8.6 Concluding remarks

The goal of this chapter was to present IVOCT as a high-resolution imaging modality to characterize tissue deformation during balloon inflation. Using image analysis techniques, we characterized the deformation of several phantoms in two scenarios. The implication of the first scenario was that variation in mechanical properties of tissues could be distinguished by image-based characterization even in presence of a balloon. The proposed technique could be helpful in cardiovascular research and in clinical applications. It could provide an insight into the composition of the vessel wall structure or the plaque in atherosclerotic arteries. In further advanced applications, a mechanical analysis of the characterization results could lead to an estimation of mechanical properties of arteries which could be performed during balloon angioplasty or balloon predilation in a stent implantation procedure. In the second scenario, we obtained a characterization of deformation during a balloon unfolding and balloon inflation process. This provided information on the effect of the unfolding and inflation process on tissue deformation. Since a multi-layer phantom was used, a layer thickness characterization was also achieved. The proposed approach is not limited to phantoms. It could be used to study the response of arteries to different interventional procedures, applying different balloons, balloon folding methods, stents, or pressurization strategies.

CHAPTER 9: FINITE-ELEMENT SIMULATION OF DEFORMATION BASED ON IVOCT

Restenosis, as described in Chapter 2, has been correlated to arterial injury resulting from the excessive mechanical stretching of the vessel wall during balloon or stent deployment [14, 16]. This motivated research in mechanical analysis of angioplasty.

Some researchers have applied the finite-element method to simulate balloon angioplasty [44-46] and stent deployment [47-51]. Simulation models could be used to improve balloon or stent designs, or to provide insightful information for clinical applications, e.g., choosing the balloon size, the balloon folding strategy, and the pressurization strategy. In order for simulation results to be reliable, suitable validation techniques should be adopted. In the literature, there has been less effort on development of experimental validation techniques.

In many articles [47-51], simulation results are validated but only for the *free-expansion* scenario, where the balloon or stent is deployed alone, without a surrounding structure, such as an artery, real or synthetic. In order to validate free-expansion results, the investigators used manufacturers' data [47-49] or optical devices [49-51].

Some articles [44, 46, 48, 52] provide simulation results for different *confined* scenarios, where the deployment was performed in an artery model. In these articles, no experimental results were provided for the confined scenarios. The need for experimental validation was indicated in several articles [44, 51, 52]. Deployment in the confined scenario poses an experimental challenge in deformation monitoring and further complicates the modeling problem by adding the interaction between the artery and the

balloon or the stent. In a rare study [90], some researchers proposed a photography method to validate their simulated findings for the contact area between a stent and different artery models. This photography method, however, was limited to side views from particular angles.

In this chapter, we propose the application of IVOCT characterization results in simulation of angioplasty. To our knowledge, no research work has provided a comparison between simulation results and experimental results in the form of intravascular imaging during balloon inflation. IVOCT monitoring provides an experimental benchmark for simulation results obtained for both free-expansion and confined scenarios.

In this chapter, we first present how a simulation model can be generated for the balloon based on free-expansion results, such as those presented in Chapter 7. Then we present application of this model to simulate the two confined experimental scenarios, discussed in Chapter 8. Subsequently, we present a comparison of the simulation results and the experimental results. Finally, we provide our concluding remarks.

9.1 Generation of a simulation model for the balloon

The finite-element software Qform, developed at IMI and described in Chapter 5, was used for simulations. In all simulations, a direct solver was used. The loading corresponded to the pressurization range, applied in experiments, i.e., 0 to 4 atm. The loading range was divided into 160 steps.

In Chapter 7, we presented detection of balloon surfaces. A mesh was generated from the detected contour, corresponding to the outer surface of the balloon, using bar elements. By interpolating the detected balloon contour nodes, we obtained 80 bar elements.

A constitutive model was developed and tuned to the IVOCT monitoring results to provide a simulation model for the balloon. Based on *a priori* knowledge from in-house experiments, the one-term Ogden constitutive model [82] was chosen to describe the mechanical behaviour of the balloon. The strain energy function for this model is given by:

$$W = \frac{\mu}{\alpha}(\lambda_1^{\alpha} + \lambda_2^{\alpha} + \lambda_3^{\alpha} - 3) \tag{9.1}$$

where λ_i are the principal stretch ratios; μ and α are material constants.

Values for material constants, μ and α, were obtained by performing an optimization using the Levenberg–Marquardt algorithm [91], which is an iterative algorithm, implemented in MATLAB Optimization Toolbox (Mathworks Inc.). This method has been commonly used in material parameter optimization [92-94]. In this optimization procedure, an objective function, in the form of a sum of squared residuals, is minimized. In our optimization, a normalized residual error, *r*, was defined as:

$$r(\mu, \alpha, P_k) = \frac{1}{D_0}\left(D_{\text{sim}}(\mu, \alpha, P_k) - D_{\text{exp}}(P_k)\right), \tag{9.2}$$

where D_0 is the initial diameter of the balloon, P_k is the *k*th pressure measurement, D_{exp} is the balloon diameter from experiment, and D_{sim} is the balloon diameter from simulation. The optimization problem was formulated as finding the minimum of the sum of squared residuals:

$$\min_{\mu,\alpha} \sum_k \left(r(\mu, \alpha, P_k)\right)^2. \tag{9.3}$$

In the simulations, the boundary condition consisted of fixing a balloon node to eliminate rigid translations. Figure 9.1 presents a block diagram to perform this optimization. For

the first iteration, the initial values for parameters, μ and α were set arbitrarily. The loading range was from 0 to 4 atm. Iteration procedure was stopped, if the optimization goal was achieved to within a set tolerance. Otherwise, new values were generated for the model parameters based on the optimization scheme and the process was repeated.

Next, we present an application of this model in simulating the two experimental scenarios, discussed in Chapter 8.

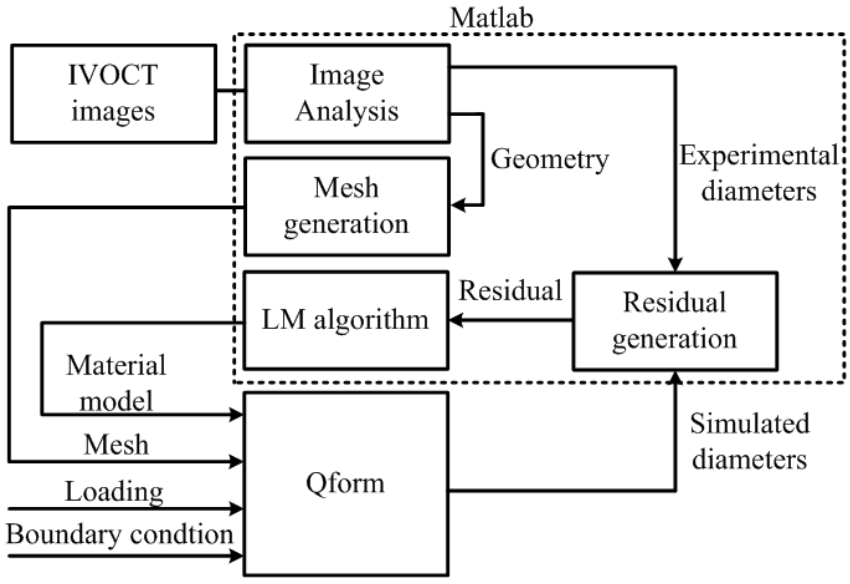

Figure 9.1. Optimization of material model parameters for the balloon

9.2 Simulation of Scenario 1

The detected inner and outer surface contours of the phantom, as presented in Chapter 8, were used to generate a mesh for the phantom. The mesh consisted of 6 layers of nodes in the radial and 80 nodes in the circumferential directions. The coordinates of the mesh nodes were obtained by interpolating the detected inner and outer contour nodes. Then, the Delaunay method [84], implemented in MATLAB (Mathworks Inc.), was used to generate a triangular mesh from the obtained nodes. The detected inner surface contour of the phantom was also used to generate a mesh for the balloon, as it represented the

interface between the balloon and the phantom. The balloon mesh consisted of 80 bar elements.

In the simulation, the boundary condition consisted of fixing a node on the outer boundary of the phantom mesh. In this preliminary analysis, we assumed a frictionless contact between the balloon and the phantom.

9.3 Simulation of Scenario 2

As was shown in Chapter 8, images of the folded balloon were locally discontinuous and distorted, due to deflection of light in the balloon folding flap. In these images, the distorted folded balloon was not detected. A mesh was generated for the balloon synthetically, rather than from contour detection. The balloon mesh consisted of 180 bar elements. The diameters extracted from the inner and the outer surface contours of the phantom were used to generate a ring-shaped mesh for the phantom. The mesh consisted of 6 layers of nodes in the radial and 120 nodes in the circumferential directions. The coordinates of the mesh nodes were obtained by interpolating the detected inner and outer contour nodes. Then, the Delaunay method was used to generate a triangular mesh from the obtained nodes.

The phantom that was used in this experiment was obtained from the mixture formulation, corresponding to the stiffest phantom material in the Experiment 2. Therefore, the same linear model was considered for this phantom.

In the simulation, the boundary condition consisted of fixing a node on the outer boundary of the phantom mesh. We assumed a frictionless contact between the balloon and the phantom.

9.4 Simulation results

In this section, we first provide the simulation model for the balloon which was generated by optimization. Then, we present simulation of deformation of phantoms using the obtained balloon model.

9.4.1. Generation of a simulation model for the balloon

In the process of finding optimal material parameters for the Ogden model for the balloon, the diameters measured on IVOCT images were considered as reference values. These values were obtained experimentally at 0.5 atm pressure steps. The optimization was performed on the same pressurization range to be used for phantom experiments. Figure 9.2(a) presents the IVOCT image of the balloon, acquired at pressure of 0 atm, when the balloon was not yet inflated to a round shape. The contour representing the outer surface of the balloon was detected and is shown in blue. The blue contour in Figure 9.2(a) represents the initial geometry of the balloon and was used to generate the mesh, depicted in Figure 9.2(b). To generate the mesh, the dimensions were converted from optical distance to geometrical distance.

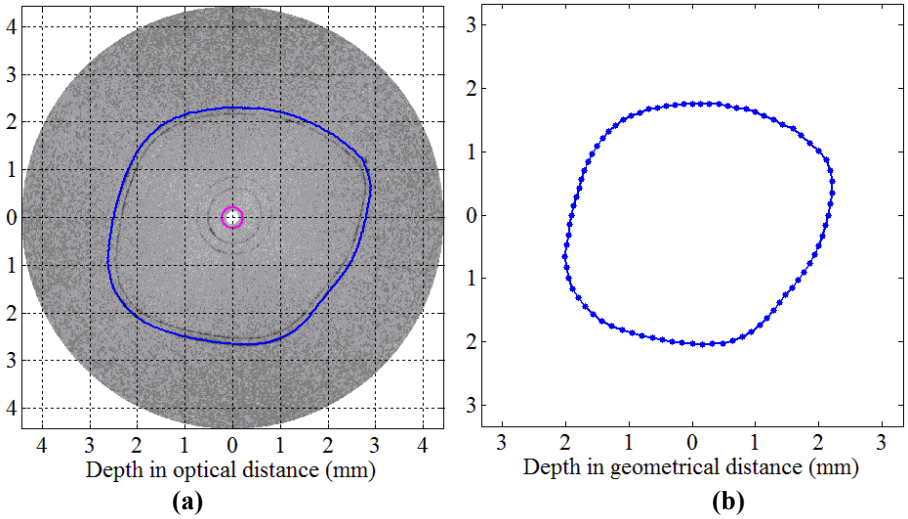

Figure 9.2. Balloon image at pressure of 0 atm (a), and balloon mesh (b)

Figure 9.3(a) shows the values of the Ogden parameters at different iterations during the optimization process. The residual error values at different iterations are presented in Figure 9.3(b). After 60 iterations, the optimization procedure stopped and values of μ=4.5 and α=4.6 were obtained. Figure 9.4 displays the diameters obtained from simulation in solid line, using the optimal material parameter values. For comparison, this figure also provides the experimental diameter values. The optimised material parameters may not correspond to the globally optimum solution. However, as Figure 9.4 shows they provide a good approximation of the balloon behaviour. The model that was obtained was used to simulate the balloon's response in the simulation of experiments involving phantoms.

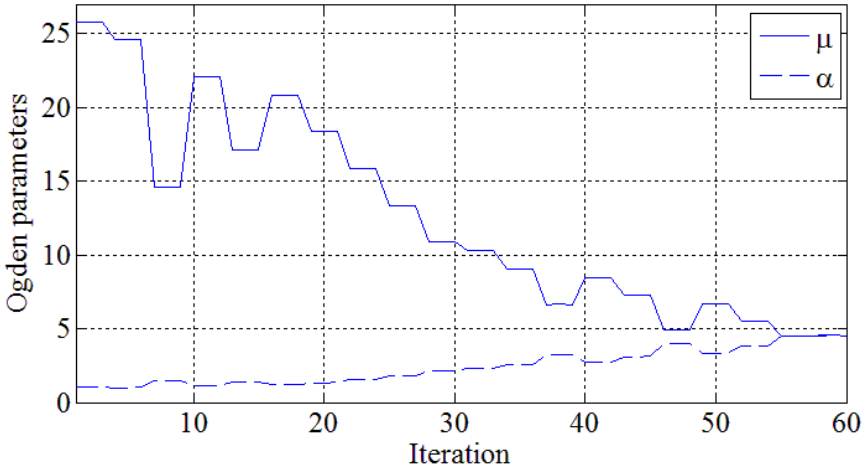

(a)

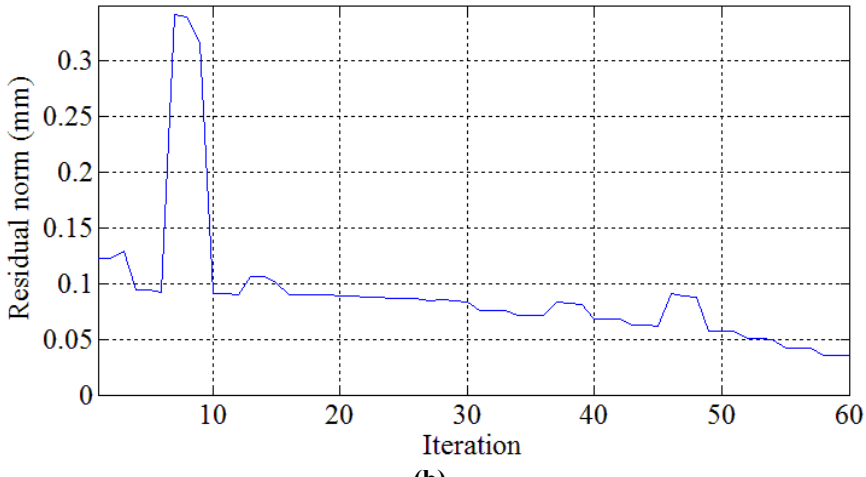

(b)

Figure 9.3. Ogden parameters (a) and the residual error (b) during optimization

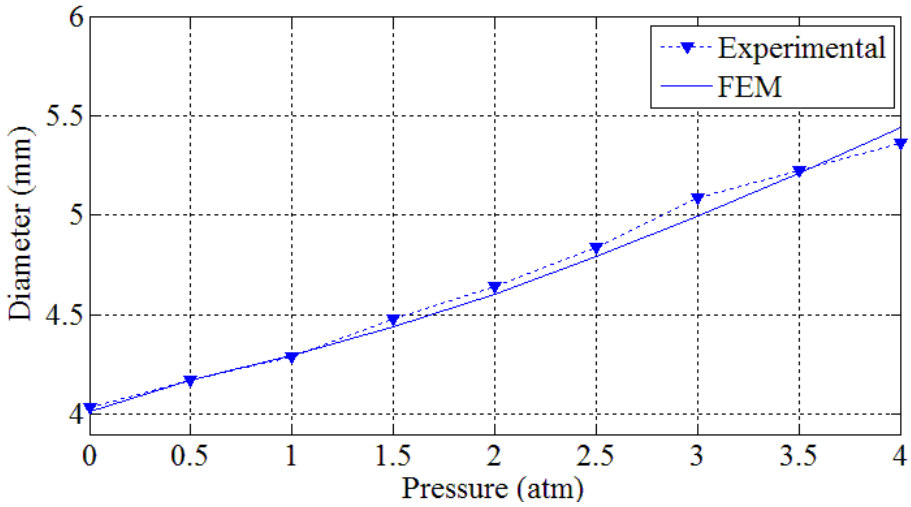

Figure 9.4. Comparison of diameter values obtained from experiment and from simulation with the optimized material parameters

9.4.2. Scenario 1

In this section, the results are presented for simulation of the first experimental scenario in Chapter 8. In the simulations, we used the linear elastic models for phantoms which were obtained from stress-strain data from uniaxial tensile tests (see Figure 8.3).

In the IVOCT monitoring experiments, images were acquired at 0.5 atm pressure steps. Figure 9.5(a,b) shows the IVOCT images of the Phantom 2 at pressures of 0 atm and 4 atm. The detected inner and outer surface contours of the phantom are shown in blue and red, respectively. The blue and red contours from Figure 9.5(a) were used to generate a mesh for the phantom. The blue contour also represented the balloon's outer surface and was used to generate a mesh for the balloon. The resulting meshes are depicted in Figure 9.5(c), where the scales are converted to geometrical distance. Figure 9.5(d) depicts the simulation result for Phantom 2 at pressure of 4 atm.

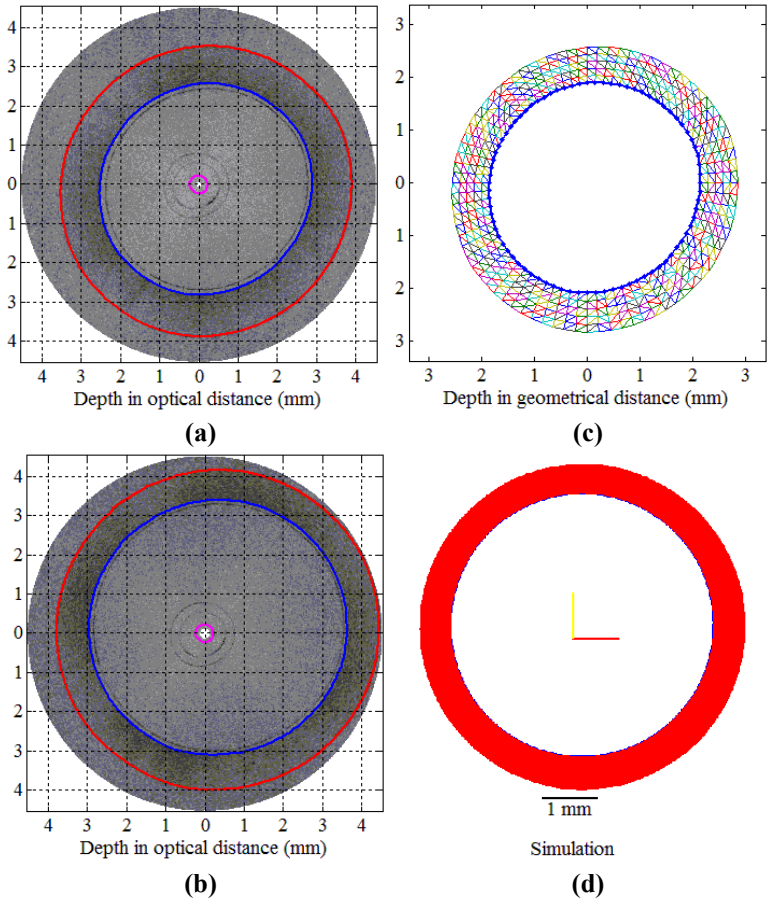

Figure 9.5. IVOCT images of Phantoms 2 at pressure of 0 atm (a), and 4 atm (b), the generated meshes (c), and the simulation result for the pressure of 4 atm (d)

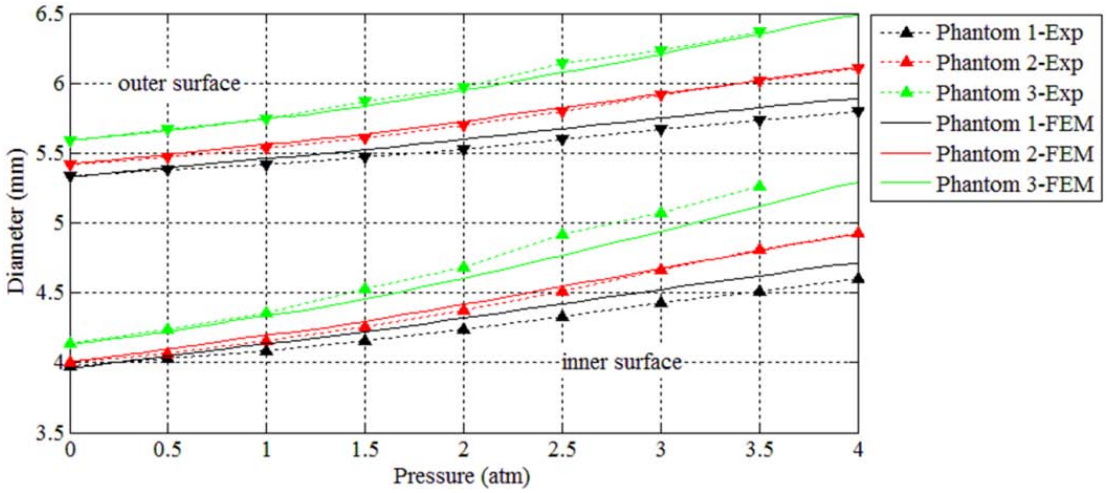

Figure 9.6 Comparison of inner and outer diameters obtained for the three phantoms from experiments and simulations

Figure 9.6 presents the inner and the outer diameters obtained from experiments and from simulations. According to this figure, there is a good agreement between the experimental

and simulation results for the Phantom 2. The inner and outer diameters of Phantom 1 are slightly overestimated in the simulation results. Nonetheless, the growth trends for these diameters seem similar in simulation and experimental results. For Phantom 3, there is a relatively better agreement between simulation and experimental results at lower pressures than at higher pressures.

9.4.3. Scenario 2

In this section, the results are presented for simulation of the second scenario in Chapter 8. The phantom in this scenario was made from a mixture with the same formulation as Phantom 1 in Scenario 2. Therefore, the same linear elastic model as Phantom 1 (see Figure 8.3) was used.

Figure 9.7(a-c), presents the IVOCT images together with the detected blue and red contours corresponding to the inner and outer surfaces of the phantom. Using the measured inner and outer diameters at pressure of 0 atm, a ring-shaped triangular mesh was generated for the phantom. This mesh is shown in Figure 9.7(d). A 1D-element mesh of the balloon was generated, synthetically, based on the phantom size, the balloon size and the balloon shape in the image. The blue contour in Figure 9.7(d) represents the balloon mesh. Figure 9.7(e) depicts the simulated geometry of the phantom and the balloon at pressure of 1 atm. In this figure, similar to the experimental result (Figure 9.7(b)), the balloon was partially unfolded. Figure 9.7(f) presents the simulation result corresponding to pressure of 2 atm. At this pressure, the balloon was almost completely unfolded.

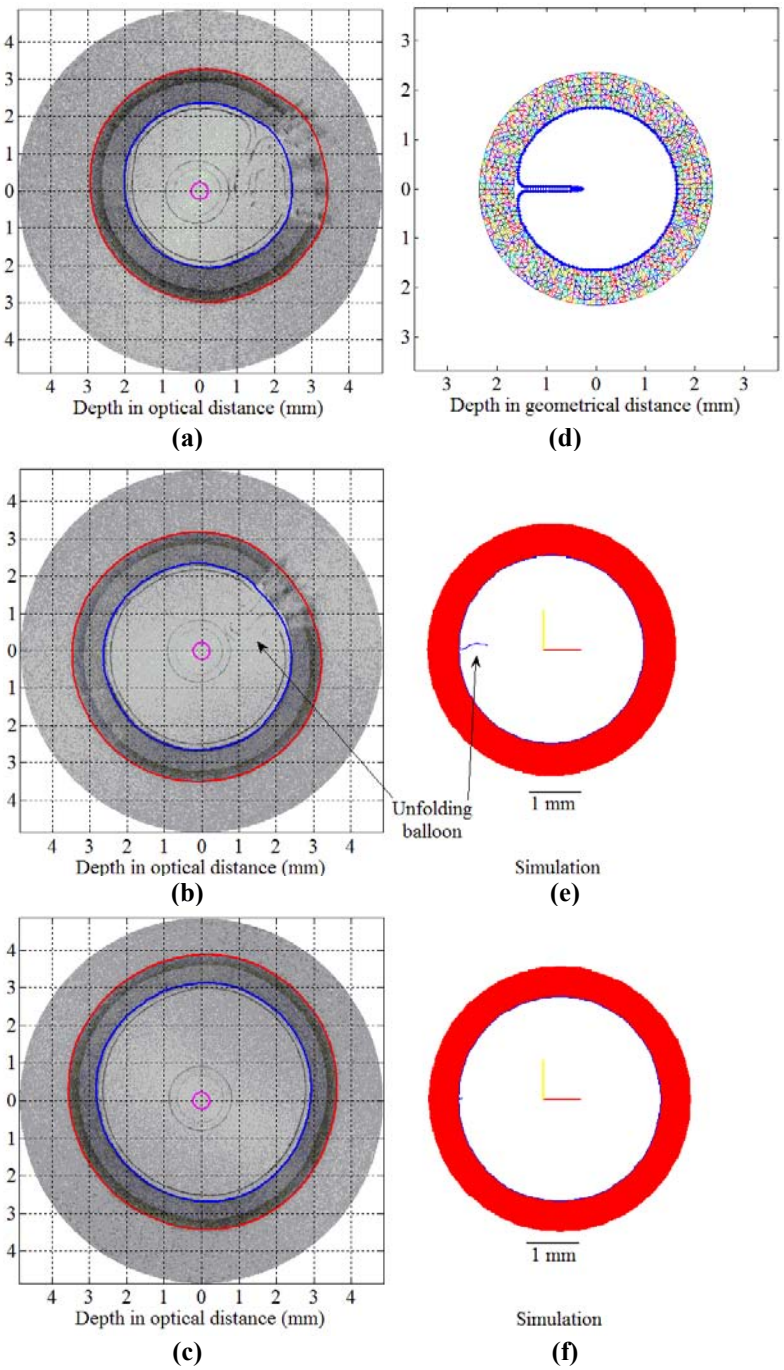

Figure 9.7. IVOCT image at 0 atm (a) at 1 atm (b), and at 2 atm(c), the corresponding mesh (d), and simulation results at 1 atm (e) and at 2 atm (f)

Figure 9.8 presents the inner and outer diameters, obtained from simulation and experiments. The simulation results capture the two-phase trend of the diameter growth for the phantom. In addition, in the simulation results, the balloon unfolded at nearly the

same pressure, i.e., 2 atm. The diameter values from simulation and experimental results have better agreement at lower pressures than at higher pressures.

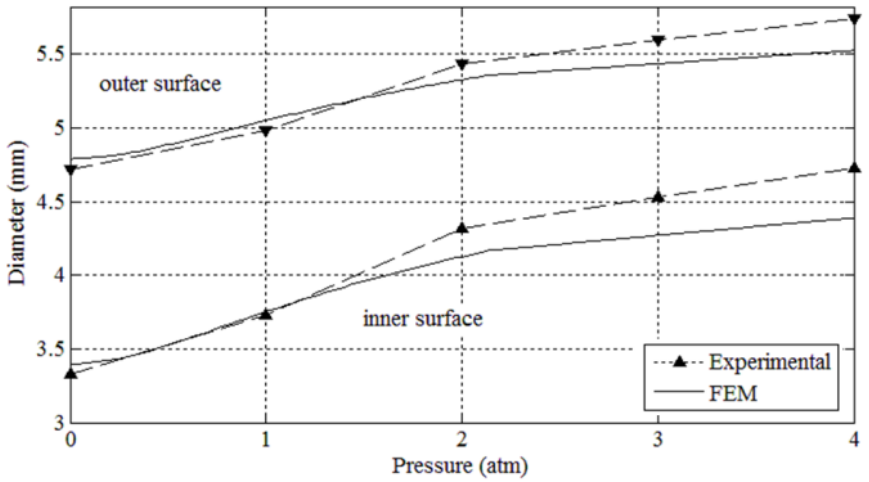

Figure 9.8. Inner and outer diameters obtained from experiments and simulations

9.5 Concluding remarks

The goal of this chapter was to establish the relevance of IVOCT monitoring for the validation of simulation models. In this preliminary study, we obtained good agreement between simulation and experimental results. The proposed technique could be beneficial in the modeling of angioplasty procedures, which is generally a challenging task. The need for reliable simulation results necessitates a validation strategy. We presented a comparison of cross-sectional monitoring and 2D simulation of balloon inflation inside phantoms. Future work may address a 3D scenario. A pullback of the IVOCT probe can provide the geometry of the structure in 3D which could be compared with 3D simulation results. IVOCT monitoring may also be used to validate the simulations corresponding to stent deployment and *in-vitro* angioplasty procedures involving real arteries.

CHAPTER 10: REAL-TIME CONTROL OF BALLOON INFLATION BASED ON FEEDBACK FROM IVOCT: EXPERIMENTAL VALIDATION IN AN ARTERY PHANTOM

In the current practice of angioplasty, the balloon deployment is performed manually. In such procedures, a syringe is used to inflate the balloon until the luminal diameter achieves a target value, the result being evaluated on X-ray angiography. In the literature, two main shortcomings have been associated to this approach. First, manual inflation renders the quality of results operator-dependent and prone to human error. Second, estimation of luminal diameter depends on angiograms which provide low-resolution silhouette views of the vasculature.

To address the first shortcoming, some researchers proposed the use of computerized inflation devices to inflate the balloon [53]. Clinical trials of such devices were also reported [54, 55]. In these trials, the focus was on using different pressurization rates. Some clinicians have also investigated real-time monitoring of pressure-volume data [61].

To address the second shortcoming, some clinicians have investigated the application of intravascular imaging techniques, e.g., intravascular ultrasound (IVUS) [31-34]. These techniques have been usually applied for verification of the results after the balloon or stent deployment. The process typically involves withdrawing the balloon catheter and replacing it with an intravascular imaging catheter to verify the post-deployment results. A few researchers demonstrated clinical application of integrated IVUS-balloon catheters [95-97] to monitor the results during balloon inflation.

We propose a combination of the above two approaches to achieve computerized control of balloon inflation, based on intravascular image analysis. To our best knowledge, no result has yet been published proposing such an approach to balloon inflation control. The reasons could be the pervasive application of IVUS which does not provide the desired resolution for this purpose, and also the unavailability of integrated imaging balloon catheters. We present computerized control of balloon inflation inside an artery phantom, based on feedback from IVOCT. IVOCT provides a resolution which is almost 10 times better than that of IVUS, rendering it an efficient approach for this application.

In this chapter, we provide details of our real-time lumen detection algorithm. Then, we describe our control methodology and hardware implementation. Subsequently, controlled balloon inflation results are presented and discussed. At the end, we provide our concluding remarks.

10.1 Lumen detection in IVOCT images

For controlled inflation experiments, we used the multi-layer phantom that was described in Scenario 2 of Chapter 8. Figure 10.1(a,b) illustrates an acquired OCT image of the balloon inside the phantom, in polar and in Cartesian coordinates. In this image, the balloon is not yet inflated and is in a folded state. Deflection of light in the balloon folding partially distorts the image. An example can be seen at 6 o'clock position in Figure 10.1(b). A sample A-scan is depicted by a red line. The "x" mark on this A-scan corresponds to the detected luminal node, as will be explained later.

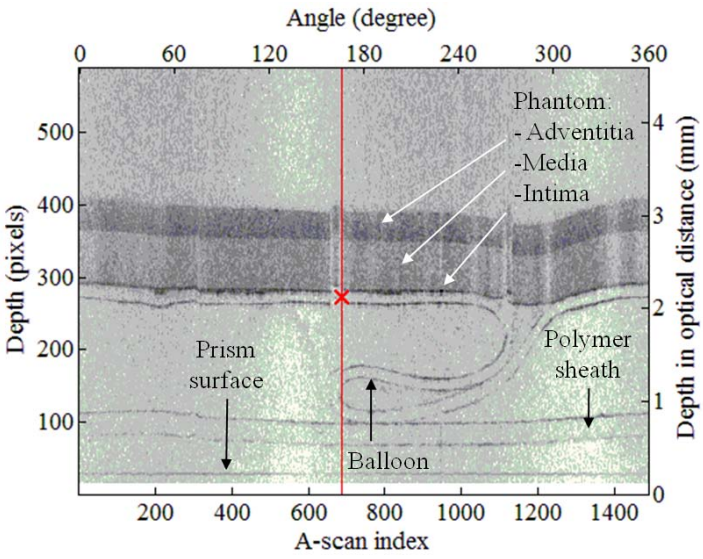

(a)

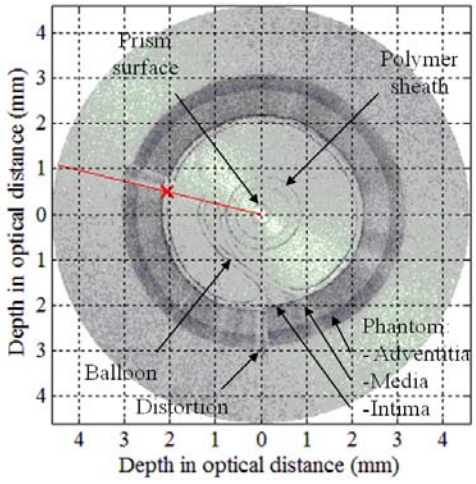

(b)

Figure 10.1. Sample image in polar (a) and Cartesian (b) coordinates

In order to estimate the luminal diameter of the phantom in real-time, a lumen contour was first detected. The detected contour was composed of *n* nodes, each of which was detected on the lumen border of a selected A-scan. These nodes could be detected on all A-scans. Therefore, the value of *n* could be as large as the number of A-scans. In our real-time control application, detection of a subset of nodes provided sufficient accuracy and increased processing speed. Additionally, contour detection was performed on a subset of images, e.g., 1 out of 8 frames or approximately every 400 milliseconds.

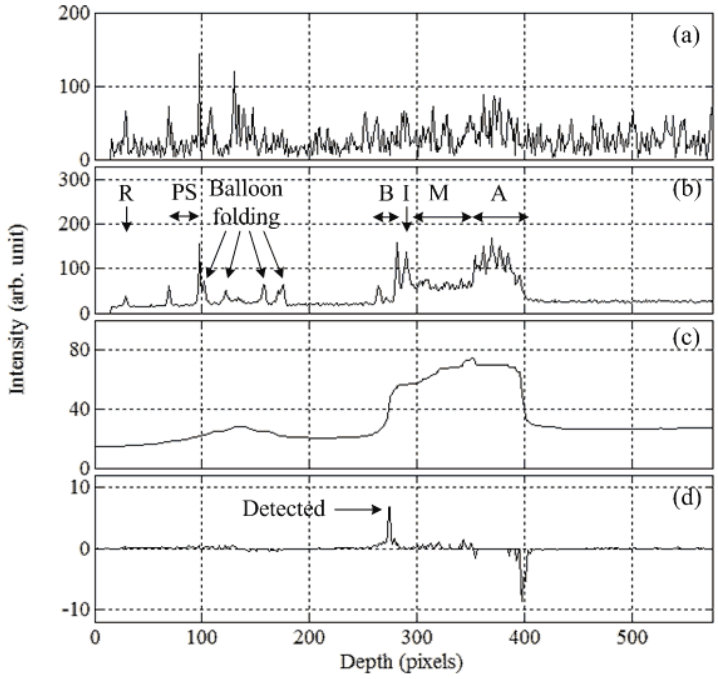

Figure 10.2. Description of different steps to extract one luminal contour node

Let j, where $j = 1, 2, ..., n$, denote the index to the A-scans processed to extract the contour nodes. In order to fully determine the coordinates of the contour nodes, on each A-scan, a depth index, i_j, was estimated.

The applied lumen detection steps were as follows:

Step 1: First, we selected *n* A-scans (in the results of this chapter, *n*=24), distributed at equal angles over a full rotation. Figure 10.2(a) demonstrates a sample A-scan, which is used to explain the detection steps. This is the A-scan corresponding to the red line in Figure 10.1.

Step 2: Some A-scans including the one presented in Figure 10.2(a) passed through a balloon folding region. Deflection of light in the balloon folding caused discontinuity and distortion in the phantom image posing a challenge to detect the lumen border from a single A-scan in a distorted region. This can be verified in Figure 10.2(a). We needed a robust detection for such A-scans. In order to provide the necessary

robustness in our algorithm, each element of the corresponding A-scan was averaged with the elements at the same depth of the w neighbouring A-scans on each side of the corresponding A-scan. Figure 10.2(b) shows how the application of averaging more clearly defines different regions. The balloon (B) and the polymer sheath (PS) can each be distinguished by a pair of spikes. The phantom media (M) and the phantom adventitia (A) can be identified as extended regions with different intensities. The phantom intima (I) and the prism surface (R) correspond to single spikes. The prism surface is represented by R, since it was used as a reference for automatic image registration in radial direction by adjusting the depth offset in each image. The image registration procedure was explained in Section 7.5.1.

Step 3: In this step, a median filter with a coarse scale was used to attenuate single spikes, such as those in Figure 10.2(b), corresponding to the polymer sheath, the balloon folding and the prism surface. This step created an extended elevated region, shown in Figure 10.2(c) with a width estimating the thickness of the phantom.

Step 4: The lumen border corresponded to the low-to-high edge of the obtained elevated region, generated in the previous step. In this step, we applied a gradient operation to detect this edge. As Figure 10.2(d) demonstrates, the lumen border was detected as the maximum of the gradient.

The applied algorithm, to detect the contour node on A-scan j, was formulated as:

$$i_j = \arg\max_i \hat{\nabla} F_s\left(\frac{1}{2w+1}\sum_{k=j-w}^{j+w} I(i,k)\right) \tag{10.1}$$

where I is the image matrix, F_s denotes median filtering with scale s and $\hat{\nabla}$ denotes the discrete gradient operation (as defined in (4.10)), with respect to the depth index, i. The

index, i_j, obtained from the detection algorithm, represented the node position in pixels. This value was converted to a depth value in millimeters in geometrical distance using the equation (7.8). Once the depth value for each contour node was calculated, the average lumen diameter was estimated.

Figure 10.3 demonstrates the detected lumen contour (in red) in 4 frames acquired when the balloon was inflated from a pressure of 0 atm to an approximate pressure of 3 atm. The detected nodes are visible on the contour in the form of red dots. The magenta circle in the center represents the detected surface of the prism. Detection in a sequence of images in the form of a movie clip is available in [5].

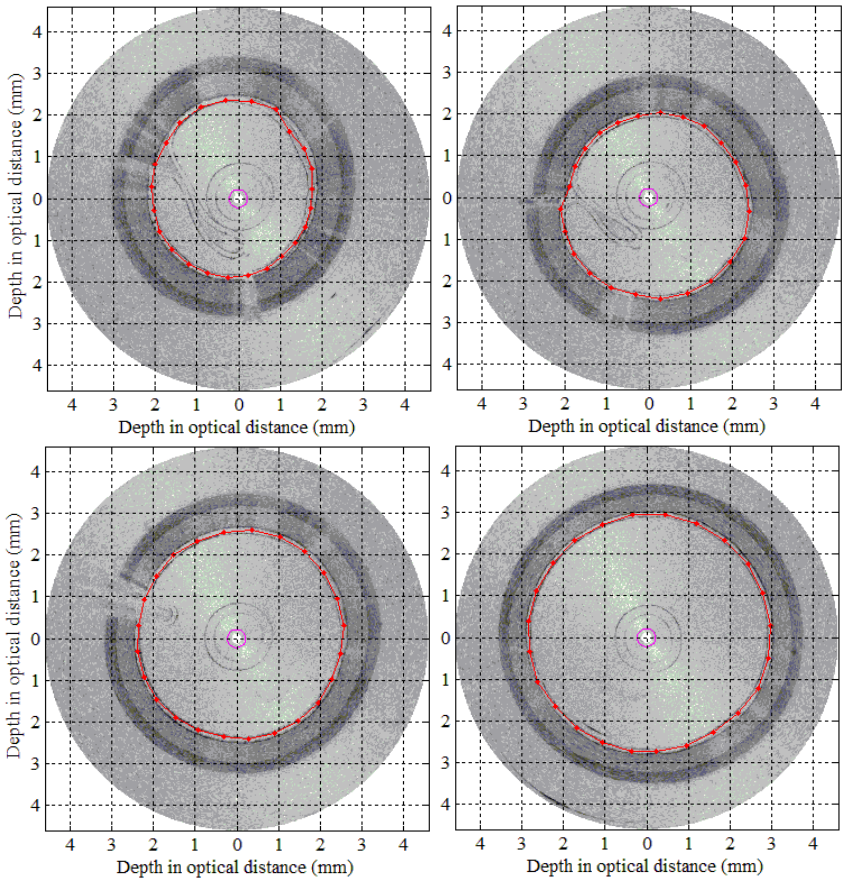

Figure 10.3. Detection of the luminal contour nodes represented as red dots

A great advantage of the above algorithm is that the detection can be performed in real-time. This is a key element that allows this algorithm to be used in a feedback loop to control the balloon inflation.

10.2 Control system architecture

In order to control the balloon inflation based on diameter feedback the method described in Section 6.3 was used. Figure 10.4 demonstrates the proposed balloon inflation control setup.

The sensing mechanism used in the control loop provided an average luminal diameter in real-time. It was composed of two main stages. In the first stage, an IVOCT imaging system acquired intra-luminal images in real-time. In the second stage, a PC performed image processing and calculated the average luminal diameter, D, in geometrical distance. The diameter, D, was subtracted from a desired target diameter, D_d, to generate an error variable, e. The error variable was sent to the controller. Alternate measurements could be made on the plant to assess its response to the pump action. A pressure transducer was connected to provide inflation pressures, as additional information. The pressure measurements were not used in the feedback loop.

The controller sent flow rate commands to the pump to achieve the target diameter. As Figure 10.4 depicts, the controller was composed of two components. Based on the sign of the error variable, e, the first component determined the direction, d, assigned to the plunger movement. The function of this component is demonstrated by a graph in Figure 10.4. Positive e indicated that the current diameter was smaller than the target diameter. In this case, a value of '+1' was assigned to d to move the syringe plunger in a direction to deliver more liquid to further inflate the balloon. Negative e indicated that the current

diameter was larger than the target diameter. In this case, a value of '-1' was assigned to *d* to move the syringe plunger in a direction to withdraw liquid to deflate the balloon. A small absolute value for *e* within a desired neighbourhood of zero (5 % of the target diameter) indicated that the current diameter had almost converged to the target diameter. In this case, in order to prevent from excessive switching in the direction of the plunger movement, no liquid was delivered or withdrawn. This neighbourhood of zero appears as a dead zone in the graph representing the first component of the controller. The second component of the controller was a gain, k_f, which determined the delivery or withdrawal rate. The controller provided the syringe pump with the flow rate *f*. Based on this flow rate, the syringe pump delivered or withdrew the liquid. In Figure 10.4, the actual delivered volume is represented by V_a. We estimated this volume by integrating the flow rate, *f*. This estimate is represented by V.

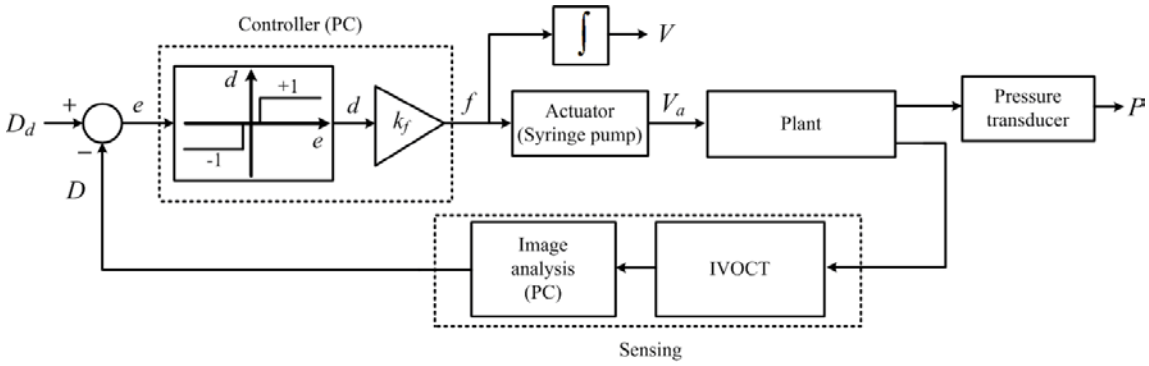

Figure 10.4. Balloon inflation control system

10.3 Hardware implementation of the control system

Figure 10.5 schematically demonstrates our hardware implementation of the control setup, proposed in Figure 10.4. A commercial syringe pump (PHD 4400, Harvard Apparatus) was used as the actuator for balloon inflation. The syringe pump was composed of a microcontroller and a stepper motor. It could provide a customized flow

rate or volume of a liquid. The output of the pump was connected to the IVOCT imaging balloon catheter by a tube and a T connector. Using a second T connector, a pressure transducer (MLH150PSB01A, Honeywell) was connected to the tubing to monitor and record inflation pressures. The sensing mechanism was composed of the OCT probe, the OCT system, and a PC. The data from the OCT system and the pressure transducer were imported to the PC through a data acquisition board (DAQ). The PC was used also as the controller, sending flow rate command to the pump in real-time through RS-232 programming.

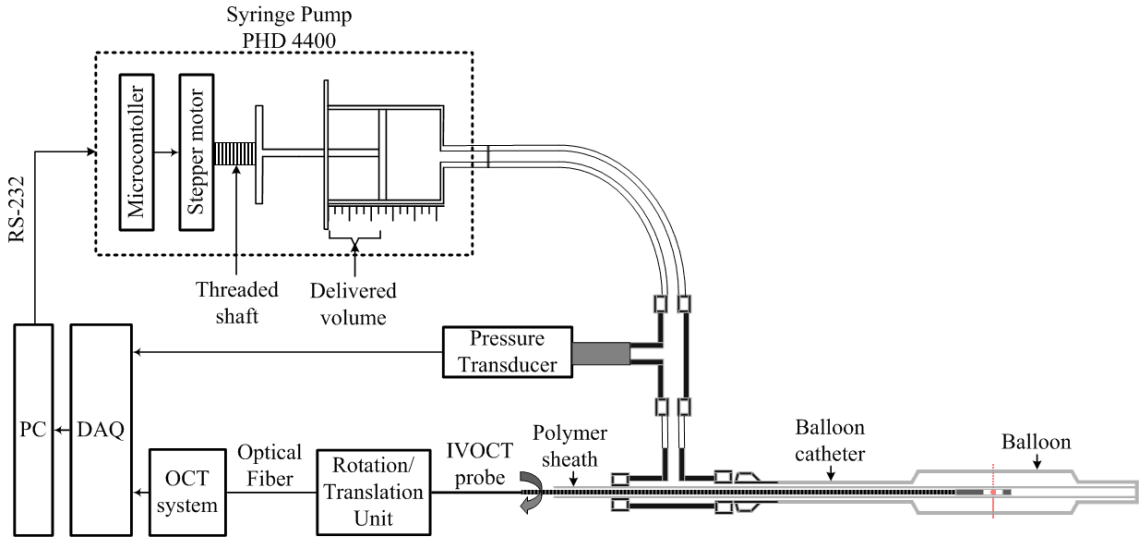

Figure 10.5. Hardware implementation of the balloon inflation control system

10.4 Results

In this section, we present and discuss the results of an experimental evaluation of the control system when using various values of the target diameter, D_d, and the flow rate gain, k_f. All diameter values are presented in geometrical distances. The values of the flow rate gain were adopted in a way that the balloon could be inflated in tens of seconds. This provides an inflation period relevant to those used in some clinical trials [55].

10.4.1. Various target diameter values

In angioplasty, before a balloon or a stent is chosen, a target luminal diameter is determined for the stenotic region of the artery, based on angiograms. The goal is to achieve this diameter using balloon angioplasty or stent deployment. In the following, we discuss the performance of the control system in providing various target diameters.

As mentioned earlier, in the experiments we used a semi-compliant balloon. In comparison with non-compliant balloons, the balloon can be further inflated to larger diameters once it achieves its nominal diameter of 4 mm. Usually a semi-compliant balloon is used to deploy the stents. Even though, a stent is not used in the experiments, a similar controlled-inflation procedure could be applicable in the case of stent deployment. Figure 10.6 presents the results, including the diameter, the volume, and the pressure versus time, of two control experiments with different values of target diameter but with the same flow rate gain, k_f. The initial diameter was approximately 3.5 mm. The applied target diameters were 4.1 mm and 4.3 mm. The value of the gain, k_f, was 500 mL/h. As Figure 10.6(a) shows, in both experiments, one could distinguish a small plateau region at an approximate diameter of 3.9 mm before the diameter reached its target value. This region corresponded to the relaxation that occurred when the balloon was completely unfolded. After the balloon was unfolded, it was further inflated until the target diameter was achieved. As Figure 10.6(a) shows, the growth rate of the diameter decreased after the balloon was unfolded. The reason is that once the balloon was unfolded, it significantly contributed to resistance against further deformation.

To compare the transient and steady-state behaviour of the controlled diameter in different experiments, we defined different performance characteristics, based on control

engineering conventions and notations [27]. The obtained characteristics are specific to our system and could change for different setups with different catheters, different balloons, different lengths of tubing, etc. Nonetheless, we provide these characteristics in order to provide an assessment of our experiments:

Rise time (T_r) was defined as the difference between the times at which 10 % and 90 % of the desired change in diameter were achieved. This parameter determined the speed of the control system to respond to changes in the target diameter.

Percentage overshoot (PO) represented a criterion to determine the excessive growth of the diameter beyond the target value. It was calculated by the following equation:

$$PO = \frac{D_{\max} - D_d}{D_d - D_0} \times 100, \tag{10.2}$$

where $D_{\max}$ is the maximum achieved diameter and D_0 is the initial diameter.

Settling time (T_s) was defined as the time, after which the convergence error remained smaller than 10 % of the difference between the initial and the target diameters:

$$\left|D - D_d\right| < 0.1\left(D_d - D_0\right) \tag{10.3}$$

Steady-state diameter (D_{ss}) was defined to determine the degree of convergence. After the settling time, the system was considered to be in steady state. We measured the average and standard deviation value of the diameter in steady state, to provide an expression, D_{ss}, for the diameter in steady state.

Before obtaining the above characteristics, a low-pass filter was applied to reduce noise in the diameter-versus-time measurements.

Table 10.1 presents the performance characteristics for the control experiments corresponding to Figure 10.6. When the diameter target value was increased from 4.1 to

4.3 mm, the rise time and the settling time were increased by approximately 6 and 7 seconds, respectively. The overshoot decreased for this increase in the target value. The settling times to achieve a desired diameter value were in a relevant range for a clinical application. In a previous clinical study [55] the researchers used up to 90 s of computerized inflation time followed by maintaining the target pressure for another 20 s.

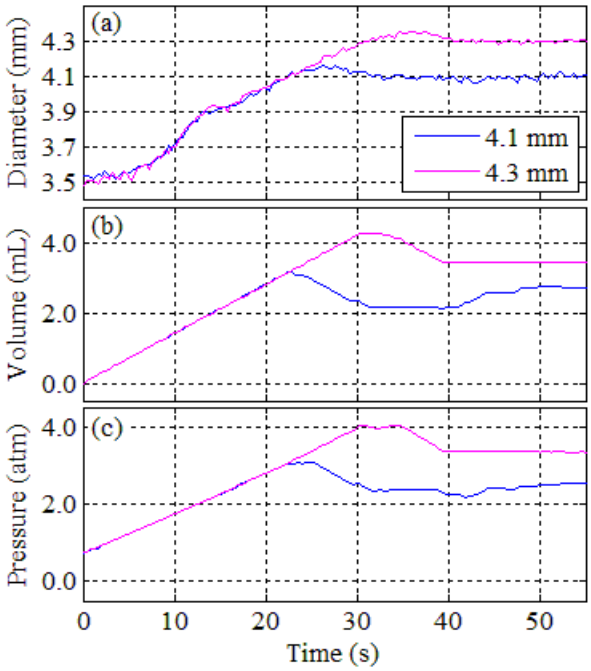

Figure 10.6. The diameter (a), the volume (b), and the pressure (c), obtained from control experiments applying different target diameters (4.1, 4.3 mm).

Table 10.1. Performance characteristics of control experiments using different target diameters (4.1, 4.3 mm)

	4.1 mm	4.3 mm
T_r (s)	15.0	21.1
PO (%)	8	6
T_s (s)	20.7	27.7
D_{ss} (mm)	4.11 ± 0.02	4.30 ± 0.03

10.4.2. Various flow rate gain values

In the literature, different researchers have investigated the effect of fast and slow inflation on the outcomes of angioplasty [86, 98]. However, the applied procedures are

not standardized. A computerized inflation device provides the opportunity to investigate the effect of predetermined inflation rates. We performed experiments to investigate the effect of changing the flow rate in the controlled inflation process. This also helped us test our system for higher inflation rates, which allowed less time for image analysis in the feedback loop.

Figure 10.7 presents the results, including the diameter, volume and pressure versus time, of three control experiments with the same target diameter but various values of the flow rate gain, k_f. The initial diameter was approximately 3.5 mm. The target diameter was 4 mm. Values of 500, 750 and 1000 mL/h were applied for the gain k_f. A plateau region corresponding to the balloon unfolding moment can be distinguished in Figure 10.7, at an approximate diameter value of 3.9 mm which is consistent with the experiments using different target diameters.

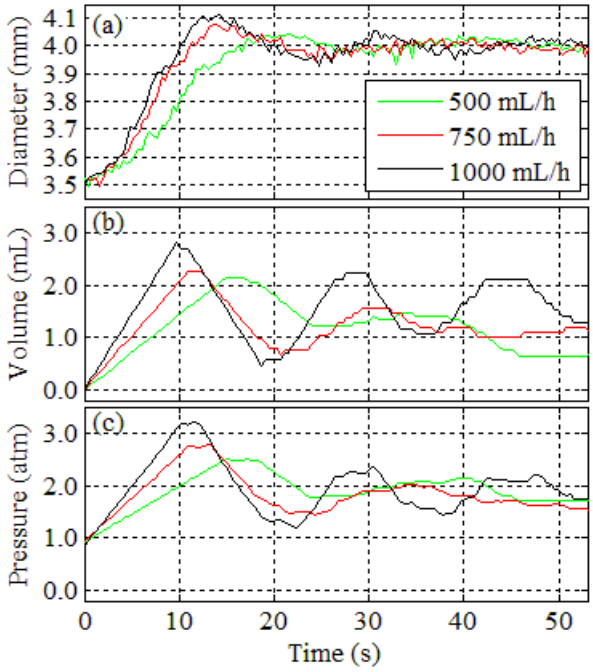

Figure 10.7. The diameter (a), the volume (b), and the pressure (c), obtained from control experiments using different flow rate gains (500, 750 and 1000 mL/h).

Table 10.2 presents the performance characteristics for the control experiments corresponding to Figure 10.7. These characteristics indicate that increasing the flow rate gain improved the rise time. However, increasing the flow rate gain also introduced oscillations in the diameter values, resulting in a larger overshoot and a larger settling time. The large overshoot and oscillations are visible in the graph corresponding to the flow rate gain of 1000 mL/h. The effect of oscillations was revealed in the larger standard deviation of the diameter in steady state corresponding to the gain value of 1000 mL/h.

Table 10.2. Performance characteristics of control experiments using different flow rate gains (500, 750 and 1000 mL/h)

	500 mL/h	750 mL/h	1000 mL/h
T_r (s)	11.7	8.1	7.7
PO (%)	8	15	21
T_s (s)	14.6	16.3	17.5
D_{ss} (mm)	4.00 ± 0.02	4.00 ± 0.02	4.00 ± 0.03

10.4.3. Sequential target diameter values

In angioplasty procedures, it is a common practice to apply a sequential pressurization procedure. First the balloon is pressurized to a target value; the pressure is maintained for a period of time; then the balloon is further pressurized to a higher target value [86]. We performed an experiment, where a sequence of diameter milestones was applied. The initial diameter was approximately 3.5 mm and k_f=500 mL/h. Two target diameters of 3.9 and 4.2 mm were applied, sequentially. Figure 10.8 presents the results of this experiment. In this figure, IVOCT images are presented at different diameter milestones together with the diameter, volume and pressure values. The balloon was first inflated to an unfolded state at a target diameter of 3.9 mm. This target diameter was maintained for several seconds. Then a new target diameter of 4.2 mm was applied. Consistent with what was observed previously, in this experiment the diameter growth rate during the second

phase was smaller than it was in the first phase. A movie clip is included in [5]. The movie clip presents the acquired IVOCT image sequence, synchronized with graphs which display the corresponding real-time diameter, volume and pressure.

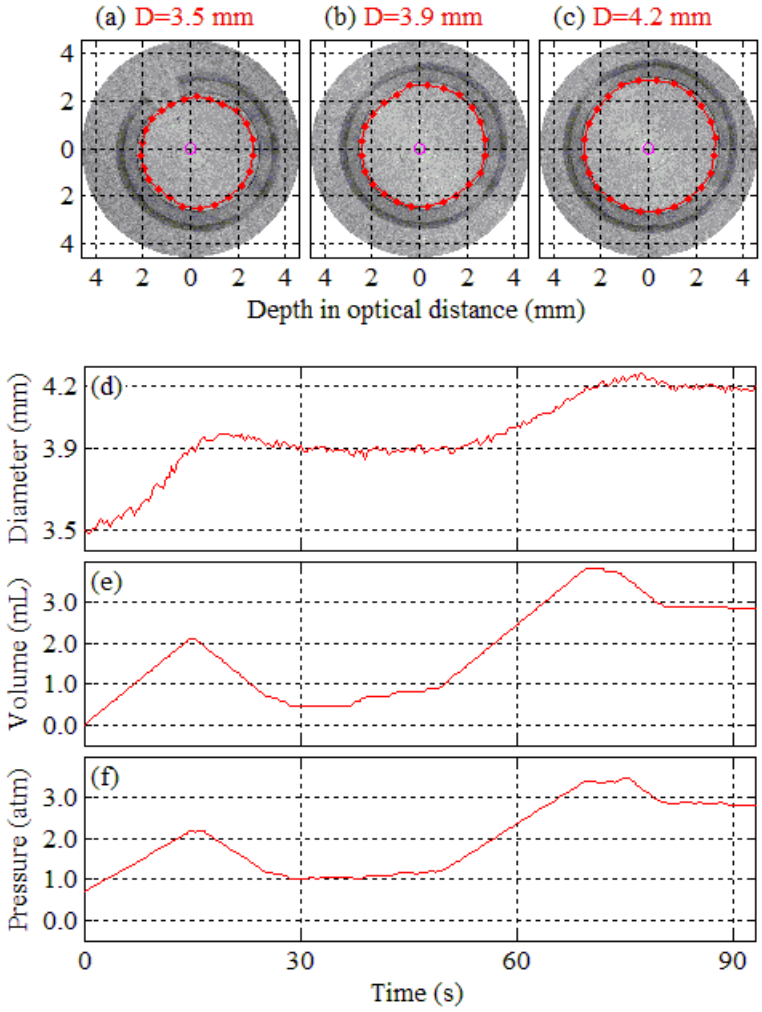

Figure 10.8. Acquired images at milestone diameters (a-c), the diameter (d), the volume (e), and the pressure (f) during the control experiment using a sequence of target diameters

As Figure 10.8 demonstrates, the proposed control setup has the flexibility to stabilize over various predetermined diameter values. At each diameter milestone, using the performance specifications, e.g., settling time, the diameter can be stabilized over predetermined periods of time. Further advanced algorithms may provide a diameter trajectory, rather than a constant target diameter, to provide a desired diameter at a desired time. In an angioplasty procedure, such advantage of this methodology could

potentially facilitate the process for an operator, providing safer and more precise conditions. Not only such an approach may improve the procedure, but also it may help standardize and compare the results across different institutes for further statistical analysis.

10.5 Concluding remarks

We presented a methodology to control the balloon inflation inside deformable structures such as arteries, based on feedback from IVOCT imaging. Using this methodology, we successfully controlled the movements of a syringe plunger based on real-time estimation of luminal diameter obtained from IVOCT images. In various experiments the luminal diameter of the phantom converged to different target diameters. The method was also robust to different flow rates. In the literature [43, 44], analysis of mechanical behaviour of the arteries is performed with the aim to improve the design of balloons or stents. The approach proposed in this chapter can provide precisely controlled conditions to validate the results of mechanical tests as well as mathematical models. From a clinical point of view, a controlled inflation could be a relevant tool to insure safe percutaneous coronary intervention procedures. In future work, more complicated control algorithms can be applied to improve performance characteristics. The control algorithm can be designed to also incorporate constraints on the inflation pressures. Future research may also address controlled procedures for stent deployment. In the next chapter, we apply the control method for balloon inflation in porcine arteries.

CHAPTER 11: REAL-TIME CONTROL OF BALLOON INFLATION BASED ON FEEDBACK FROM IVOCT: EXPERIMENTAL VALIDATION IN AN EXCISED HEART AND A BEATING HEART MODEL

In the previous chapter, we presented control of balloon inflation in an artery phantom. In this chapter, we extend the experimental validation of balloon inflation control to porcine arteries. In this preliminary study, experiments were performed using a compliant balloon. First, controlled inflation was performed in arteries of an excised porcine heart. The goal was to assess the performance of the control system in response to dynamics of the compliant balloons and real porcine arteries, a step forward from our preliminary work on phantoms [5]. In a further advanced setup, i.e., an *ex vivo* beating heart setup, we simulated two realistic aspects of the *in vivo* condition, namely, the presence of a blood flow and the presence of cyclic arterial contractions during the heart beat. We investigated if contour detection could be performed in the presence of blood. We also investigated if the control system could robustly provide convergence to target diameters in the presence of arterial contractions.

In the following, we first present the structure of the applied compliant balloon and the experimental setups. Then, we use a sample image to provide details on detection and diameter characterization. Subsequently, we present controlled balloon inflation results and concluding remarks.

11.1 IVOCT-imaging through a compliant balloon

A compliant balloon was used to deform the arteries. The compliant balloon was a silicone membrane which was glued to a balloon catheter. The balloon catheter was based on a transparent polymer sheath that contained and protected the probe. The probe was inserted in the balloon catheter, as shown in Figure 11.1. A liquid was used to inflate the balloon through a few holes punched in the polymer sheath. The liquid also facilitated the rotation of the probe and provided a transparent medium for imagery. In our experiments, we used water for balloon inflation. A soft tip was attached to the distal end of the balloon catheter to help navigate the catheter through the artery without causing damage. IVOCT imaging of the vessel walls was performed through the balloon.

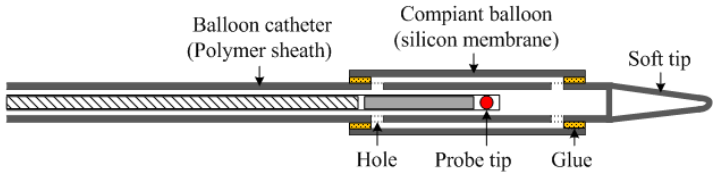

Figure 11.1. Schematic of the IVOCT probe inside the balloon catheter

11.2 Porcine heart experiments

Balloon inflation control experiments were performed in porcine coronary arteries in two different setups, one using an excised heart and the other using a beating heart model.

11.2.1. Excised heart model

Three days before the day of the experiment, a frozen porcine heart was allowed to defrost. On the day of the experiment, some excess segments of aorta were trimmed to facilitate access to coronary arteries. Through the aorta, the balloon catheter and the IVOCT probe were inserted in the left anterior descending (LAD) coronary artery for

experiments. Figure 11.2 illustrates the applied setup for this experiment. This setup allowed us to perform controlled inflation of the compliant balloon inside real arteries.

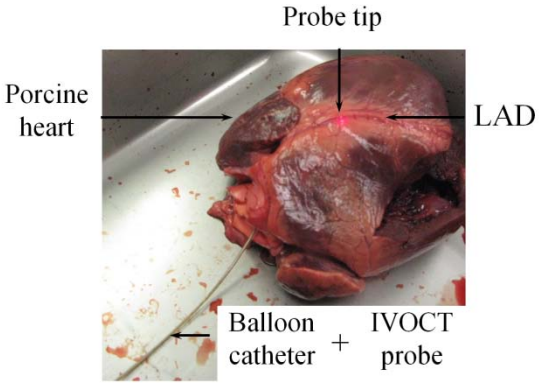

Figure 11.2. The excised heart setup

11.2.2. Beating heart model

The beating heart setup was provided by the Institute for Biodiagnostics (IBD) of the NRC. The experiments were conducted according to regulations laid out by the Canadian Council on Animal Care and were approved by a local Animal Care Committee of the NRC. The details of the beating heart model have been reported previously [73]. In this thesis, the same model was used to investigate the performance of our inflation control method. Commercial swine were acclimatized in the animal facility, one week before experiments. On the day of the experiment, the animal was first anaesthetized. The chest was opened and the heart was arrested. The heart was separated, rinsed and put in a cold saline bath. It was cannulated and prepared for perfusion. It was then hung over a funnel and perfused with body temperature blood and Krebs-Heinseleit solution in equal proportions. Once the heart warmed up and showed signs of activity, it was defibrillated to establish a normal rhythm. The preparation steps are illustrated in Figure 11.3. The balloon catheter and the IVOCT probe were inserted in the LAD artery through an introducer. The beating heart setup is illustrated in Figure 11.4.

The beating heart model was helpful in generating conditions similar to an *in vivo* setup without the associated complications of a full animal preparation. The setup remained functional for several hours. In our experiments, it allowed us to investigate the efficiency of our image analysis and control algorithms in presence of arterial contractions and blood flow.

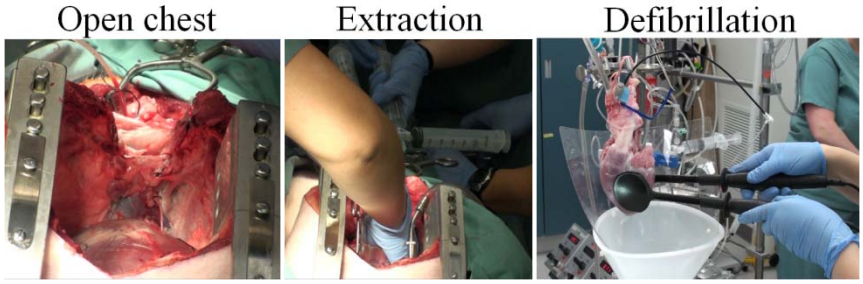

Figure 11.3. Main steps to prepare the beating heart setup

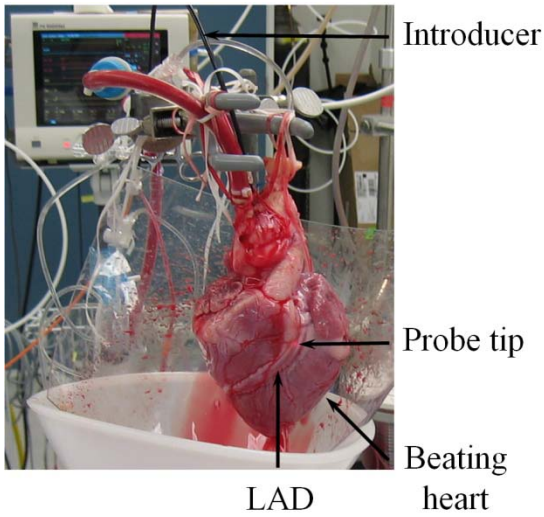

Figure 11.4. The beating heart setup

11.3 Monitoring balloon inflation in a porcine artery

In this section, we present a sample image obtained from a beating heart experiment. Figure 11.5(a,b) presents an IVOCT image in polar coordinates and in Cartesian coordinates, illustrating the balloon inside the artery. As this figure shows, the balloon is not inflated. The arterial wall is not visible at many angles, where the blood is occluding the view by scattering the light. The polymer sheath and the balloon are represented each

by two contours, corresponding to their inner and outer surfaces. The prism surface is represented by one contour.

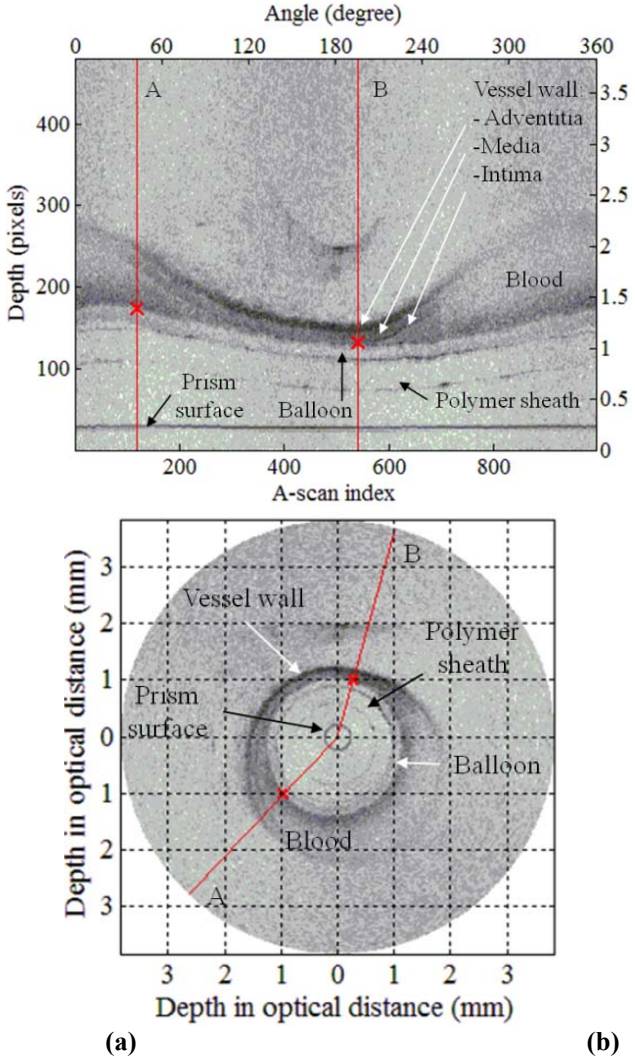

Figure 11.5. A sample IVOCT image in polar (a) and in Cartesian (b) coordinates

Two sample A-scans, A-scan "A" and A-scan "B" are depicted by red lines in Figure 11.5. The "x" marks on these A-scans are detected balloon nodes, as will be explained later. A-scan A corresponds to a sample depth profile for a segment of the image where visualization of the vessel wall was obstructed by blood. A-scan B corresponds to a sample depth profile for the segment of the image where the balloon was in the vicinity of the vessel wall and where there was almost no blood trapped between the balloon and the

vessel wall. In this segment, better visualization of the vessel wall structure was provided. The vessel wall layers, namely, intima, media and adventitia could be distinguished, as demonstrated in Figure 11.5(a).

11.4 Balloon detection in IVOCT images

In experiments on phantoms, described in the previous chapter, the inflation was controlled based on the estimated luminal diameter of the phantom. Similar to the phantom experiments, in the experiments on the excised heart controlled inflation was performed based on the estimated luminal diameter of the artery. However, in the beating heart experiments, the blood occluded visualization of the artery. In these experiments, controlled inflation was achieved based on the estimated diameter of the balloon rather than the lumen. This provided the same final results, because during the artery deformation the balloon diameter and the luminal diameter were equal. The balloon diameter was obtained from real-time detection of the contour corresponding to the balloon. The same lumen detection algorithm described in Section 10.1, was used this time to detect the balloon. Next, we describe the result of applying each step of the algorithm given by (10.1):

Step 1: First, we selected n A-scans, distributed at equal angles over a full rotation. As examples, Figure 11.6(a,b) demonstrates, respectively, the A-scan A and the A-scan B, as introduced in Figure 11.5. These A-scans are used to describe the algorithm performance for the two different regions, described previously.

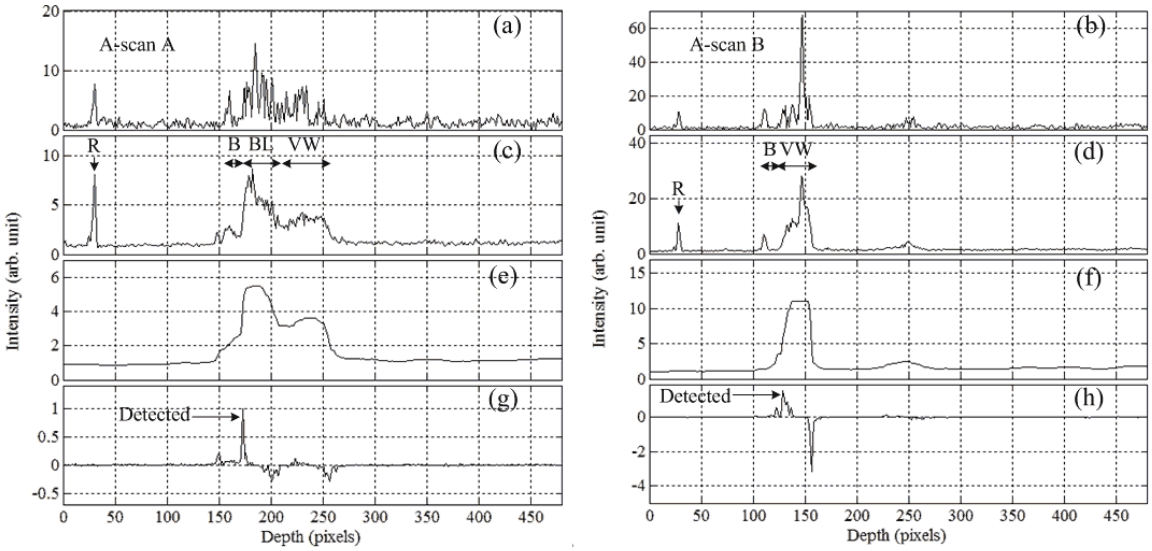

Figure 11.6. Description of different steps to extract luminal contour nodes, sample A-scans (a,b), averaging results (c,d), median filtering results (e,f), and gradient operation results (g,h)

Step 2: Each element of a selected A-scan was averaged with the elements at the same depth of the w neighbouring A-scans on each side of the selected A-scan. In Figure 11.6(c,d), it can be seen that application of this step to the selected A-scans more clearly defines different regions, e.g., balloon (B), blood (BL), and vessel wall (VW). These regions can be distinguished by peaks or regions with different elevations in intensity. The prism surface is represented by R, since it was used as a reference for automatic image registration in radial direction by adjusting the depth offset in each image. Image registration procedure was explained in Section 7.5.1.

Step 3: In this step a median filter with a coarse scale was used to attenuate single peaks that were not of interest. For example, it eliminated single peaks, such as those corresponding to the prism surface and the inner surface of the balloon. This step created an extended elevated region corresponding to the blood and the vessel wall as shown in Figure 11.6(e)) or the vessel wall as shown in Figure 11.6(f).

Step 4: The balloon node corresponded to the low-to-high edge of the obtained elevated region, generated in the previous step. In this step, we applied a gradient

operation to detect this edge. As Figure 11.6(g,h) demonstrates, the balloon node can be detected as the maximum of the gradient.

In the results of this chapter, we present 24 detected contour nodes for each image. We first tested our algorithm by post-processing a sequence of images, acquired during manual balloon inflation in a previously conducted beating heart experiment, where no control was applied. Figure 11.7 displays balloon detection in 4 sample images. The detected nodes are visible on the contour in the form of red dots. The magenta circle near the center represents to the detected surface of the prism. Detection in a sequence of images in the form of a movie clip is available in [6].

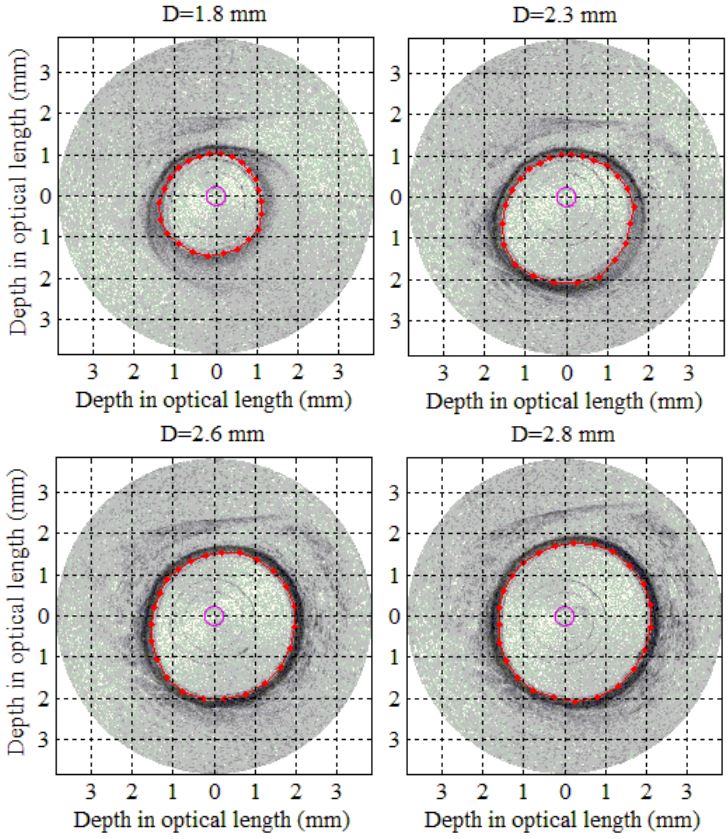

Figure 11.7. Detection of the balloon contour, provided by the detected red dots

The index, i_j, obtained from the detection algorithm, represented the node position in pixels. This value was converted to a depth value in millimeters in geometrical distance

using (7.8). Once the depth value for each contour node was calculated, the average balloon diameter was estimated.

11.5 Control system

The details of the control system and our hardware implementation were explained in Sections 10.2 and 10.3. As was mentioned previously, in the experiments on porcine hearts, a compliant balloon was used. Unlike a non-compliant balloon that is designed to achieve a fixed nominal diameter, the compliant balloon did not have a nominal diameter and could be inflated to various diameters, continuously, until it reached its burst pressure. This property gave us more flexibly in testing the control system for various values of the target diameter. Additionally, in comparison with non-compliant balloons, the compliant balloon was inflated in a more abrupt fashion. Therefore, the use of this balloon challenged the response time of the real-time control system. The speed of the system was further tested, using different inflation rates. The inflation rate has been suggested to be an important factor in some outcomes of angioplasty, e.g., restenosis [86, 98]. Therefore, the tests using various flow rates addressed an important aspect of the controlled inflation system.

11.6 Results

In this section, we provide results of controlled inflation in arteries of an excised and a beating heart. An investigation of the performance of the control system is presented for various experimental scenarios.

11.6.1. Inflation control in an excised heart

Figure 11.8 demonstrates the results of an experiment in which two target diameters of 2.3 and 2.7 mm were sequentially targeted. Figure 11.8(a-c) shows IVOCT images at different diameter milestones, i.e., at initial diameter and at each of the two target diameters. Figure 11.8(d-f) presents the real-time values of the balloon diameter, the delivered volume, and the inflation pressure. In this figure and the ones to follow, all diameter values are presented in geometrical distances. A supplementary video clip is available in [6]. The video clip presents the IVOCT images during balloon inflation, synchronized with the real-time values of the diameter, the volume, and the pressure.

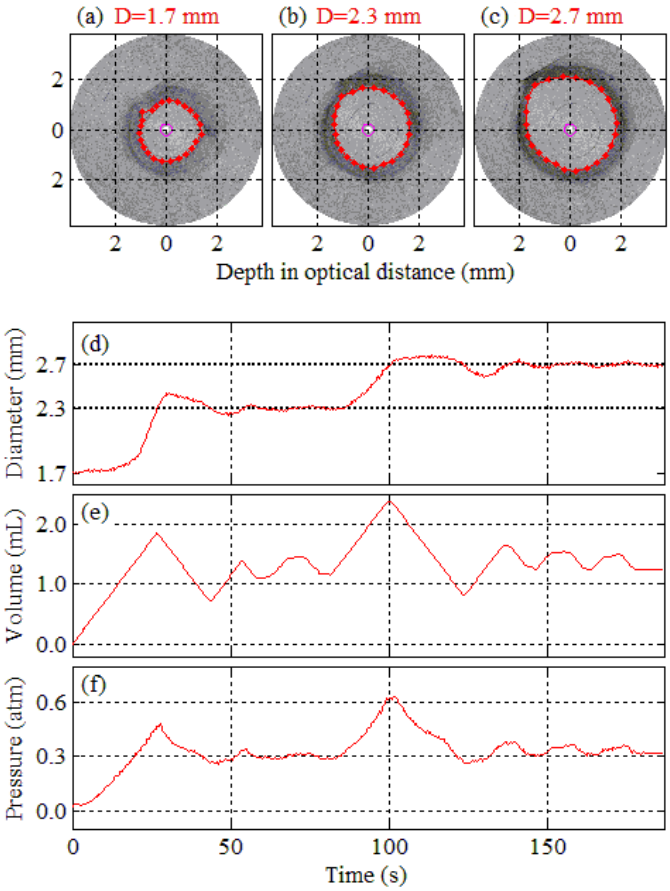

Figure 11.8. Results of balloon inflation experiment in an excised heart: IVOCT images (a-c), balloon diameter (d), delivered volume (e) and inflation pressure (f)

The results obtained from this experiment proved the ability of the control system to provide a good convergence to various target diameters. Therefore, the results of this experiment extended the validation of the performance of the control system to compliant balloons and real arteries.

The procedure used in this experiment could be used with various target diameter sequences and various durations to maintain each target diameter to study the responses of the vessel wall and plaques, e.g., deformation and rupture, under repeatable and controlled conditions.

Satisfactory results in this excised heart experiment, where the control system was employed, as well as successful balloon detection in beating heart images (see Figure 11.7), where the control system was not employed, set the table for control experiments in a beating heart setup which provides conditions close to *in vivo* conditions.

11.6.2. Inflation control in an artery of a beating heart

In this section, we present the results of three experimental scenarios. The results of the first scenario correspond to controlled inflation for various target diameters. The results of the second scenario correspond to three experiments with various flow rates. The results of the third scenario correspond to controlled inflation to achieve a sequence of various target diameters.

11.6.2.1. Various target diameter values

We performed two inflation control experiments, using the same flow rate but different target diameters. At both target diameters, the blood was not yet fully displaced and the balloon had not yet deformed the artery. The goal was to verify if the balloon diameter could be controlled in the initial inflation phase when it was still surrounded by blood.

Figure 11.9 presents the results, including the real-time values of the diameter, the volume, and the pressure, obtained from these two control experiments. In both experiments, the flow rate to deliver or withdraw the liquid was 250 mL/h. The initial diameter was approximately 1.7 mm. The target diameters were 2.1 mm and 2.3 mm.

In order to characterize and compare the system responses, in transient and steady state, we used the performance characteristics defined in Section 10.4.1. As will be shown, the obtained performance characteristics were affected by the superimposed effect of the oscillatory contractions of the artery. Nonetheless, they provided a preliminary assessment of the control system's performance. The margin for settling time was increased to 25 %. The reason for choosing a larger value was that, in our experiments, artery contractions constantly disturbed the diameter value. Therefore, the diameter values did not settle within previously used margins of the target diameters.

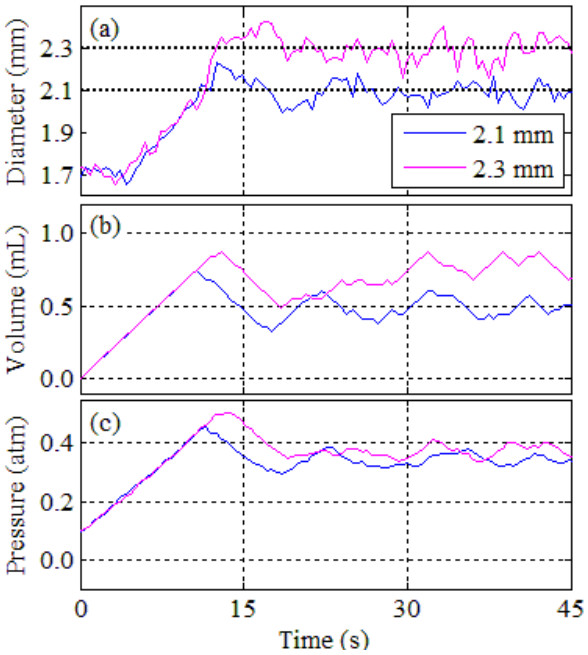

Figure 11.9. The diameter (a), the volume (b), and the pressure (c), obtained from control experiments using various target diameters (2.1, 2.3 mm).

The performance characteristics for this experiment are provided in Table 11.1. In both cases, although fluctuations were caused by arterial contractions, the difference between the target diameter and the steady-state average diameter was not larger than 20 μm. The rise time and the settling time were increased by 2 s and 1 s, respectively, when the target diameter was increased from 2.1 mm to 2.3 mm. The percentage overshoot decreased when the target diameter was increased.

Table 11.1. Performance characteristics of control experiments using different target diameters (2.1, 2.3 mm)

	2.1 mm	2.3 mm
T_r (s)	5	7
PO (%)	29	21
T_s (s)	18	19
D_{ss} (mm)	2.08 ± 0.04	2.29 ± 0.03

11.6.2.2. Various flow rate gain values

We performed three control experiments with the same target diameter but various values of the flow rate. Figure 11.10 presents the results, including the real-time values of the diameter, the volume and the pressure obtained from these control experiments. The initial diameter was approximately 1.7 mm. The target diameter was 2.6 mm. To control the diameter in these experiments, delivery and withdrawal of liquid was performed at flow rates of 100, 250 and 400 mL/h. At the target diameter, the blood was displaced and the artery was deformed by the balloon.

Table 11.2 presents the performance characteristics of the control system. The difference between the target diameter and the steady-state average diameter was in the order of 10 μm. Increasing the flow rate improved the rise time. The rise time corresponding to the flow rate of 100 mL/h was significantly larger than it was in the other experiments, resulting in a much slower convergence. Although increasing the flow rate could improve

the rise time, it was expected to increase the percentage overshoot or oscillations in delivery/withdrawal stages as was also observed in experiments with phantoms [5]. Such effect was confirmed in the calculated percentage overshoots and standard deviations of the steady-state diameter.

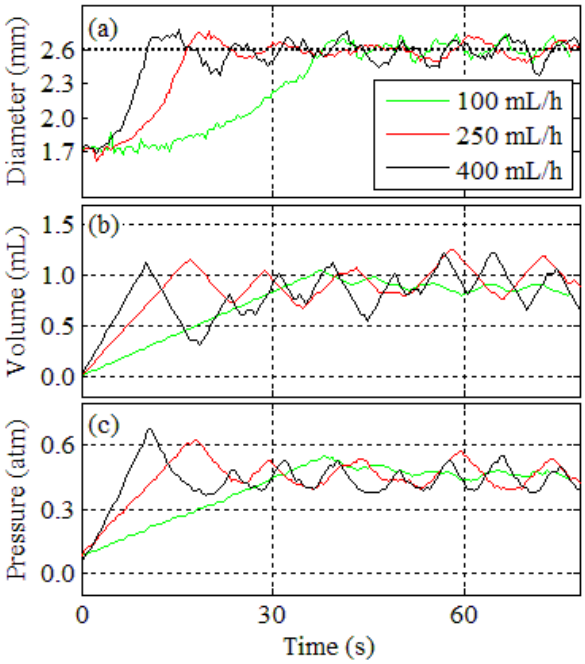

Figure 11.10. The diameter (a), the volume (b), and the pressure (c), obtained from control experiments using different flow rates (100, 250 and 400 mL/h).

Table 11.2. Performance characteristics of control experiments using different flow rate gains (100, 250 and 400 mL/h)

	100 mL/h	250 mL/h	400 mL/h
T_r (s)	22	9	5
PO (%)	13	16	16
T_s (s)	37	17	11
D_{ss} (mm)	2.61 ± 0.06	2.60 ± 0.06	2.60 ± 0.09

11.6.2.3. Sequential target diameter values

In this subsection, we present a case, where a sequence of previously scheduled diameter milestones was applied. The initial diameter was approximately 1.7 mm and the flow rate was 250 mL/h. Figure 11.11 shows the acquired IVOCT images, and graphs which display the corresponding real-time values of the diameter, the volume and the pressure.

Figure 11.11(a) shows that at the diameter of 1.7 mm, the balloon was surrounded by blood and was in vicinity of the vessel wall between the 4 o'clock position and the 8 o'clock position. Figure 11.11(b) presents the IVOCT image acquired when the balloon was first inflated to a diameter of 2.6 mm. At this diameter the balloon displaced the blood and deformed the artery. This IVOCT image revealed that at this location, there was a bifurcation at 3 o'clock position. The edge detection algorithm could detect the balloon in the bifurcation area, despite the reduced contrast in this region. At the next step, the balloon was inflated to a diameter of 2.9 mm, further deforming the artery, as shown in Figure 11.11(c). Finally, Figure 11.11(d) shows the balloon was deflated to a diameter of 2.2 mm, where the balloon was again surrounded by blood.

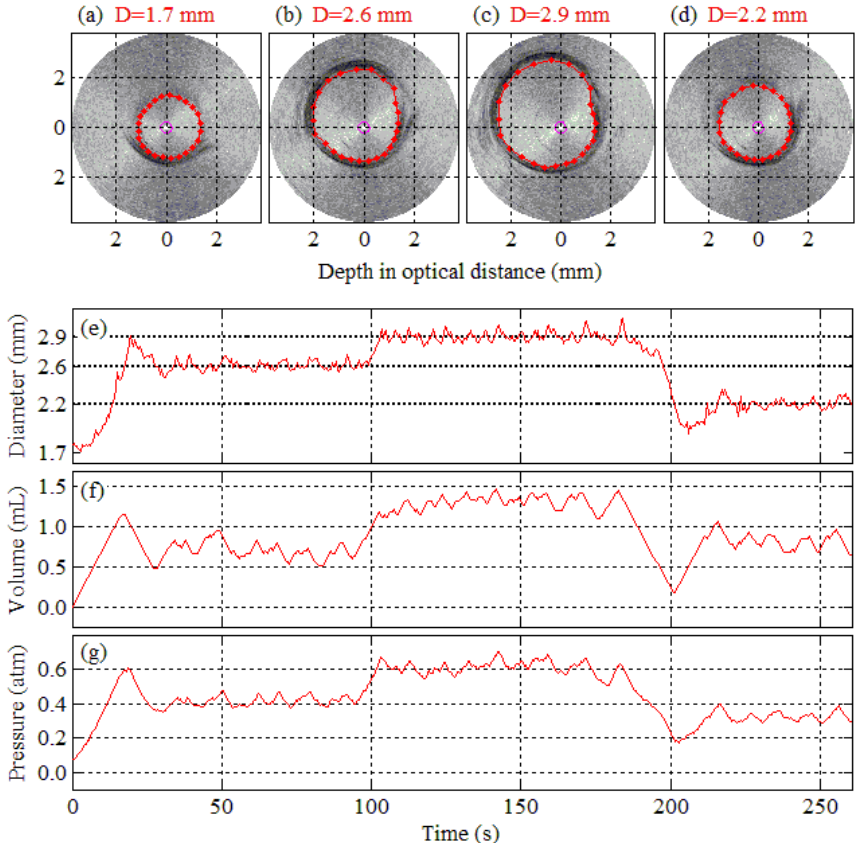

Figure 11.11. Acquired images at various diameters (a-d), and the diameter (e), the volume (f), and the pressure (g) during the control experiment using a sequence of target diameters

Applying the sequence of target diameters allowed us to more rigorously investigate the balloon inflation control in the blood displacement phase and artery deformation phase, using various target diameters all in one experiment. The implication of such an experiment is that one may be able to design a control system to achieve previously planned diameters at desired times, followed by maintaining the diameter at each target value for a desired duration of time. Such schemes could have implications in developing safer or more effective angioplasty procedures.

11.7 Concluding remarks

In this study, we extended the validity of a previously proposed control methodology to balloon inflation inside porcine arteries. The experiments were performed in an excised and a beating heart. In the excised heart experiment, the goal was to investigate if the control method was applicable to inflation of a compliant balloon inside porcine arteries. In the beating heart experiment, the first goal was to investigate if the edge detection algorithm was functional when blood was present in IVOCT images. The second goal was to investigate if the response time of the control system was sufficient to provide desired target diameters in presence of arterial contractions.

The control system provided a good convergence to target diameters in the excised heart experiment. This experiment indicated that the control method could be useful in characterizing the tissue's response to various balloon inflation procedures under controlled conditions. In this study, this experiment also provided us with a smooth transition to beating heart experiments. In the beating heart experiments, the balloon detection algorithm was successfully applied to estimate the balloon diameter in real-time. Although artery contractions constantly caused disturbances in the actual diameter

values, the control system provided average steady-state diameters close to the target diameters. We expect the disturbances to be smaller in angioplasty procedures, using higher pressures and using angioplasty balloons which are made of stiffer materials. Trials of such procedures could be addressed in future research. The future research may also focus on improving the performance characteristics of the control system, using more advanced control methods.

CHAPTER 12: CONCLUSION AND FUTURE WORK

In this thesis, we presented different opportunities provided by IVOCT monitoring of balloon deployment, in air, in artery phantoms, and in arteries.

We performed IVOCT monitoring and characterization of balloon inflation in a deployment tester. We achieved a detailed assessment of balloon diameter and wall thickness. The monitoring and characterization method could benefit balloon manufacturers. It provides a method to assess the quality of balloons and validate their performances.

We demonstrated monitoring and characterization of phantom deformation in two scenarios. In the first scenario, we provided results on monitoring and characterization of inner and outer diameters of single layer phantoms with different mechanical properties. The results of the first scenario implied that variation in mechanical properties of the phantoms could be sensed by IVOCT. This monitoring and characterization method could, therefore, provide information about the vessel wall composition and plaques. The results of the second scenario provided an assessment of deformation during balloon unfolding and inflation. Furthermore, a multi-layer phantom was used. The phantom was composed of three layers which simulated artery layers. As a result, not only did we achieve a characterization of the inner and outer diameters of the phantom, but also a characterization of layer thicknesses. Therefore, the proposed monitoring and characterization method could be used to study deformation of various vessel wall structures. It could also be used to study the effect of various balloon sizes, balloon folding strategies, and balloon deployment strategies on tissue deformation.

Monitoring and characterization results could also be applied in finite-element simulation of angioplasty. The results obtained from free expansion of the balloon could be used to generate a simulation model of the balloon. The results from confined scenarios could provide a benchmark to validate the simulation results. Simulation results of angioplasty, once validated, could provide insightful information for development of angioplasty devices and could improve the strategies applied in the angioplasty procedures.

We formulated balloon inflation as a control engineering problem. Various methods were proposed and simulated to control the balloon inflation based on measured pressure or diameter. Then, we successfully demonstrated experimental relevance of the proposed real-time inflation control to achieve a desired luminal diameter. In this method, in a feedback loop the diameter was estimated from IVOCT images in real-time. In various experiments the luminal diameter converged to different target diameters. The method was also robust to different flow rates. We first validated this method when the balloon was inflated inside a phantom. Then we extended the validation of this method to inflation inside a porcine artery of an excised heart. Finally, based on the experimental results obtained from a beating heart model we confirmed relevance of this method to controlled inflation in presence of blood flow and arterial contractions. To our knowledge, this was the first demonstration of a controlled clinical application, where IVOCT images were processed in real-time in a feedback loop. The combination of IVOCT and control engineering results in a technology that could benefit the medical device industry, researchers, and clinical users. Controlled balloon inflation could be used to perform experiments under predetermined and repeatable conditions to test angioplasty devices or study tissue response. Controlled balloon inflation could also be applied clinically to improve the angioplasty procedures.

Future research may provide further results in the areas of monitoring, characterization, simulation, and control:

Monitoring and characterization of stent deployment: A similar method could be used to monitor the deployment of a stent. Performance of various stents can be validated using IVOCT monitoring. The tissue response can be characterized, when stents with various designs and various sizes are used.

Extraction of mechanical properties: The IVOCT characterization results could be used in a mechanical analysis to estimate mechanical properties of balloons. One of the goals of the balloon forming process is to obtain material with increased stiffness, which is achieved by heating and stretching. The mechanical properties of the resulting balloon are not known. IVOCT characterization could provide a non-destructive method to extract such properties. It could also provide a method to extract mechanical properties of tissues.

Application of phantoms with inclusions: IVOCT characterization of deformation could be performed for a phantom with an inclusion with mechanical properties, different from those of the phantom. In this way, the response of atherosclerotic arteries could be studied. The results also provide a benchmark for validation of finite-element simulation of angioplasty in atherosclerotic arteries. In addition, techniques such as elastography [99] could be used to investigate the possibility of distinguishing the inclusion based on its different deformation trend during balloon deployment.

3D Simulation of angioplasty: IVOCT characterization results were used to validate 2D simulation results. Application of image analysis techniques to IVOCT images, acquired during a pullback of the probe, provides a 3D characterization, which could be used to validate 3D simulation results.

Control and simulation: We presented control of balloon inflation based on feedback from experimental data. The feedback in a control loop could also be provided from a simulation model. In a further advanced research, a model could be tuned in real-time based on various estimations, e.g., diameter and pressure.

Controlled inflation in *in vivo* experiments: In this thesis, we demonstrated the applicability of the proposed control method in a beating heart model. The next step could be the investigation of this method in an *in vivo* animal experiment.

REFERENCES

[1] H. Azarnoush, S. Vergnole, R. Bourezak, B. Boulet, and G. Lamouche, "Optical coherence tomography monitoring of angioplasty balloon inflation in a deployment tester," *Review of Scientific Instruments,* vol. 81, p. 083101, 2010.

[2] H. Azarnoush, R. Bourezak, S. Vergnole, G. Lamouche, and B. Boulet, "Optical coherence tomography characterization of balloon diameter and wall thickness," *Journal of Medical Devices,* vol. 4, p. 027523, 2010.

[3] H. Azarnoush, S. Vergnole, C. É. Bisaillon, V. Pazos, B. Boulet, and G. Lamouche, "Intravascular optical coherence tomography to characterize tissue deformation during angioplasty: preliminary experiments with artery phantoms," *Journal of Biomedical Optics,* Under review.

[4] H. Azarnoush, V. Pazos, S. Vergnole, B. Boulet, and G. Lamouche, "Finite-element simulation of angioplasty based on intravascular optical coherence tomography," To be submitted.

[5] H. Azarnoush, S. Vergnole, B. Boulet, R. DiRaddo, and G. Lamouche, "Real-time control of angioplasty balloon inflation based on feedback from intravascular optical coherence tomography: preliminary study on an artery phantom," *IEEE Transactions on Biomedical Engineering,* In press.

[6] H. Azarnoush, S. Vergnole, B. Boulet, M. Sowa, and G. Lamouche, "Real-time control of angioplasty balloon inflation based on feedback from intravascular optical coherence tomography: experimental validation using an excised heart and a beating heart model," *IEEE Transactions on Biomedical Engineering,* Accepted for publication.

[7] H. Azarnoush, S. Vergnole, B. Boulet, and G. Lamouche, "Optical coherence tomography layer thickness characterization of a mock artery during angioplasty balloon deployment," *SPIE Medical Imaging: Computer-Aided Diagnosis,* p. 79641V, 2011.

[8] H. Azarnoush, G. Lamouche, C. E. Bisaillon, C. Degrandpre, and B. Boulet, "Evaluation of a technique to estimate the compliance of atherosclerotic intima," in *Biomedical Simulation, Lecture Notes in Computer Science*, F. Bello, S. Cotin, Ed.: Springer-Verlag, Heidelberg, pp. 20-28, 2010.

[9] G. Lamouche, H. Azarnoush, S. Vergnole, V. Pazos, C. E. Bisaillon, P. Debergue, B. Boulet, and R. Diraddo, "Assessing mechanical properties with intravascular or endoscopic optical coherence tomography," *Proceedings of SPIE Photonics West: Bios Optical Interactions with Tissue and Cells XXII,* vol. 7897, p. 789708, 2011.

[10] H. Azarnoush, S. Vergnole, M. Hewko, B. Boulet, M. Sowa, and G. Lamouche, "Detection of inflating balloon in optical coherence tomography images of a porcine artery in a beating heart experiment," *SPIE Medical Imaging: Visualization, Image-Guided Procedures, and Modeling,* vol. 7964, p. 79641V, 2011.

[11] H. Azarnoush and B. Boulet, "Angioplasty balloon deployment control," *American Control Conference,* pp. 3572-3573, 2010.

[12] H. Azarnoush, S. Vergnole, B. Boulet, and G. Lamouche, "Real-time control of angioplasty balloon inflation based on feedback from intravascular optical coherence tomography," *SPIE Photonics West: Diagnostic and Therapeutic Applications of Light in Cardiology,* 2012.

[13] R. M. Califf, D. F. Fortin, D. J. Frid, W. R. Harlan III, E. M. Ohman, J. R. Bengtson, C. L. Nelson, J. E. Tcheng, D. B. Mark, and R. S. Stack, "Restenosis after coronary angioplasty: an overview," *Journal of the American College of Cardiology,* vol. 17, pp. 2-13, 1991.

[14] K. J. Beatt, P. W. Serruys, H. E. Luijten, B. J. Rensing, H. Suryapranata, P. de Feyter, M. van den Brand, G. Jan Laarman, J. Roelandt, and G. Anne van ES, "Restenosis after coronary angioplasty: the paradox of increased lumen diameter and restenosis," *Journal of the American College of Cardiology,* vol. 19, pp. 258-266, 1992.

[15] J. H. Rogers and J. M. Lasala, "Coronary artery dissection and perforation complicating percutaneous coronary intervention," *Journal of Invasive Cardiology,* vol. 16, pp. 493-499, 2004.

[16] D. Faxon, *Restenosis: a guide to therapy*: Martin Dunitz, 2001.

[17] D. L. Fischman, M. B. Leon, D. S. Baim, R. A. Schatz, M. P. Savage, I. Penn, K. Detre, L. Veltri, D. Ricci, and M. Nobuyoshi, "A randomized comparison of coronary-stent placement and balloon angioplasty in the treatment of coronary artery disease," *New England Journal of Medicine,* vol. 331, pp. 496-501, 1994.

[18] P. W. Serruys, P. de Jaegere, F. Kiemeneij, C. Macaya, W. Rutsch, G. Heyndrickx, H. Emanuelsson, J. Marco, V. Legrand, and P. Materne, "A comparison of balloon-expandable-stent implantation with balloon angioplasty in patients with coronary artery disease," *New England Journal of Medicine,* vol. 331, pp. 489-495, 1994.

[19] J. Cosgrave, G. Melzi, G. G. L. Biondi-Zoccai, F. Airoldi, A. Chieffo, G. M. Sangiorgi, M. Montorfano, I. Michev, M. Carlino, and E. Bonizzoni, "Drug-

eluting stent restenosis: the pattern predicts the outcome," *Journal of the American College of Cardiology,* vol. 47, p. 2399, 2006.

[20] A. Kivelä and J. Hartikainen, "Restenosis related to percutaneous coronary intervention has been solved?," *Annals of medicine,* vol. 38, pp. 173-187, 2006.

[21] G. D. Dangas, B. E. Claessen, A. Caixeta, E. A. Sanidas, G. S. Mintz, and R. Mehran, "In-Stent Restenosis in the Drug-Eluting Stent Era," *Journal of the American College of Cardiology,* vol. 56, pp. 1897-1907, 2010.

[22] C. Briguori, J. Tobis, T. Nishida, M. Vaghetti, R. Albiero, C. Di Mario, and A. Colombo, "Discrepancy between angiography and intravascular ultrasound when analysing small coronary arteries," *European Heart Journal,* vol. 23, p. 247, 2002.

[23] M. E. Brezinski, *Optical coherence tomography: principles and applications*: Academic Press, 2006.

[24] A. C. Bovik, *Handbook of image and video processing*: Academic Press, 2005.

[25] L. O'Gorman, M. J. Sammon, and M. Seul, *Practical algorithms for image analysis: description, examples, programs, and projects*: Cambridge University Press, 2008.

[26] R. D. Cook, *Concepts and applications of finite element analysis*: A1bazaar, 2007.

[27] R. C. Dorf, R. H. Bishop, "Modern control systems," 11 ed: Prentice Hall, 2008.

[28] W. H. Organization, *World health statistics 2006*: World Health Organization, 2006.

[29] D. Lloyd-Jones, R. J. Adams, T. M. Brown, M. Carnethon, S. Dai, G. De Simone, T. B. Ferguson, E. Ford, K. Furie, and C. Gillespie, "Heart disease and stroke statistics--2010 update: a report from the American Heart Association," *Circulation,* vol. 121, p. e46, 2010.

[30] E. Regar, P. W. Serruys, and T. G. Van Leeuwen, *Optical coherence tomography in cardiovascular research*: Informa healthcare, 2007.

[31] R. Blasini, F. J. Neumann, C. Schmitt, J. Bökenkamp, and A. Schömig, "Comparison of angiography and intravascular ultrasound for the assessment of lumen size after coronary stent placement: impact of dilation pressures," *Catheterization and Cardiovascular Diagnosis,* vol. 42, p. 113, 1997.

[32] P. J. Fitzgerald, A. Oshima, M. Hayase, J. A. Metz, S. R. Bailey, D. S. Baim, M. W. Cleman, E. Deutsch, D. J. Diver, and M. B. Leon, "Final results of the can routine ultrasound influence stent expansion (CRUISE) study," *Circulation,* vol. 102, pp. 523-530, 2000.

[33] R. Russo, M. Attubato, C. Davidson, A. DeFranco, P. Fitzgerald, R. Iaffaldano, F. Ling, P. Silva, K. Rocha-Singh, and G. Smith, "Angiography versus intravascular ultrasound-directed stent placement: final results from AVID," *Circulation,* vol. 100, p. I234, 1999.

[34] A. Colombo, P. Hall, S. Nakamura, Y. Almagor, L. Maiello, G. Martini, A. Gaglione, S. L. Goldberg, and J. M. Tobis, "Intracoronary stenting without anticoagulation accomplished with intravascular ultrasound guidance," *Circulation,* vol. 91, p. 1676, 1995.

[35] T. Kume, T. Akasaka, T. Kawamoto, N. Watanabe, E. Toyota, Y. Neishi, R. Sukmawan, Y. Sadahira, and K. Yoshida, "Assessment of coronary intima-media thickness by optical coherence tomography," *Circulation,* vol. 69, pp. 903-907, 2005.

[36] B. Bouma, G. Tearney, H. Yabushita, M. Shishkov, C. Kauffman, D. DeJoseph Gauthier, B. MacNeill, S. Houser, H. Aretz, and E. Halpern, "Evaluation of

intracoronary stenting by intravascular optical coherence tomography," *Heart,* vol. 89, p. 317, 2003.

[37] I. K. Jang, G. J. Tearney, B. MacNeill, M. Takano, F. Moselewski, N. Iftima, M. Shishkov, S. Houser, H. T. Aretz, and E. F. Halpern, "*In vivo* characterization of coronary atherosclerotic plaque by use of optical coherence tomography," *Circulation,* vol. 111, p. 1551, 2005.

[38] D. A. Clark, *Coronary Angioplasty*, Second ed.: Wiley-Liss, 1991.

[39] S. Baumüller, S. Leschka, L. Desbiolles, P. Stolzmann, H. Scheffel, B. Seifert, B. Marincek, and H. Alkadhi, "Dual-source versus 64-section ct coronary angiography at lower heart rates: comparison of accuracy and radiation Dose1," *Radiology,* vol. 253, p. 56, 2009.

[40] E. Falk, P. K. Shah, and V. Fuster, "Coronary plaque disruption," *Circulation,* vol. 92, p. 657, 1995.

[41] M. Davies, "Anatomic features in victims of sudden coronary death. Coronary artery pathology," *Circulation,* vol. 85, p. I19, 1992.

[42] E. Spuentrup, A. Ruebben, T. Schaeffter, W. J. Manning, R. W. Gunther, and A. Buecker, "Magnetic resonance-guided coronary artery stent placement in a swine model," *Circulation,* vol. 105, p. 874, 2002.

[43] G. A. Holzapfel, G. Sommer, C. T. Gasser, and P. Regitnig, "Determination of layer-specific mechanical properties of human coronary arteries with nonatherosclerotic intimal thickening and related constitutive modeling," *American Journal of Physiology-Heart and Circulatory Physiology,* vol. 289, p. H2048, 2005.

[44] G. A. Holzapfel, M. Stadler, and C. A. J. Schulze-Bauer, "A layer-specific three-dimensional model for the simulation of balloon angioplasty using magnetic resonance imaging and mechanical testing," *Annals of Biomedical Engineering,* vol. 30, pp. 753-767, 2002.

[45] S. Oh, M. Klelnberger, and J. McElhaney, "Finite-element analysis of balloon angioplasty," *Medical and Biological Engineering and Computing,* vol. 32, pp. 108-114, 1994.

[46] T. C. Gasser and G. A. Holzapfel, "Finite element modeling of balloon angioplasty by considering overstretch of remnant non-diseased tissues in lesions," *Computational Mechanics,* vol. 40, pp. 47-60, 2007.

[47] C. Dumoulin and B. Cochelin, "Mechanical behaviour modelling of balloon-expandable stents," *Journal of Biomechanics,* vol. 33, pp. 1461-1470, 2000.

[48] F. Gervaso, C. Capelli, L. Petrini, S. Lattanzio, L. Di Virgilio, and F. Migliavacca, "On the effects of different strategies in modelling balloon-expandable stenting by means of finite element method," *Journal of Biomechanics,* vol. 41, pp. 1206-1212, 2008.

[49] F. Migliavacca, L. Petrini, V. Montanari, I. Quagliana, F. Auricchio, and G. Dubini, "A predictive study of the mechanical behaviour of coronary stents by computer modelling," *Medical Engineering & Physics,* vol. 27, pp. 13-18, 2005.

[50] W. Q. Wang, D. K. Liang, D. Z. Yang, and M. Qi, "Analysis of the transient expansion behavior and design optimization of coronary stents by finite element method," *Journal of Biomechanics,* vol. 39, pp. 21-32, 2006.

[51] D. E. Kiousis, A. R. Wulff, and G. A. Holzapfel, "Experimental studies and numerical analysis of the inflation and interaction of vascular balloon catheter-stent systems," *Annals of Biomedical Engineering,* vol. 37, pp. 315-330, 2009.

[52] H. Zahedmanesh, D. John Kelly, and C. Lally, "Simulation of a balloon expandable stent in a realistic coronary artery--Determination of the optimum modelling strategy," *Journal of Biomechanics,* vol. 43, pp. 2126-2132, 2010.

[53] M. Unverdorben, M. Groll, P. Glaeser, P. Osypka, T. Osypka, B. Kunkel, and C. Vallbracht, "Preliminary results achieved by a computer-assisted system for controlled balloon dilatation of coronary and peripheral arteries," *Computers and Biomedical Research,* vol. 30, pp. 403-413, 1997.

[54] M. Unverdorben, P. Glaeser, R. Degenhardt, G. Rippin, H. K. Berthold, and C. Vallbracht, "Controlled balloon inflation reduces long-term restenosis after percutaneous transluminal coronary angioplasty," *The Journal of Invasive Cardiology,* vol. 13, p. 774, 2001.

[55] D. Leibowitz, M. Abu-Gazala, I. Katz, H. Danenberg, H. Nassar, L. Boguslavsky, M. Mosseri, B. Varshitzsky, C. Lotan, and A. Weiss, "Computerized gradual balloon inflation: a novel strategy of coronary angioplasty superior to a standard manual approach," *Cardiovascular Revascularization Medicine,* vol. 10, pp. 45-48, 2009.

[56] A. Murray and V. Allen, "Angioplasty pressure-volume measurement," *Medical and Biological Engineering and Computing,* vol. 33, pp. 747-748, 1995.

[57] A. Murray and V. Allen, "Measurement of angioplasty lumen volume and wall compliance: a laboratory study," *Physiological Measurement,* vol. 18, p. 39, 1997.

[58] A. Murray, V. Allen, and M. Bennett, "Validation of an automated technique for determining the mechanical characteristics of coronary arteries during balloon angioplasty: laboratory assessment with necropsy segments," *Heart,* vol. 79, p. 608, 1998.

[59] T. Olbrich and A. Murray, "Assessment of computer-controlled inflation/deflation for determining the properties of PTCA balloon catheters with pressure-volume curves," *Physiological Measurement,* vol. 22, p. 299, 2001.

[60] T. Olbrich and A. Murray, "Assessment of a technique to determine the mechanical properties of coronary arteries using mock arteries," *Physiological Measurement,* vol. 25, p. 997, 2004.

[61] T. Olbrich, D. Williams, J. Doig, and A. Murray, "*In vivo* assessment of coronary artery angioplasty and stent deployment from balloon pressure–volume data," *Physiological Measurement,* vol. 27, p. 213, 2006.

[62] M. Shehab, L. Michalis, and M. Rees, "Balloon angioplasty optimization: Should we measure balloon volume as well as pressure?," *CardioVascular and Interventional Radiology,* vol. 31, pp. 149-157, 2008.

[63] D. Huang, E. A. Swanson, C. P. Lin, J. S. Schuman, W. G. Stinson, W. Chang, M. R. Hee, T. Flotte, K. Gregory, and C. A. Puliafito, "Optical coherence tomography," *Science,* vol. 254, p. 1178, 1991.

[64] A. F. Fercher, C. K. Hitzenberger, G. Kamp, and S. Y. El-Zaiat, "Measurement of intraocular distances by backscattering spectral interferometry," *Optics Communications,* vol. 117, pp. 43-48, 1995.

[65] G. Häusler and M. W. Lindner, "“Coherence radar” and “spectral radar”—new tools for dermatological diagnosis," *Journal of Biomedical Optics,* vol. 3, p. 21, 1998.

[66] S. Chinn, E. Swanson, and J. Fujimoto, "Optical coherence tomography using a frequency-tunable optical source," *Optics letters,* vol. 22, pp. 340-342, 1997.

[67] B. Golubovic, B. E. Bouma, G. J. Tearney, and J. G. Fujimoto, "Optical frequency-domain reflectometry using rapid wavelength tuning of a Cr4+:forsterite laser," *Optics Letters,* vol. 22, pp. 1704-1706, 1997.

[68] F. Lexer, C. Hitzenberger, A. Fercher, and M. Kulhavy, "Wavelength-tuning interferometry of intraocular distances," *Applied optics,* vol. 36, pp. 6548-6553, 1997.

[69] S. Yun, G. Tearney, J. de Boer, N. Iftimia, and B. Bouma, "High-speed optical frequency-domain imaging," *Optics Express,* vol. 11, pp. 2953-2963, 2003.

[70] C. M. Eigenwillig, B. R. Biedermann, G. Palte, and R. Huber, "K-space linear Fourier domain mode locked laser and applications for optical coherence tomography," *Optics Express,* vol. 16, pp. 8916-8937, 2008.

[71] M. A. Choma, K. Hsu, and J. A. Izatt, "Swept source optical coherence tomography using an all-fiber 1300 nm ring laser source," *Journal of Biomedical Optics,* vol. 10, p. 044009, 2005.

[72] S. Vergnole, D. Lévesque, and G. Lamouche, "Experimental validation of an optimized signal processing method to handle non-linearity in swept-source optical coherence tomography," *Optics Express,* vol. 18, pp. 10446-10461, 2010.

[73] G. Lamouche, M. Dufour, M. Hewko, S. Vergnole, B. Gauthier, C. É. Bisaillon, J. P. Monchalin, and M. G. Sowa, "Intravascular optical coherence tomography on a beating heart model," *Journal of Biomedical Optics,* vol. 15, p. 046023, 2011.

[74] D. Eberly, *Ridges in image and data analysis*: Kluwer Academic Pub, 1996.

[75] I. Laptev, H. Mayer, T. Lindeberg, W. Eckstein, C. Steger, and A. Baumgartner, "Automatic extraction of roads from aerial images based on scale space and snakes," *Machine Vision and Applications,* vol. 12, pp. 23-31, 2000.

[76] C. Kirbas and F. Quek, "A review of vessel extraction techniques and algorithms," *ACM Computing Surveys,* vol. 36, pp. 81-121, 2004.

[77] Y. Lee and W. Rhodes, "Nonlinear image processing by a rotating kernel transformation," *Optics letters,* vol. 15, pp. 1383-1385, 1990.

[78] J. Canny, "A computational approach to edge detection," *IEEE Transactions on Pattern Analysis and Machine Intelligence,* pp. 679-698, 1986.

[79] D. Marr and E. Hildreth, "Theory of edge detection," *Proceedings of the Royal Society of London. Series B. Biological Sciences,* vol. 207, p. 187, 1980.

[80] A. Goshtasby, *2-D and 3-D image registration for medical, remote sensing, and industrial applications*: Wiley-Interscience, 2005.

[81] J. D. Humphrey, *Cardiovascular solid mechanics: cells, tissues, and organs*: Springer Verlag, 2002.

[82] R. Ogden, "Large deformation isotropic elasticity-on the correlation of theory and experiment for incompressible rubberlike solids," *Proceedings of the Royal Society of London. A. Mathematical and Physical Sciences,* vol. 326, p. 565, 1972.

[83] D. Laroche, S. Delorme, T. Anderson, and R. DiRaddo, "Computer prediction of friction in balloon angioplasty and stent implantation," *Biomedical Simulation,* pp. 1-8, 2006.

[84] B. Delaunay, "Sur la sphere vide," *Izv. Akad. Nauk SSSR, Otdelenie Matematicheskii i Estestvennyka Nauk,* vol. 7, pp. 793-800, 1934.

[85] R. E. Klabunde, *Cardiovascular physiology concepts*: Lippincott Williams & Wilkins, 2005.

[86] R. Ilia, H. Cabin, S. McConnell, M. Cleman, and M. Remetz, "Coronary angioplasty with gradual versus rapid balloon inflation: initial results and complications," *Catheterization and Cardiovascular Diagnosis,* vol. 29, pp. 199-202, 1993.

[87] D. Lalli, "Cycle-to-cycle control of the angioplasty balloon fabrication process," Master's thesis, Electrical and Computer Engineering, McGill University, 2006.

[88] C. E. Bisaillon, M. Dufour, and G. Lamouche, " Artery phantoms for intravascular optical coherence tomography: healthy arteries," *Biomedical Optics Express,* vol. 2, pp. 2599-1-2613, 2011.

[89] A. J. Narracott, P. V. Lawford, J. P. G. Gunn, and D. R. Hose, "Balloon folding affects the symmetry of stent deployment: experimental and computational evidence," *Proceedings of Engineering in Medicine and Biology*, pp. 3069-3073, 2007.

[90] K. Takashima, T. Kitou, K. Mori, and K. Ikeuchi, "Simulation and experimental observation of contact conditions between stents and artery models," *Medical Engineering & Physics,* vol. 29, pp. 326-335, 2007.

[91] K. Levenberg, "A method for the solution of certain nonlinear problems in least squares," *Quarterly of Applied Mathematics,* vol. 2, pp. 164–168, 1944.

[92] V. Pazos, R. Mongrain, and J. C. Tardif, "Mechanical characterization of atherosclerotic arteries using finite-element modeling: feasibility study on mock arteries," *IEEE Transactions on Biomedical Engineering,* vol. 57, pp. 1520-1528, 2010.

[93] A. Pandit, X. Lu, C. Wang, and G. S. Kassab, "Biaxial elastic material properties of porcine coronary media and adventitia," *American Journal of Physiology-Heart and Circulatory Physiology,* vol. 288, p. H2581, 2005.

[94] R. Ogden, G. Saccomandi, and I. Sgura, "Fitting hyperelastic models to experimental data," *Computational Mechanics,* vol. 34, pp. 484-502, 2004.

[95] J. Isner, K. Rosenfield, D. Losordo, L. Rose, R. Langevin Jr, S. Razvi, and B. Kosowsky, "Combination balloon-ultrasound imaging catheter for percutaneous transluminal angioplasty. Validation of imaging, analysis of recoil, and identification of plaque fracture," *Circulation,* vol. 84, p. 739, 1991.

[96] H. Mudra, V. Klauss, R. Blasini, M. Kroetz, J. Rieber, E. Regar, and K. Theisen, "Ultrasound guidance of Palmaz-Schatz intracoronary stenting with a combined intravascular ultrasound balloon catheter," *Circulation,* vol. 90, p. 1252, 1994.

[97] M. Kawata, T. Okada, N. Igarashi, K. Okajima, Y. Domoto, and T. Mizutani, "Assessment of intravascular ultrasound-bearing balloon catheter-guided percutaneous transluminal coronary angioplasty and stenting," *Heart and vessels,* p. 185, 1997.

[98] E. M. Ohman, J. Marquis, D. R. Ricci, R. Brown, M. L. Knudtson, D. J. Kereiakes, J. K. Samaha, J. R. Margolis, A. L. Niederman, and L. S. Dean, "A

randomized comparison of the effects of gradual prolonged versus standard primary balloon inflation on early and late outcome. Results of a multicenter clinical trial. Perfusion Balloon Catheter Study Group," *Circulation,* vol. 89, p. 1118, 1994.

[99] R. Chan, A. Chau, W. Karl, S. Nadkarni, A. Khalil, N. Iftimia, M. Shishkov, G. Tearney, M. Kaazempur-Mofrad, and B. Bouma, "OCT-based arterial elastography: robust estimation exploiting tissue biomechanics," *Optics Express,* vol. 12, pp. 4558–4572, 2004.